UCLouvain

École polytechnique de Louvain

Actuator lines modeling and investigation of tilted wind turbines for improved farm efficiency

Author: **François Trigaux**
Supervisor: **Grégoire Winckelmans**
Readers: **Philippe Chatelain, Hervé Jeanmart, Maud Moens**
Academic year 2018–2019
Master [120] in Mechanical Engineering

Remerciements

Premièrement, les ressources de calculs ayant permis la réalisation de ce travail ont été fournies par le Consortium des Équipements de Calcul Intensif en Fédération Wallonie-Bruxelles (CÉCI) financé par le Fonds de la Recherche Scientifique de Belgique (F.R.S.-FNRS) sous la convention 2.5020.11, ainsi que par le super-ordinateur Tier-1 de la Fédération Wallonie-Bruxelles.

Je tiens en premier lieu à remercier mon promoteur, le professeur Grégoire Winckelmans, pour l'aide qu'il m'a apportée tout au long de ce travail. Son enthousiasme fut communicatif et m'a redonné confiance lors des moments de doute. La grande rigueur de ses relectures a été d'une importance capitale dans l'amélioration de ce texte.

Merci ensuite au docteur Maud Moens qui a supervisé chaque étape de cette thèse. La qualité de son travail passé fut un fondement rêvé pour amorcer ce sujet. Sa disponibilité sans faille a été d'un grand secours lorsqu'une question survenait, et une solution a toujours su être trouvée à mes problèmes, parfois avant même qu'ils ne se posent. Son avis, ses conseils et relectures ont été des éléments capitaux tout au long de ce travail.

Cette période n'aurait probablement pas été la même sans le soutien de mes co-mémorants du local B037. En particulier, je tiens à remercier Juan, Pierre et Oscar, qui ont contribué à entrecouper les dernières semaines de rédaction de nombreuses pauses café, déjeuner ou tractions. Je pense également à Timothée qui a su m'aider à garder l'équilibre au kot, entre ambiance studieuse et convivialité.

Je souhaite également adresser mes remerciements à tous mes amis, qui ont toujours su me changer les idées aux bons moments. Leur soutien inconditionnel et leur bonne humeur ont rendu ces derniers mois d'étude bien plus agréables.

Enfin, je remercie ma famille qui a toujours été là pour m'aider et qui a supporté tant bien que mal mes explications compliquées. Leurs attentions et leur compréhension ont été particulièrement importantes pour surmonter les différentes épreuves. Merci également à mes cousins qui, depuis l'autre côté de l'Atlantique, ont accepté d'améliorer l'orthographe anglaise de ce texte.

Contents

1 Introduction **1**
- 1.1 Wind energy and wind farm control . . . 1
- 1.2 Tilting as a wake steering strategy . . . 2
- 1.3 Objectives and outlines . . . 3

2 Numerical simulation of flow and wind turbines **5**
- 2.1 BigFlow . . . 5
- 2.2 Actuator models . . . 7
  - 2.2.1 Actuator Disk with tip-loss correction . . . 8
  - 2.2.2 Actuator Lines . . . 9

3 Actuator lines model **11**
- 3.1 Improved actuator lines model . . . 11
  - 3.1.1 Velocity interpolation . . . 11
  - 3.1.2 Forces distribution . . . 13
  - 3.1.3 Numerical constrains . . . 15
- 3.2 Characterization in uniform flows . . . 16
  - 3.2.1 Influence of the kernel topology . . . 16
  - 3.2.2 Influence of the resolution . . . 21
  - 3.2.3 Influence of the kernel width . . . 23
- 3.3 Validation at various upstream velocities . . . 26
- 3.4 Actuator lines in an atmospheric boundary layer . . . 29
  - 3.4.1 Numerical setup . . . 29
  - 3.4.2 Results and discussion . . . 30
- 3.5 Conclusion . . . 36

4 Tilted wind turbine in an ABL **39**
- 4.1 Numerical set up . . . 39
- 4.2 Power and thrust . . . 40
- 4.3 Loads and fatigue analysis . . . 41
- 4.4 Wake behaviour . . . 44
  - 4.4.1 Instantaneous streamwise velocity . . . 44
  - 4.4.2 Flow statistics . . . 45
- 4.5 Conclusion . . . 49

5 Tilted turbines in a wind farm **51**
5.1 Numerical set-up . . . 51
5.2 Power and thrust . . . 52
5.3 Loads . . . 53
5.3.1 Time-averaged loads . . . 54
5.3.2 Tilting moment . . . 54
5.3.3 Bending moments . . . 55
5.4 Wake statistics . . . 57
5.4.1 Time-averaged streamwise velocity . . . 57
5.4.2 Time-averaged transverse velocities and vorticity . . . 61
5.5 Conclusion . . . 62

6 Conclusion and perspectives **63**

A Statistics of the atmospheric boundary layers **65**

B Computation of the equivalent bending moment **67**

C Instantaneous velocity in the wind farms **69**

Chapter 1

Introduction

1.1 Wind energy and wind farm control

Currently, the production of electricity relies mostly on fossil fuels, such as gas, oil and coal. However, those fossil fuels have non negligible drawbacks such as the emission of greenhouse gasses, air pollution, limited availability and uneven distribution on the globe. Therefore, renewable energy have gained popularity and their development has risen importantly in the last years. Following hydropower, wind is the second most common source of energy and generated 959 TWh in 2016 for the entire planet [1].

Wind power presents some major advantages. It does not emit neither greenhouse gases nor air pollutants that could create acid rains or cause respiratory diseases. Its extraction has one of the lowest CO2 emissions over its entire lifetime [2]. Wind is also widely available and can support countries in getting energetically self-sufficient. Finally, recent development achieved to reduce costs in such a way that land based wind turbines are now competitive with fossil energy sources [3]. Those advantages have led to a massive development of the wind energy in the recent years, as illustrated on figure 1.1 where the installed capacity of wind power is depicted for Belgium [4]. In fifteen years, the share of wind based electricity production rose from 0.02% to 8.02% in 2015.

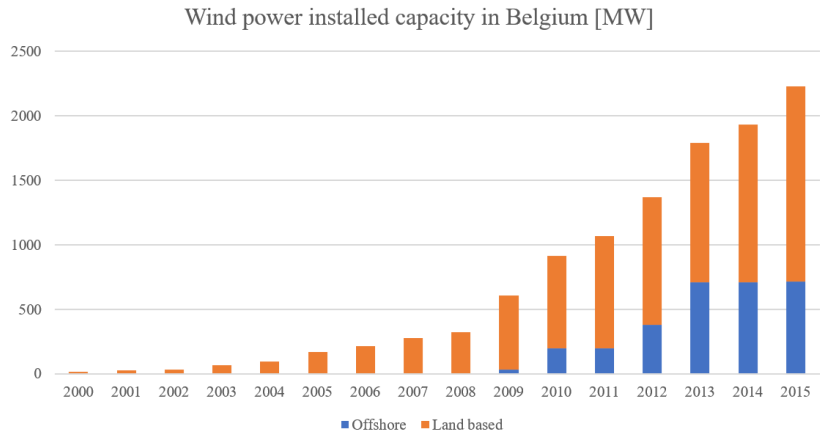

Figure 1.1: *Evolution of the installed capacity of wind power in Belgium.*

The economic viability of a wind project is often constrained by the the local climatic conditions of the site. The wind turbines need to be placed on a location presenting excellent wind conditions to ensure a reasonable return on investment. However, those zones are often located far from the energy consuming region and in remote area, leading to increased costs due to civil and land works, or the extension of the transportation capacity. To overcome this financial limitation, wind turbines are now generally gathered in a wind farm whether offshore or onshore in order to benefit from the economy of scale. A wind farm presents a new challenge as it consists in an entire system that must be optimized regarding the power extraction or the turbines loads. Apart from the optimal design of one single wind turbine, the interactions between the different machines and their wakes can cause issues such as the diminution of the power capture or the increase of the unsteady loads on the wind turbine. Studies showed a reduction of almost 40% of the power output when the wind turbines are aligned in the direction of the wind [5].

To mitigate those effects, turbines are controlled to improve the overall power. Those control techniques act on the axial induction or on the wake direction. By adapting the rotation speed using the the generator torque or the pitch angle of the blades, the wake intensity can be alleviated and the power available downstream can be increased. The wake deviation can be achieved with individual pitch control of the blades, or an intentional misalignment of the rotor with the free-flow. The latter is usually obtained by adapting the yaw angle of the turbines. As a result, the rotor thrust is deviated from the flow direction and a tangential force component applies a skew on the streamtube. In spite of the power reduction of the first wind turbine, this approach gave successful results in increasing the global power output as well as reducing the loads on the downstream machines [6]. In this work, a new strategy for the wake deviation is studied. Instead of acting on the yaw angle, we propose to modify the tilt angle to obtain a vertical wake deflection.

1.2 Tilting as a wake steering strategy

Tilting a rotor consists in inclining the wind turbine as depicted on figure 1.2. Similarly to yawing, it yields to a wake deflection that can be beneficial for the downstream located machines. Moreover, tilting a wind turbine presents several advantages over yawing. First, the wake is deviated downwards or upwards which decreases the impact of wake meandering and the sensitivity to the wind direction. Also, deflecting the wake downwards is likely to pull in the high velocities of the upper wind, yielding to an increased power extraction. Similarly, the downwards deviation of the wake could reduce the deep-array effect. This reorientation of the wake is also likely to increase the interaction with the ground, leading to a faster decay of the velocity deficit and the turbulent kinetic energy.

Applying tilt to a single turbine will decrease its power extraction due to the misalignment with the incoming wind. Furthermore, the flow impacting the blades will be modified. As observed on figure 1.2, the downwind part of the rotor is deeper in the wake than the upwind part, and thus captures a slower wind speed. The variation of the forces on the blades through one rotation is thus amplified or diluted according to the tilt angle. This asymmetry influences the loads of the machine and impacts the probability of failure caused by fatigue. To be a valid approach, tilting will need to prove its ability to overcome those two problems. First,

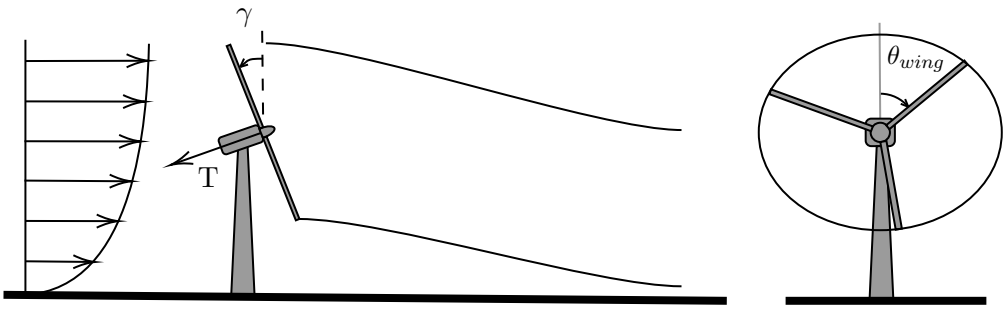

Figure 1.2: *Tilted wind turbine with a downwind configuration, the resulting thrust as well as the corresponding deflection of the streamtube.*

the power loss of the tilted turbines will have to be outweighed by the increased power output of the downstream turbines. Second, the increase of the structural loads must stay limited.

To date, few studies have been conducted on the effect of tilting. Abdelsalam & Ramalingam [7] used RANS to obtain a significant wake recovery and a gain of power in the downstream flow for lightly tilted turbines. Fleming *et al* [8] used LES to show that tilting achieved to deflect the wake, and observed a reduction of some loads, but the increase of the bending moment on the blades. Finally, Annoni *et al* [9] studied the interaction of two and three tilted turbines and obtained an increased total power output for the aligned case. However, none of those studies performed a complete assessment of the power in a larger wind farm, or verified the evolution of the unsteady loads on the turbines in such a configuration. This work has the objective of filling this knowledge gap and to elaborate on the effects of tilting.

1.3 Objectives and outlines

This thesis aims at studying in some depth the effect of a variation of the tilt angle setting on the efficiency and the loads in a wind farm. Various configurations will be characterized regarding their power output and the variation of the various moments acting on the machines. This study is performed using high fidelity computational fluid dynamic tools. The turbulent wind and the fluid dynamics will be simulated using LES and the wind turbines will be modeled using state-of-the-art actuator models.

The in-house developed fourth-order finite difference flow solver was previously enriched by an advanced actuator disk model by Moens [10]. Actuator disks are particularly suitable for large farm simulation as they are able to reproduce far-wake structures accurately even on coarse grid. They are also less limited by the numerical stability as the position of the actuator points stays stationary. However, the near-wake behaviour is not captured accurately by a disk approach. Moreover, even the advanced actuator disk model uses an arguable assumption when used in tilted mode. To overcome those limitations, an actuator lines model was developed. This model accounts for the finite number of blades, and a specific effort was put in the accurate representation of the tip behaviour.

The actuator lines model will be assessed by comparing with the advanced actuator disk model on both fine and coarse grids. This assessment will first be performed in uniform flow and then in a turbulent boundary layer to emphasize the differences between the two models.

Then, the actuator lines model will be used to simulate a small wind farm containing tilted turbines. Various configurations will be studied in order to emphasize the effect of tilt angle on the wake behaviour and the power output.

Chapter 2 This chapter briefly presents the numerical tools used in this work. The fourth-order finite difference flow solver is first described. Then, the actuator models used in the thesis are reviewed, and their theory is quickly recalled. A review of the state of the art of actuator line modeling is also performed to provide a theoretical basis to our implementation.

Chapter 3 A detailed description of the improved actuator lines model is given, with a special focus on the mollification of the forces generated by the turbine on the surrounding flow. In fact, it was emphasized by various authors that the forces distribution had a tremendous influence on the obtained results. Multiple mollification strategies are thus assessed in a uniform flow with a typical upstream velocity and their characteristics are discussed. Then, a choice is made on the method that gives the best results regarding the forces, power and wake behaviour. This model is then verified with the advanced actuator disk for various upstream velocities. Further investigations are performed in an atmospheric boundary layer to characterize the behaviour of the method in realistic turbulent flows.

Chapter 4 The actuator lines model is then used for the simulation of tilted wind turbines in an atmospheric boundary layer. Various tilted configurations are assessed and the influence of the tilt angle is discussed over one single wind turbine. The wake deflection is observed to derive the potential improvement of this technique regarding the optimization of the total wind farm. The influence on the total power and the modification of the structural loads are also discussed.

Chapter 5 This chapter focuses on the simulation of a small wind farm containing tilted wind turbines, and the interaction between the different machines is quantified. The efficiency of the entire wind farm is considered, as well as the structural loads and the long-term behaviour of the wake.

Chapter 2

Numerical simulation of flow and wind turbines

2.1 BigFlow

The flow is computed using LES with a in-house developped 4th order finite difference code called BigFlow. This code solves the incompressible Navier-Stokes equations supplemented by a subsgrid scale model

$$\nabla \cdot \mathbf{v} = 0,$$
$$\frac{\partial \mathbf{v}}{\partial t} + (\mathbf{v} \cdot \nabla)\mathbf{v} = -\nabla P + \nabla \cdot (\tau + \tau^{sgs}) + \mathbf{f}.$$

where $P = p/\rho$, τ stands for the shear stress, τ^{sgs} is the extra-stress tensor modeling the effect of the subgrid scales of the turbulence on the resolved scales and f is a volumic force. The code is formulated in primitive variables (pressure-velocity) and uses a structured grid with staggered configuration. The viscous stress τ is $\tau_{ij} = 2\nu S_{ij}$, with S_{ij} the strain rate of deformation defined as

$$S_{ij} = \frac{1}{2}\left(\frac{\partial u_i}{\partial x_j} + \frac{\partial u_j}{\partial x_i}\right).$$

The sub-grid scales effects are computed using a classical Smagorinsky model or a Regularized Variational Mustiscale model, as implemented by Duponcheel [11]. The Smagorinsky [12] eddy viscosity model for subgrid scales reads

$$\tau_{ij}^{sgs} = 2\nu^{sgs} S_{ij} \text{ with } \nu^{sgs} = C\Delta^2 (2S_{ij}S_{ij})^{1/2},$$

where Δ is the geometric mean of the grid spacing in each direction $\Delta = (\Delta x \Delta y \Delta z)^{1/3}$, and C the Smagorinsky constant with value C=0.027. The RVM model consists in separating the large scales and the resolved small scales to compute the strain rate of deformation based only on the small scales S_{ij}^s. The subgrid scale contribution now reads

$$\tau_{ij}^{sgs} = 2C\Delta^2 (2S_{kl}^s S_{kl}^s)^{1/2} S_{ij}^s.$$

The RVM model interacts with the wall model and is thus not suitable with bounded shear-flow [13]. Hence, the Smagorinsky model is used when an atmospheric boundary layer (ABL) is modeled, while the RVM is preferred for uniform inflows.

The spatial discretization of the convective term is performed using Vasilyev scheme that conserves exactly the discrete kinetic energy. However, when a wall model is added, the discretization was rewritten to allow an easier implementation of the wall shear stress boundary conditions [13]. The time integration is performed using the delta-form introduced by Lee *et al.* [14]. This integration method is chosen to ensure stability while keeping computational costs low, as described by Georges [15]. To assure that the obtained field is divergence free, a Poisson equation is solved and leads the pressure gradient that must be added to project the velocity into a solenoidal field. This increment of pressure is then added to the kinematic pressure.

The solution of the Poisson equation is the most requiring part of the numerical process, and great effort was put in its fast resolution. The solver implemented by Duponcheel [11] is a multi-grid solver. Multi-grid solver consists in the combination of the solution of the equation at various grid level, each working in mitigating its dedicated range of error frequency. This solver presents the advantage of an efficient parallelization. Here, the parallelization is performed efficiently by allowing the region handled by various processors to agglomerate and generate the coarser grid. This allows massive parallelization of the code while keeping the Poisson solver efficient.

The boundary conditions are enforced using 3 layers of ghost points in order to keep the 4th order precision at the boundaries. Dirichlet and Neumann conditions can be enforced, but unbounded flow cannot be handled yet.

Wall modeling Large velocity gradients appear in the near wall region of wall bounded shear flow. Their amplitude is even increased in an ABL as the Reynolds number is high and the ground is rough. The exact computation of the velocity field is this region would require an prohibitively fine mesh in the wall region. To overcome this limitation, a wall model based on the logarithmic law of the wall is introduced. This model consists in generating the proper wall shear stress to ensure a local equilibrium with the near wall logarithmic behaviour of the boundary layer. The friction velocity u_τ is obtained as

$$\frac{1}{u_\tau} = \frac{1}{\kappa |\langle \mathbf{u} \rangle|} \log(y/y_0),$$

with u_τ the friction velocity defined as a representative velocity of the shear stress at the wall, and $\kappa = 0.38$ the von Karman constant. The operator $|\cdot|$ stands for the norm of a vector, and $\langle \cdot \rangle$ is the spatial averaging operator. The friction velocity is found from the shear stress at the wall using the relation

$$\tau_w = \rho \frac{\mathbf{u}|\mathbf{u}|}{|\langle \mathbf{u}|\mathbf{u}| \rangle|} u_\tau^2.$$

Generation of the inflow turbulence The simulation of an ABL containing some wind turbines in a limited size computational domain is challenging as the effects of the wind turbine on the total pressure gradient are difficult to quantify. To overcome this limitation,

the inflow turbulent ABL is generated by running a precursor simulation which consists of a half channel with horizontal periodic boundary conditions and driven by a prescribed pressure gradient that compensates the wall shear stress as

$$u_\tau^2 = -\frac{dP}{dx}H.$$

The recovered velocity field is then transferred at the inflow of the co-current simulation, in which the wind turbines can be placed. The advantage of this approach is the faithful reproduction of the inflow turbulent structures. Nevertheless, it roughly doubles the computational cost. Also, some large turbulent structures are harder to break down if the lateral width of the computational domain is small.

2.2 Actuator models

Actuator models are a common method for the simulation of wind turbines interaction with their surrounding flow. Those models are able to retrieve correctly the forces acting on the blades and the important wake structures, while keeping the computation costs significantly lower than those of blade resolved simulations. The models consist in introducing a volumetric source term f in the Navier-Stokes equation,

$$\frac{Du}{Dt} = RHS + f.$$

The value of f is computed at control points based on the local velocity measured in the flow solver and on the blade element theory presented below. The forces on those control points are then redistributed on the surrounding grid points to ensure that the flow is properly affected and to avoid numerical instabilities. The location of the control points is the main variation between the actuator disk and the actuator lines approaches.

Blade element theory

The blade element theory allows to compute the forces acting on a blade by dividing it in a series of radial elements on which 2D aerodynamics stays valid. The airfoils experimental lift and drag coefficients are used with an effective angle of attack. The latest differs from the geometric angle of attack due to the downwash angle resulting from the circulation of the blades and in the wake. The flow angle ϕ is obtained through the measure of u_n and u_t, the axial and tangential velocities on the rotor, respectively,

$$\phi = \arctan\left(\frac{u_n}{\Omega r - u_t}\right),$$

and is used to computed the effective angle of attack of the blade α as

$$\alpha = \beta - \phi.$$

where β is the geometric blade angle including blade twist and the pitch angle.

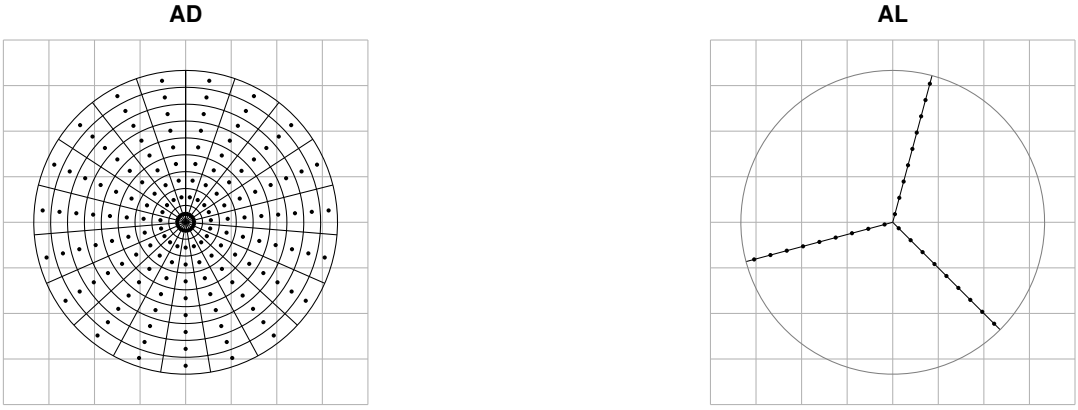

Figure 2.1: *Control points distribution for AD and AL approach*

The forces acting on the blade are then obtained from C_l and C_d, the lift and drag coefficient, respectively. Using the fluid density ρ and the blade local chord length c, the lift L and the drag D resulting from each blade elements are computed as

$$(L, D) = \frac{1}{2}\rho V_{rel}^2 c\Delta r(C_l(\alpha), C_d(\alpha)),$$

with V_{rel} the relative velocity felt by the blade element

$$V_{rel} = \sqrt{u_n^2 + (\Omega r - u_t)^2}.$$

Finally, the lift and drag, computed regarding the relative velocity are transferred to the rotor frame into a normal and a tangential component, F_n and F_t, respectively

$$F_n = L\cos(\phi) + D\sin(\phi), \qquad F_t = L\sin(\phi) - D\cos(\phi).$$

2.2.1 Actuator Disk with tip-loss correction

The Actuator Disk (AD) approach consists in the discretization of the surface swept by the rotor into radial and azimuthal elements, each of them having a control point at its center (see Figure 2.1). The local flow velocities are interpolated for every control point with a M_4' scheme and are used to compute the forces. The latter are then normalized to take into account the number of blades N_b and the ratio between the surface of the element and the annular section of radius r,

$$F_{n,AD} = F_n N_b \frac{\Delta S}{2\pi r \Delta r} \quad \text{and} \quad F_{\theta,AD} = F_\theta N_b \frac{\Delta S}{2\pi r \Delta r}.$$

Those forces are divided by the volume of one cell to be used as bulk force in the Navier-Stokes equation, after being redistributed on the surrounding mesh using an third order M_4 scheme.

The advanced actuator disk model developped by Moens [10] and used in this work also accounts for tip-loss correction. The latest is modeled using the Glauert tip-loss correction factor [16]. The disk accounting for an infinite number of blades, the circulation flow occurring at the tip that creates the discrete tip vortices cannot be captured. This leads to an overestimation of the forces at the tip and thus to an even more sensitive increase of the torque and power. The tip-loss correction fixes the induction that cannot be captured by a disk model. However, it still presents two disadvantages. Firstly, contrary to the induction, the wake structures are not corrected and the near wake is not accurately retrieved, especially at low tip-speed ratio [17]. The AD sheds a cylindrical vortex sheet whereas the real blades are followed by helical vortex sheets that quickly roll-up and concentrate at the tip and the root into discrete vortex tubes. This shortcoming does not impact the far wake, but the deviation of the wake obtained with the tilt of the turbines might be affected by those structures. Secondly, the tip-loss correction requires the value of the effective upstream velocity, which is not clearly defined in the case of a turbulent flow. Here, this upstream velocity is recovered using one dimensional momentum theory [10]. However, this assumption was never assessed with significant yaw or tilt effects, although the theory cannot be easily transposed for inclined wind turbines [18].

2.2.2 Actuator Lines

The Actuator Lines (AL) approach was developed by Sorensen and Shen [19] and provides an answer to the aforementioned problems. In this method, the forces are computed and distributed around virtual lines at the location of the real blades instead of on a disk (see figure 2.1). This better represents the rotor dynamics and its influence on the blade induction thanks to the modeling of separated blades. The normal and tangential forces F_n and F_t acting on the control points are transformed into bulk forces f and mollified around the lines using a regularization kernel η. This consists in a convolution product between the bulk force f, who acts as a dirac of forces, and the kernel

$$f_\eta = f * \eta.$$

The form of this regularization kernel is often discussed as it has an important influence on the power and forces that will be obtained using the actuator lines model. The most common kernel, used originally in [19] has the shape of a three dimensional gaussian function depending on the distance d between the actuator point and the flow solver grid point,

$$\eta_{3D} = \frac{1}{\pi^{3/2}\sigma^3} \exp\left(-\frac{d^2}{\sigma^2}\right).$$

The value of the standard deviation σ must be chosen with care as it adjusts the strength of the regularization. To avoid numerical instabilities, Troldborg [20] indicated that the minimal value for regularization was linked to the grid spacing h by $\sigma/h \geq 2$. However, concerns were raised that the use of a grid based σ does not accurately represents the tip behaviour due to the fact that the mollification expend beyond the tip of the blade. This led some authors to use the Glauert [16] or Shen [21] tip-loss correction . However, those corrections have no theoretical framework in the case of an AL method that solves the three dimensional flow around the blade. The above discussed uncertainties on the upstream velocity could also be problematic when used in turbulent flow.

This tip behaviour representation problem encouraged authors to mollify the forces more accurately by adapting the radius of the kernel to the local chord length, *i.e.* keeping $\sigma/c(r)$ constant. In their guidelines, Jha *et al.* [22] have shown that the effective angle of attack at the tip was better captured by using an equivalent elliptic chord distribution. By comparing the solution obtained with an actuator line and a potential flow, Martinez [23] obtained that the optimal agreement required $\sigma/c = 0.14, ..., 0.17$. However, using such a width is not possible in practice as it requires a very high resolution, which is not affordable in the case of farm simulations.

The idea to introduce a non isotropic gaussian was also studied by Churchfield et al. [24]. The distribution kernel is then defined as

$$\eta_{3D+} = \frac{1}{\pi^{3/2}\sigma_c\sigma_t\sigma_s} \exp\left(-\frac{d_c^2}{\sigma_c^2}\right) \exp\left(-\frac{d_t^2}{\sigma_t^2}\right) \exp\left(-\frac{d_s^2}{\sigma_s^2}\right)$$

where σ_c, σ_t and σ_s represents the standard deviation of the kernel in the chord, thickness and span directions, respectively. The distances between the mesh point and the control point of the actuator line are represented by d_c, d_t and d_s, also in chord, thickness and span directions. This modification led to exciting results as the near wake representation was more accurately captured, and the tip behaviour was tighter, removing the need of an artificial tip-loss correction.

However, the non-isotropic three dimensional gaussian kernel does not solve completely the issue that forces are distributed beyond the blade radius. Moreover, the use of this kernel induces overlapping between adjacent forces distributions. To solve this issue, the idea of removing the spanwise mollification was studied by Mikkelsen [25], Shives and Crawford [26] and Jha [27]. The mollification kernel is hence a two dimensional gaussian spread in chord and thickness directions

$$\eta_{2D} = \frac{1}{\pi\sigma^2} \exp\left(-\frac{d^2}{\sigma^2}\right)$$

with d the distance in a plane perpendicular to the line. The use of this regularization gave consistent results with the expected tip behaviour. However, some numerical oscillations were observed at the tip, due to the increased sharpness in this region.

In this work, both a non-isotropic 3D gaussian and a 2D gaussian were implemented in order to compare their performances. A complete description of the implementation of the actuator lines method as well as a discussion on the different distribution parameters is performed in Chapter 3.

Chapter 3

Actuator lines model

The actuator lines (AL) model, briefly introduced in section 2.2.2, presents some major advantages but also raised some new challenges in the accurate modeling of the wind turbines. This model accounts for the blades dynamics by computing the forces around virtual lines. It leads to an enhanced modelling of the near wake, which is one of the weakest point of the actuator disk (AD) method. This chapter aims at shedding some light on the behaviour of the AL method and at developing a way of distributing the forces that improves the critical tip behaviour of the blades. In this chapter, a first presentation of the implementation of the actuator lines method is performed. Then, the various mollification methods are assessed in uniform flow, and the method is verified regarding various operating conditions. Then, a comparison between the AD and the AL method is performed in a turbulent atmospheric boundary layer.

3.1 Improved actuator lines model

The actuator lines model consists in three main steps: the interpolation of the velocities from the flow grid to the wind turbine frame, the computation of the forces using the blade element theory and the distribution of the forces on adjacent grid points. The improved model especially focused on the distribution of this last step and is described in section 3.1.2. This also led to modify the velocity interpolation, which is first described in section 3.1.1.

3.1.1 Velocity interpolation

The actuator lines are in general not aligned with the mesh and the velocities obtained with the flow solver must be interpolated from the grid points. This interpolation can be performed using a M_4' kernel in all spatial directions, which is an isotropic interpolating function. But the AL method is improved by modifying the force distribution on the mesh using a non-isotropic smoothing kernel. The use of such a smoother installs uncertainty about the sampling of the velocity in the affected region. In fact, the forces computed at the control points are not spread on the surrounding mesh uniformly, leading to an uneven distribution of the circulation around the blade. Using an isotropic interpolating function is then quite biased and the velocity sampling must be adapted consequently. When the forces are mollified with a kernel η, the relative velocity felt by the blade element V_{rel} evolves with [24]

$$\mathbf{V}_{rel} = \iint_{-\infty}^{\infty} \mathbf{u}(x', y')\eta(x - x', y - y')dx'dy', \tag{3.1}$$

Here, this force mollification kernel is a non-isotropic three- or two-dimensional gaussian kernel (see section 3.1.2). The equation (3.1) can then not be used in this form as this gaussian kernel η is a smoother, not an ordinary interpolating kernel, as $\eta(0)$ is not equal to the unity. This means that the velocity sampled on the actuator lines would be weighted by different values of the surrounding flow datas, even when the line is perfectly aligned with the mesh. To overcome this effect, a new non-isotropic interpolating kernel must be defined, with a topology similar to the gaussian kernel η.

The interpolated velocity is defined as $\tilde{u}$ and is obtained from the convolution of the discrete datas u_i and the interpolating function W,

$$\tilde{\mathbf{u}}(\mathbf{x}) = \int_{-\infty}^{\infty} \mathbf{u}_i W(\mathbf{x} - \mathbf{x}_i)d\mathbf{x}.$$

An appropriate function $W(x)$ must be found for each direction. In order to mimic the topology of the distribution kernel for the force, while keeping the approximation of the velocity sufficiently local, it is chosen that the interpolation will use 2 grid points in the axial direction and 6 grid points in the tangential direction. The interpolation function is also chosen to be based on B-splines for the ease of use of their compact support. Hence, the axial function is the 2nd order spline $M_2(x)$ corresponding to the tent function, as defined in Cottet [28]. For the tangential direction, the sixth order B-spline $M_6(x)$ cannot be used as this kernel is not interpolating. We thus aim at building $M_6'(x)$, a fourth order interpolating function that has a support of 6 nodes, so that the new interpolation kernel reads

$$W(\mathbf{x}) = M_2(\mathbf{x} \cdot \hat{e}_x)M_6'(\mathbf{x} \cdot \hat{e}_y)M_6'(\mathbf{x} \cdot \hat{e}_z).$$

Following the work of Monnaghan [29], this new kernel will be built as a linear combination of $M_6(x)$ with its derivatives, such that

$$M_6'(x) = a_1 M_6(x) + a_2 x \frac{dM_6}{dx} + a_2 x^2 \frac{d^2 M_6}{dx^2}. \tag{3.2}$$

The conditions that must be fulfilled by the new interpolating function are

$$M_6'(0) = 1, \tag{3.3a}$$

$$\int_{-\infty}^{\infty} M_6'(x)dx = 1, \tag{3.3b}$$

$$\int_{-\infty}^{\infty} x^2 M_6'(x)dx = 0. \tag{3.3c}$$

Equation (3.3a) ensures that the kernel is an interpolating function, equation (3.3b) ensures the conservation of the integral and the last condition (3.3c) ensures that M_6' is a fourth order interpolating kernel (as M_6 is symetric). The combination of those conditions with equation (3.2) leads to the following coefficients, that define completely the interpolation function,

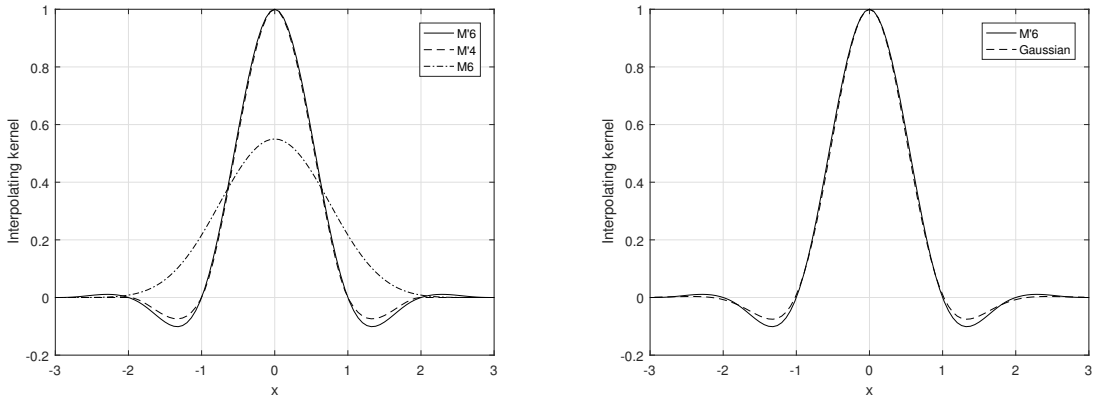

(a) *(b)*

Figure 3.1: *Comparaison of various interpolation kernel. (a) M_6', M_4' and M_6. (b) comparaison of M_6' kernel with a gaussian based one defined with the same conditions.*

$$a_1 = \frac{20}{11} \quad a_2 = \frac{33}{34} \quad a_3 = \frac{7}{66}.$$

The interpolation function M_6' is shown on figure 3.1a. The kernel is very similar to M_4' in the $|x| < 1$ region. It is also verified to have a compact support spread between $[-3, 3]$. On figure 3.1b, M_6' is compared to a kernel built by using the same constitutive rules expressed in equations 3.2 and 3.3, but using a Gaussian function with standard deviation equal to one as basis. The two schemes show similar behaviour, but the Gaussian one does not rely on a compact support, which would require to ensure that the integral is conserved at each interpolation, hence increasing the computational costs.

This interpolation kernel shows very good results in recovering correct induction when compared to the uniform interpolation kernel, But it has a little impact on the captured forces. A disadvantage of this ellipsoidal kernel is that its axes stay aligned with the mesh. Hence, interpolation in the tilted or yawed cases do not follow the exact topology of the smoothing kernel for the forces. For those reasons, this modified interpolation kernel will not be used for those cases. Also, for the sake of comparison, it will not be used when different forces distributions must be compared. In such cases, the M_4' uniform kernel is preferred.

3.1.2 Forces distribution

The mollification on the mesh can be performed using a 2 or 3D Gaussian kernel with non-uniform width in each directions. The 3D gaussian kernel requires firstly to compute the distance in the chord, thickness and span directions between the considered mesh grid point j and the control point i on the blade. A weight w_{ij} is attributed to the grid point using the gaussian formula

$$w_{ij} = \frac{1}{\pi^{3/2}\sigma_c\sigma_t\sigma_s} \exp\left(-\frac{d_{c,ij}^2}{\sigma_c^2}\right) \exp\left(-\frac{d_{t,ij}^2}{\sigma_t^2}\right) \exp\left(-\frac{d_{s,ij}^2}{\sigma_s^2}\right).$$

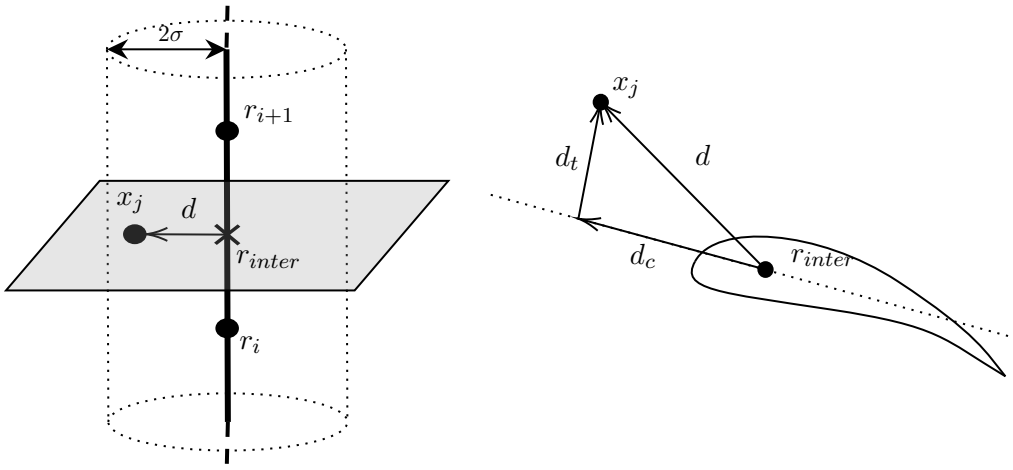

Figure 3.2: *2D kernel geometry*

To ensure that the integral of the force is conserved during the mollification, the weights are normalized for each control point of the blade

$$\hat{w}_{ij} = \frac{w_{ij}}{\sum_{j=0}^{n} w_{ij}}.$$

The total force on the grid point j induced by the N blade elements is then expressed as

$$f_j = \sum_{i=0}^{N} \hat{w}_{ij} \frac{F_i}{\Delta x \Delta y \Delta z}.$$

The use of a non-isotropic 3D kernel presents several advantages compared to the classical uniform distribution. First, the difference between σ_c and σ_t allows to distribute the forces in a direction similar to the pressure distribution of the airfoil. This increases the accuracy by taking into account the blade geometry and the pitch angle in the mollification. Second, The spanwise mollification can be decreased to avoid an expansion of the mollification far beyond the blade tip.

The 2D Gaussian kernel only requires the distance in the chord and thickness direction. A weight is attributed to the grid point j only if it belongs to a cylinder centered on the blade going from the hub to the tip and of radius twice as large as largest standard deviation σ, as depicted on figure 3.2. This weight of the mesh grid point j is obtained using the 2D gaussian formula

$$w_j = \frac{1}{\pi\sigma^2} \exp\left(-\frac{d_c^2}{\sigma_c^2}\right) \exp\left(-\frac{d_t^2}{\sigma_t^2}\right).$$

With this kernel, the weights are no longer normalized in each element surrounding a control point, but on the entire blade,

$$\hat{w}_j = \frac{w_j}{\sum_{j \in blade} w_j}.$$

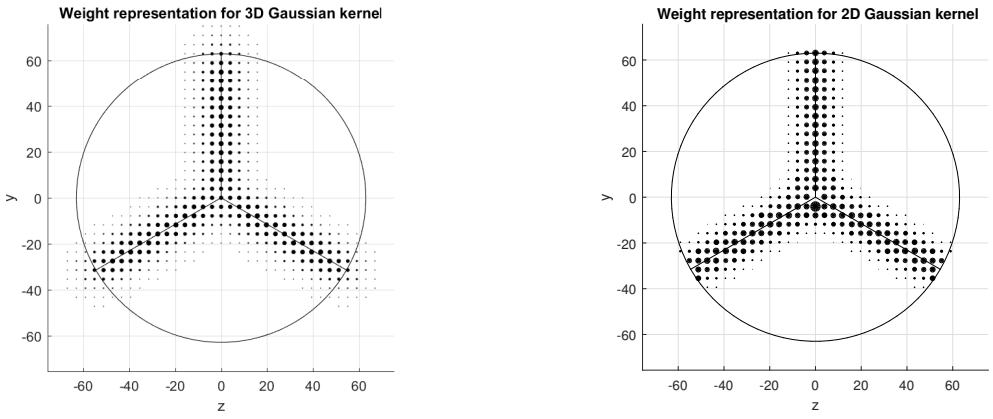

(a) 3D kernel *(b) 2D kernel*

Figure 3.3: *Comparison of distribution weights ($\sigma_c/h = 2$, $\sigma_s/h = 1$)*

This method was chosen to preserve the integral of the force on the blade while keeping the weight distribution sufficiently smooth to avoid non physical force gradients within the distribution. This could arise from the normalization on small elements with irregular number of included grid points.

A linear interpolation is performed between the control points in order to better represent the force distribution along the blade. The force at a radial distance r is thus given by

$$F(r) = \sum_{i=0}^{N} F_i M_2(r - r_i).$$

In the second half of the last segment, an extrapolation of the force should be carried. This is performed by enforcing $F(R_{tip}) = 0$.

The bulk source f_j added to the mesh point j is then given by

$$f_j = \hat{w}_j \frac{F(r_{inter})}{\Delta x \Delta y \Delta z},$$

with r_{inter} the radius on the intersection between the actuator line and the perpendicular plane including the considered grid point.

The weights for the two kernels are shown on figure 3.3. There is no force distribution beyond the blade tip in the case of a 2D gaussian kernel, which is likely to have a positive influence on the loads recovered in this region. However, a large force variation might appear in the tip region if a fine mesh is used.

3.1.3 Numerical constrains

One of the drawbacks of the AL method is the restrained stability condition. The blade tip can not go through more than one grid cell per time step. This gives the following condition, that is similar to the CFL condition for convection equation, based on the local tip velocity ΩR,

$$\frac{\Omega R \Delta t}{\Delta z} < 1.$$

This dimensionless number will be referred as the tip-CFL in the rest of this work.

The spatial resolution must be sufficient to capture the variation occurring on the blade. The lower limit is often set to 20 control points per blade. Usually, it is also advised to have the length of the blade elements smaller than the mesh spacing [22]. The effect of resolution will be assessed in the next section for a uniform inflow.

3.2 Characterization in uniform flows

In this section, we aim at characterizing our implementation of the AL method regarding several key parameters such as the topology and the width of the distribution kernel and the spatial resolution of the flow solver. The actuator disk with tip-loss correction (AD) will be used as reference, as it was validated against a high fidelity method [30]. In this section, simulations are performed with a uniform inflow exempt of turbulence. The reference machine considered is the NREL-5MW offshore wind turbine whose characteristics are extensively described in Jonkman [31]. This turbine has a diameter D of 126m and a hub height of 90m.

The objectives of those simulations is also to emphasize which of the implementation performs the best at a relatively coarse resolution, in order to use this method in wind farms. For that purpose, the discussion is structured around three main aspects. First, the behaviour of the instantaneous and the time averaged wake is assessed as the velocity deficit, vortex structure and turbulent kinetic energy play a major role in the interaction between different machines in a wind farm. Second, the local data of the blade such as the forces and, at a smaller extent, the induction, condition the design and lifetime of the machine. Thirdly, the power and the thrust must be considered as they consist in the final output of the wind turbine.

3.2.1 Influence of the kernel topology

3.2.1.1 Simulation parameters

The wind turbine is set in a domain of size 8Dx4Dx4D, and is placed at position 2Dx2Dx2D. Boundary conditions are inflow and outflow at $x = -2D$ and $x = 6D$ respectively. A no through condition is imposed in at y=$\pm 2D$ while periodic condition is used in the z-direction. The upstream velocity is chosen to be 9 m/s as this is the maximum of the power curve for the considered NREL-5MW. In those conditions, the rotor has an angular velocity of 10.3 RPM, which leads to a medium tip speed ratio of $\lambda = 7.55$. The pitch angle is set to zero for the blades and the pitch control is not active, so the pitch angle stays constant through the entire simulation. The grid resolution is set to 48 points per diameter in each direction which gives 24 points per blade. This resolution was chosen as it stays computationally acceptable and complies with the usual spatial resolution requirements. To ensure stability, the time step Δt is chosen as 0.025 seconds, which leads to a tip-CFL of 0.65. The simulations are performed on 16000 time steps (400 seconds), which gives 3.6 convective times. The two first convective times are required for the flow to converge statistically. The rest of the simulation is then used to compute statistics on the flow, as well as the power and the forces on the blades.

3.2.1.2 Assessed Methods

This set of simulations aims at comparing various mollification of the forces with the AD reference. The five assessed cases are summarized in table 3.1. Three 3D gaussian kernels are compared: AL3Du is uniform in each direction, AL3D has a reduced width in the span and thickness directions, and AL3Ds stays non-uniform but the width is reduced in all directions. One 2D kernel (AL2D) is also tested, with ratios similar to AL3D. For the sake of comparison, M_4' was also kept as interpolating function, and it hence plays no role in the relative comparison.

Abbreviation	Topology	Interp.	Distrib.	σ_c/h	σ_t/h	σ_s/h
AL3Du	Uniform 3D	M_4'	Gaussian	3	3	3
AL3D	Non-uniform 3D	M_4'	Gaussian	3	1.5	1.5
AL3Ds	Non-uniform 3D sharp	M_4'	Gaussian	2	1	1
AL2D	Non-uniform 2D	M_4'	Gaussian	3	1.5	-
AD	Uniform 3D	M_4'	M_4	1*	1*	1*

Table 3.1: *Summary of the assessed methods. The symbol * refers to the equivalent gaussian width.*

3.2.1.3 Results and discussion

The typical vortex structure behind a wind turbine consists in three parts [32, 33]. In the near wake, the vortex tubes shed by the tip are advected in an helical path following the wake boundary. Then, those discrete structures sort of merge into a continuous vortex sheet. Further in the wake, this "bumpy" vortex sheet becomes unstable due to Kelvin-Helmholtz instabilities. Eddies are formed and the slipstream becomes turbulent. Those three states can be clearly observed on figure 3.4 that shows the isocontours of the vorticity obtained with AL2D. In the rotor plane, the bound vortices representing the blades can also be observed.

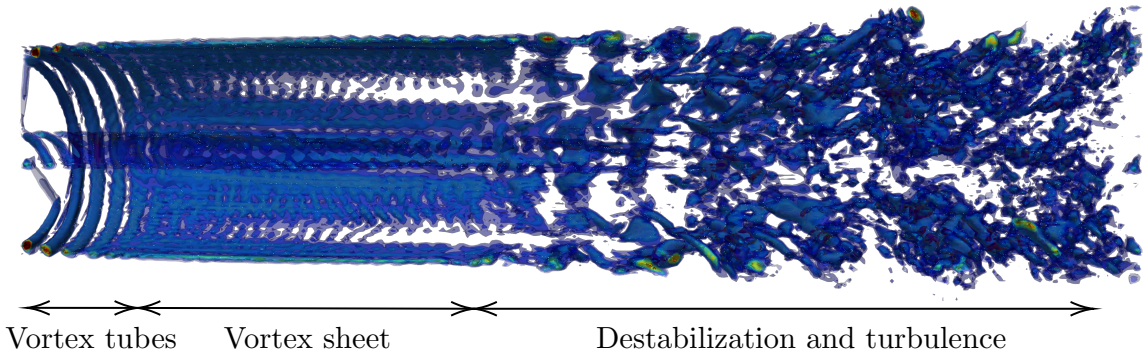

Figure 3.4: *Iso-contour of vorticity behind a wind turbine simulated with the AL2D method.*

Figure 3.5 shows slices of the vortex structure in the wake and in the rotor plane for the different methods. The AD sheds a continuous vortex sheet while the AL method sheds discrete vortex tubes. Though, the demarcation between the tubes is reduced when the mollification is increased. The AD is also not able to capture the bound vortices at the blades. The effect of the blades is spread uniformly over the disk surface, and so is the vorticity distribution. On the contrary, the AL method managed to retrieve the bound vortices, but with a various intensity depending on the method.

The intensity of the shed vortices and the distance where the wake starts being unstable differs from one method to another. Those variations are mostly driven by the value of the spanwise mollification. The larger the ratio σ_s/h, the later the shear layer gets unstable. The similarity with the AD and AL3Ds is attributed to their equivalent kernel width in that direction. On the contrary, AL2D and AL3Du predict very different behaviour. The mollification in the chord and thickness directions seems to have no impact on the wake destabilization, as AD and AL3Ds exhibits similar behaviour even if AL3Ds is wider in the chord direction. Also, AL2D and AL3D who have the same chord and thickness distribution exhibits discrepant behaviours. The importance of the spanwise mollificaton is explained by the fact that reducing its value creates and thinner vortex sheet whose tendency to become unstable is increased.

The spanwise mollification also has an influence on the amplitude of small high frequency vortex oscillations appearing near the tip region. Those oscillations are often visible in other authors works [34]. This issue was solved in [22] by adding some numerical diffusion using 10% of upwinding upstream. However, this technique was not developped in this work as the amplitude of those oscillations does not seem to have a major influence on the obtained results.

In the rotor plane, the bound vorticity also exhibit varying intensities between the different AL methods. Although its integral is conserved between the methods as it is related to the local lift force, the distribution on the grid is different. Reducing the kernel size in the chord and thickness directions tends to increase the intensity. Both directions have an impact, as it clearly appears that the bound vorticity in the case AL3Du are far smaller than that of the AL3D one, even if their chordwise mollification is the same.

Figure 3.6 shows the time-averaged velocity deficit in the wake at various position. Good general agreement is observed between the different methods. Closer investigations highlight that sharply distributed AL methods present larger velocity gradients in the hub and the tip regions. More through flow is allowed at the center of the rotor as the forces are not distributed before the hub. Also, the velocity deficit shown by AL2D at $x/D = 6$ presents more diffusion near the tip region than the one obtained with the other methods. This is related to the faster transition to turbulence in the wake, that will accelerate mixing and thus the re-energizing process of the wake compared to the other methods. On the contrary, AL3Du exhibits a smooth behaviour at the hub and tip, but the velocity deficit stays important in the far-wake compared to other methods.

Forces, thrust and power

Figure 3.7 shows the forces acting on each element of the blade. It must first be observed that all methods shows a general good agreement with the AD, especially for the normal forces.

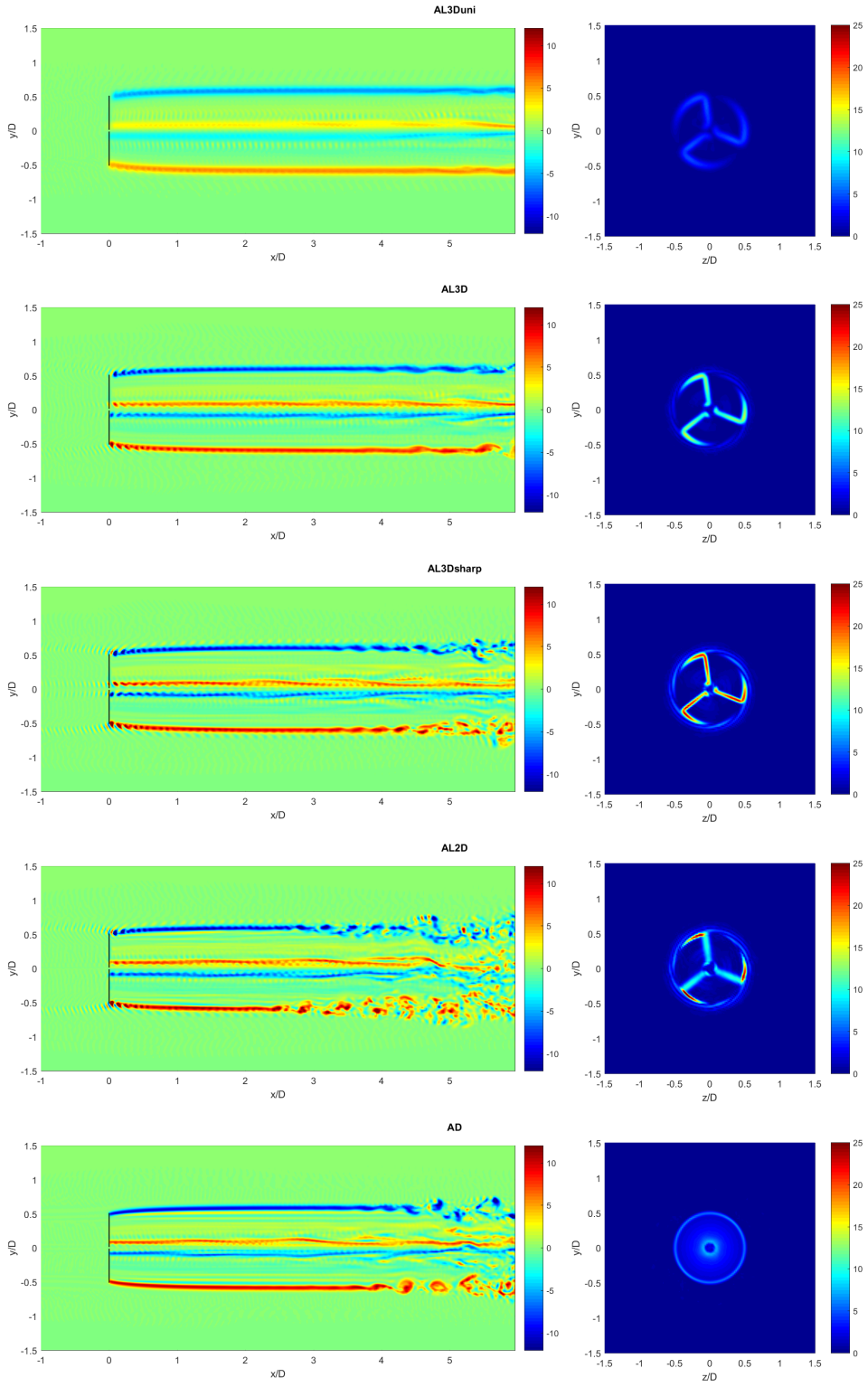

Figure 3.5: *Vertical slices of the vorticity and its norm in the rotor plane. From up to down: AL3Du, AL3D, AL3Ds, AL2D and AD. The vorticity magnitude is normalized using the factor* D/U_∞.

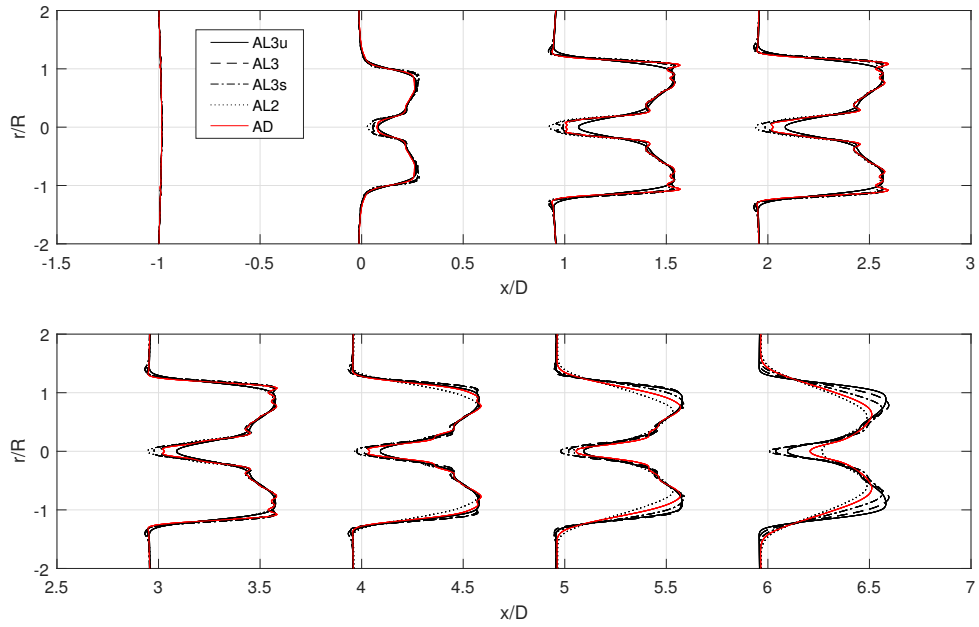

Figure 3.6: *Mean streamwise velocity deficit* $\frac{U-u}{U}$ *downstream of the wind turbine for the various methods.*

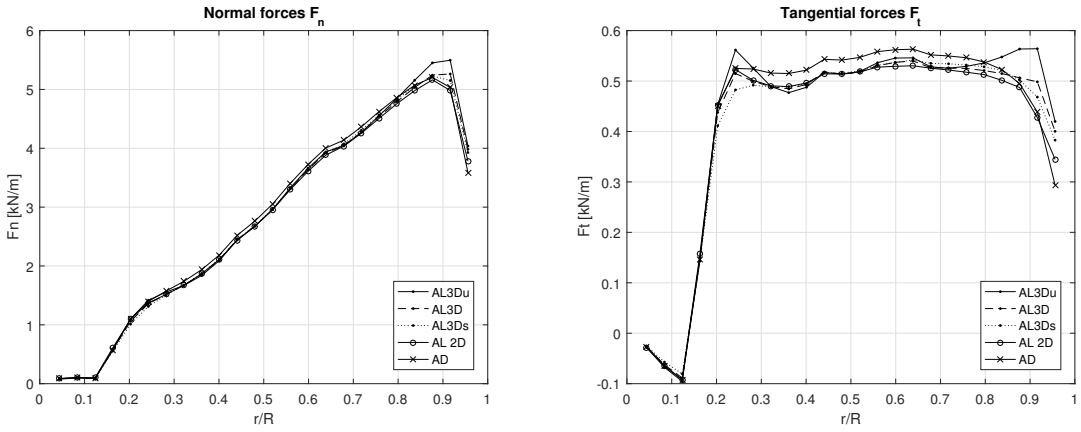

Figure 3.7: *Normal and tangential force per blade element length for the various considered methods.*

The AD produces slightly larger forces within $0.2 < r/R < 0.8$. This behaviour is explained by the small size of the computational domain, that is conductive to blockage effects. In fact the disk surface represents 4.9% of the surface of the transverse domain, and the proximity of the boundary conditions will impact the recovered quantities. The AL methods suffer less from those blockage effects.

The collapse of the force in the vicinity of the tip is captured by the AL, with a success relative to the used method. The width of the spanwise mollification seems to play a de-

terminant role in the apprehension of this decrease and best agreement is found for the 2D kernel (which has no spanwise mollification). This effect is attributed to the reduction of the mollification beyond the tip, which creates nonphysical forces on the flow further from the blades.

The variation of the power and the thrust compared to the results obtained by Moens [30] with a vortex particle-mesh method is depicted in Table 3.2. There is a general offset with the reference for all methods. This behaviour is here due to the blockage effects resulting from the small size of the computational domain. The power obtained with the AL methods differs importantly according to the mollification. The uniform 3D mollification largely over-predicts the recovered power and thrust. The prediction is improved when the kernel is not uniform. Moreover, sharpening the kernel slightly corrects the prediction. The accuracy is further increased when using a 2D gaussian kernel.

	Reference	AL3Du	AL3D	AL3Ds	AL2D	AD
Thrust	500.6 [kN]	+6.0%	+4.7%	+4.5%	+3.6%	+3.1%
Power	2930.8 [MW]	+13.3%	+9.5%	+9.0%	+6.4%	+4.4%

Table 3.2: *Power and thrust obtained for the various methods*

Conclusion on the topology

Consistent results were obtained with the AL methods, and some non-negligible differences were noticed according to the chosen mollification kernel. In particular, the spanwise mollification appears to be a critical parameter. It influences the wake destabilization, leading to a variation of the vorticity in the wake and of the dispersion of the mean velocity deficit. The force distribution was in better agreement with the AD model with a smaller spanwise mollification, without adding any artificial tip-loss correction. Finally, the predicted power and thrust approached the reference value as the spanwise mollification was reduced. The best concordance was found for the 2D gaussian kernel, that has no spanwise mollification. The absence of overlap between the blade elements and of force distribution beyond the tip are clear assets of this mollification. This kernel will thus be preferred in the rest of this work to simulate wind turbines.

3.2.2 Influence of the resolution

The objective of this work being the study of the tilt angle of wind turbines in a wind farm, large domains will have to be considered. Working at high resolution in such domains requires very large computational capacities, and reducing the resolution is thus desirable. A decrease from 48 to 32 points per diameter already cuts drastically in the simulations cost. However, although the AL method with a 2D kernel succeeds at capturing the behaviour of the wind turbines at an intermediate resolution, this performance is not guaranteed at a coarser resolution. The objectives of this section are to study the influence of the grid coarsening on the behaviour of the AL method, and verifying that the aforementioned conclusions still hold.

For that purpose, the computational domain was modified from 4x4x9D to 6x6x12D to remove blockage effects, and the resolution was coarsened from 48 to 32 grid points per di-

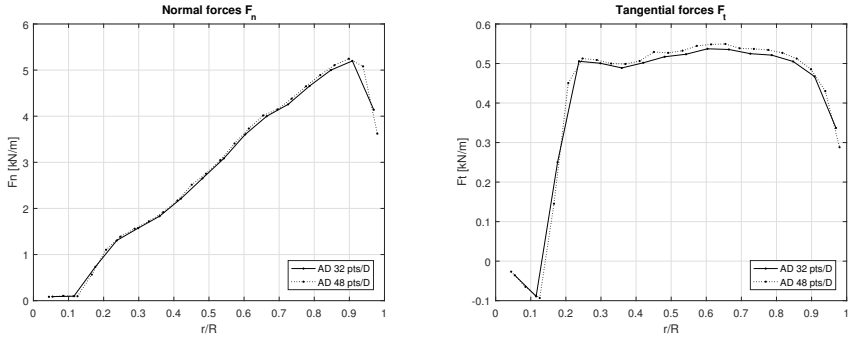

(a) Actuator Disk

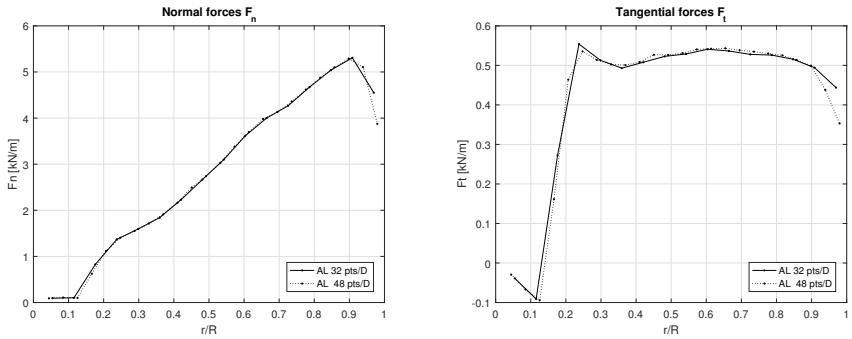

(b) Actuator Lines

Figure 3.8: *Forces distribution variation when the computational domain is modified*

ameter. This keeps the computational costs equivalent to the previous case. Coarsening of the grid also relaxes the constrain on the time step, as the grid cells are larger, so that the time step can be increased to 0.04 seconds while keeping the tip-CFL sufficiently low. The number of control points on the blade is kept equal to the number of grid points per blade, i.e. 16 points per blade. Other parameters are kept constant regarding the previous configuration.

Figure 3.8 shows the forces distribution of the actuator disk and actuator lines when the domain is increased and the resolution coarsened. First, the AD with tip-loss correction is not very grid sensitive. Except for a small lowering of the forces due to the increase of the domain size, the tip-losses are accurately recovered. This is due to the fact that the correction of the disk is somehow artificial, and has less dependency on the surrounding flow. Conversely, the AL method shows more dependency on the grid, and the forces collapse at the tip is not as steed at coarser resolution. This is due to the fact that the tip behaviour is dependent on the local flow whose calculation accuracy is decreased when the mesh is coarsened.

The vorticity behind the wind turbine is displayed on figure 3.9. The discrete vortex tubes that were observed in the vicinity of the tip on figure 3.5 are not recovered in the coarse case. Those vortex structures require multiple grid points to be spread on, and the coarsening tends to enlarge them. The larger shed vortex tube will thus be closer to the one generated by the preceding blade. This leads a quicker merging, that results in a continuous vortex sheet directly after the rotor, similarly to the one observed behind the AD. This near

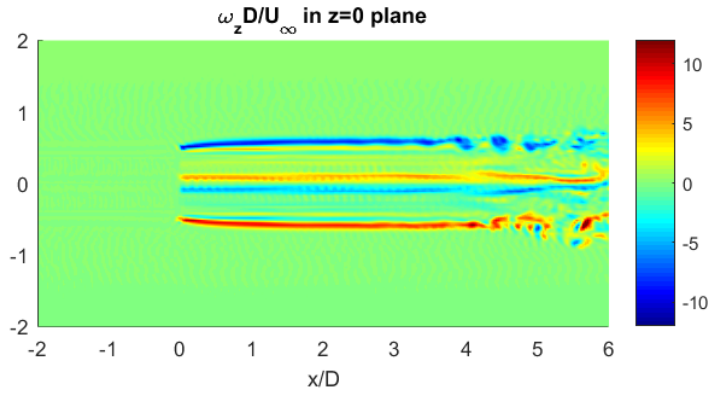

Figure 3.9: *Vorticity in z direction in the vertical plane*

wake behaviour explains why the forces distribution is deteriorated at coarse resolution. The reduced interval between the vortex tubes increases the interactions between the different blades. Those interactions tends to alleviate the circulation flow at the tip and reduces the effect of the separated blades.

The power extracted by each method is also altered consequently to the modification of the forces distribution. The disk prediction is reduced by 0.9%, due to the reduction of the blockage effects. On the contrary, the AL method increased its prediction by 1.7%. The total difference between the two methods is thus increased to 4.6%. This stays a reasonable difference, but the divergence of the behaviour of both methods when the resolution is coarsened is clearly sensible.

3.2.3 Influence of the kernel width

The side-effects of coarsening on the behaviour of the AL could be alleviated by an appropriate width of the mollification kernel. Simulations were thus performed with various values of kernel width in the chord direction σ_c or in the thickness direction σ_t, aiming at understanding the importance of those parameters. Six simulations were performed in the same conditions than the ones described in the section 3.2.2 and the distribution function parameters were varied in each case. Three simulations used a non-uniform distribution kernel whereas the three others used a uniform distribution. Each of the set had one sharp, normal and large width, whose parameters are synthesized in Table 3.3. The comparison will mostly focus on recovering an appropriate repartition of the forces on the blades, as well as a better prediction of the power.

Effect of the chordwise mollification σ_c

The effect of the chordwise mollication is assessed by comparing kernels with various σ_c/h while keeping σ_t/h constant. The variation of the forces is displayed on figure 3.10. First, it is observed that the mollification width is an important yet not dramatic parameter, as all curves have a similar aspect, especially in the normal direction. Larger discrepancies are found in the tangential force, with an uneven impact along the blades. The forces near the hub increase when σ_c is enlarged. Although this increase is not consistent with the AD, it has

Kernel full name	Abbreviation	σ_c/h	σ_t/h
2D non-uniform sharp	$AL2D_{2,1}$	2	1
2D non-uniform	$AL2D_{3,1}$	3	1
2D non-uniform large	$AL2D_{4,2}$	4	2
2D uniform sharp	$AL2D_{1,1}$	1	1
2D uniform	$AL2D_{2,2}$	2	2
2D uniform large	$AL2D_{4,4}$	4	4

Table 3.3: *Parameters and denomination of the various kernels*

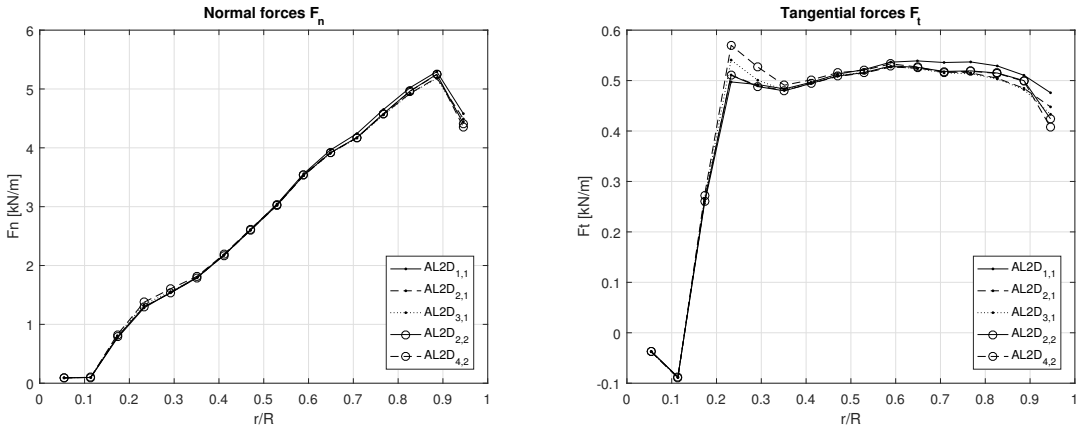

Figure 3.10: *Comparison of the force distribution for various mollification width in the chord direction. The curves with dots represents the variation of σ_c/h with $\sigma_t/h = 1$. The curves with circles have $\sigma_t/h = 2$.*

a limited impact on the recovered power due to the proximity to the rotor center, that limits the resulting torque. This behaviour is explained by the superposition of the mollification kernel of the three blades in the vicinity of the hub when the width is increased. At the tip, increasing the width helps recovering the forces collapse. A larger mollification thus appears to increase the sensitivity of the blade to the surrounding flow effects. Interestingly, a very sharp kernel ($AL2D_{1,1}$) gives disappointing results, explained by the inability of the flow solver to recreate large velocity gradients in the second part of the blade when the body forces are distributed on a small number of grid points.

Effect of the thickness mollification σ_t

The mollification in thickness direction is expected to have an impact on the shed vortex tubes at the tip. The larger the width, the more inflated the tubes will be. The advection of the structures away from the rotor will thus require more time, and the interaction between the blades will be enhanced. Figure 3.11 shows the force distribution for kernel with constant σ_c but various σ_t. Again, the largest discrepancies are observed in the tangential distribution of forces. The width in the thickness direction have negligible influence on the near hub behaviour, contrary to the chordwise mollification. The tip behaviour is more correctly represented when the thickness mollification is increased. However, the pre-tip forces are increased

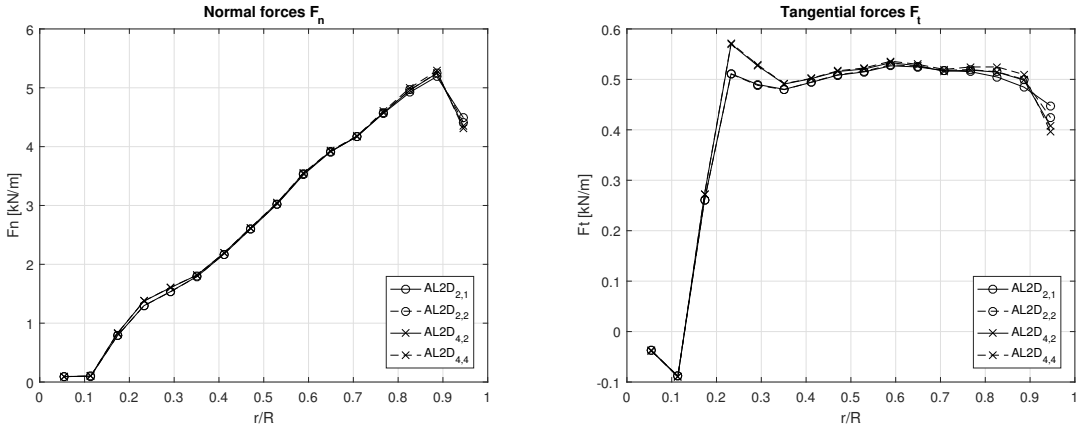

Figure 3.11: *Comparison of the force distribution for various mollification width in the thickness direction. Curves with dots illustrates the variation of σ_t with $\sigma_c/h = 2$. Circled curves have $\sigma_c/h = 4$.*

when σ_t is increased. This behaviour diverges from results obtained with actuator disk or finer resolved actuator lines. Also, this increase in the pre-tip region of the blade will create an important increase in power which will supplant the reduction achieved at the last control point.

Impact on power and thrust

Table 3.4 gives the power and thrust for the considered methods. All the recovered values tends to over-predict the reference values from the AD. The 2D non-uniform kernel with $\sigma_c/h = 3$ and $\sigma_t/h = 1$ presents the best behaviour. As it was observed that the normal forces were not really dependant on the mollification width, the thrust value is less sensitive than the power value. The latter varies from 4.5% to 7.9%, emphasizing the importance of a well chosen kernel. The sharp kernel $\text{AL2D}_{1,1}$ presents the most spurious results with a large overestimation. The use of non-uniform kernel also seems to improve the recovered quantities.

With a range of 3.4% of variation in power, the differences due to the kernel width are significant, yet their impact is relatively small compared to those introduced when the grid was coarsened. It was in fact verified (not shown here) the discrete wake structure were not recovered, even by sharpening the mollification. Using the AL methods at a coarse resolution will thus lead to a slightly overpredicted tip forces and power.

	AD	$\text{AL2D}_{2,1}$	$\text{AL2D}_{3,1}$	$\text{AL2D}_{4,2}$	$\text{AL2D}_{1,1}$	$\text{AL2D}_{2,2}$	$\text{AL2D}_{4,4}$
Thrust	512.3 kN	+1.9%	+1.9%	+2.4%	+3.1%	+2.0%	+2.7%
Power	3031.4 kW	+4.7%	+4.5%	+5.4%	+7.9%	+4.8%	+6.0%

Table 3.4: *Power and thrust extracted from the various models*

3.3 Validation at various upstream velocities

This section aims at validating the AL method in a uniform flow for various operating points of the wind turbine. Those operating conditions are summarized in Table 3.5. The purpose is to verify how the upstream velocity can affect the results obtained with the AL, and also to perform a more complete verification by investigating the major aspects of the rotor data.

u_∞ (m/s)	RPM	λ	pitch (^{o})	Δt	tip-CFL
14	12.1	5.7	8.7	0.03	0.57
9	10.30	7.55	0	0.04	0.65
5	7.76	10.24	0	0.05	0.61

Table 3.5: *Operation conditions of the wind turbine*

The AD with tip-losses correction and the AL simulations were run in the same computational domain as described in section 3.2.2. The time step is adapted to keep the tip-CFL close to 0.6 for all the computations, as it was verified that this value did not imply major stability issues. Each simulation was run on four convective times, the two first being necessary for statistical convergence of the flow, and the two lasts are used to compute the time-averaged quantities. The discussion is here structured around the parameters impacting the rotor: the forces acting on the blades, the induced velocities, and the recovered power and thrust.

Forces The forces distribution represented on figure 3.12 is very similar for the AD and AL models. Except for the case $\lambda = 7.55$, the tip behaviour is globally well captured. This exception can be related to the vortex structure behind the rotor. In the $\lambda = 5.7$ case, the high upstream velocity convects the vortex tubes quickly and decreases the interaction between the blades, leading to a correct tip behaviour. For the $\lambda = 10.24$ case, the high tip speed ratio increase the interaction between the blades and the tip-loss correction is reduced, what reduces the variation between the AD and AL methods. The case $\lambda = 7.55$ is thus a particular case, where the advection is not sufficient to separate the thickened trailing vortices of each blades, even if this behaviour is physically expected.

Blades local velocities The local velocities measured at the blades, shown on figure 3.13, present some differences between the AD and the AL model. Near the hub, the small discrepancies that can be observed with the AL method actually matches the results that were observed with the high resolution vortex particle-mesh (VPM) method [30]. In fact, the axial induction should tend to 1 at the hub, and the tangential one should tend to zero, a tendency that is more noticeable in the AL results. Also, the variation of the axial induction observed at roughly 60% of the blade in the $\lambda = 5.7$ case were verified to be due to the variation of the blade geometry instead of a miscalculation due to the method.

The AL method appears to recover an induction lying between the uncorrected and the corrected disk induction at the tip. The large increase in axial induction was also obtained with the VPM method and in Martinez *et al* [34]. The origin of this variation is the interpolation that goes beyond the blade tip, and a small value of unperturbed velocity is thus sampled.

A surprising results is the difference in tangential velocities that can be observed for the cases $\lambda = 5.7$ and $\lambda = 10.24$. The AL method overpredicts the tangential induction compared

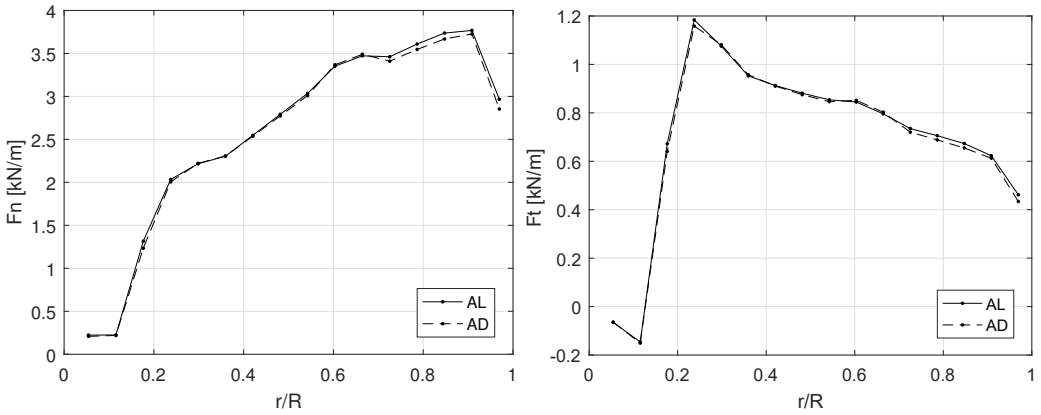

(a) $\lambda = 5.7$

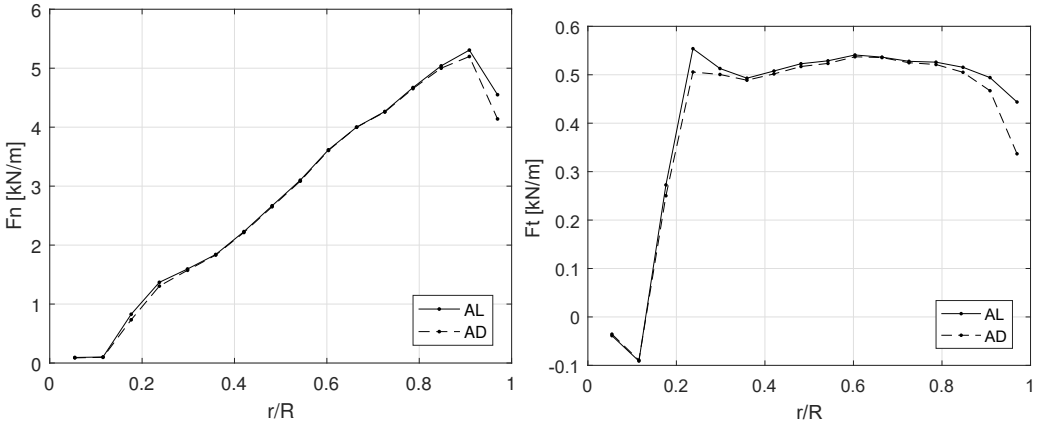

(b) $\lambda = 7.55$

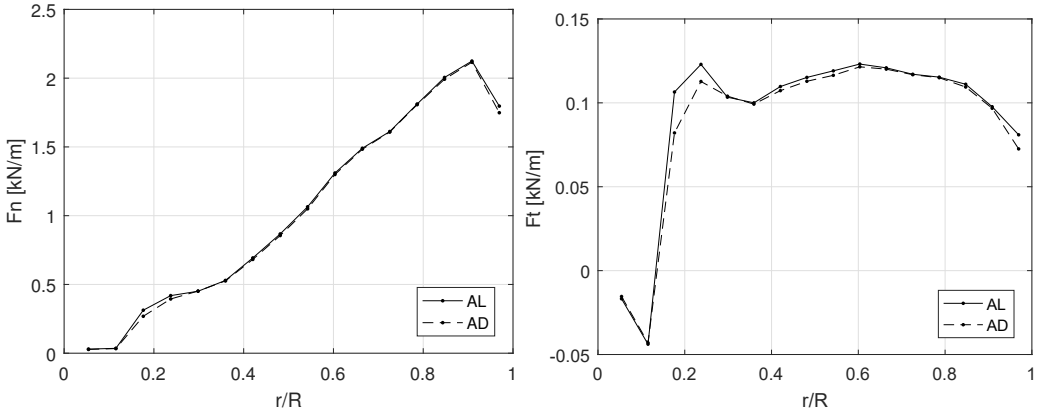

(c) $\lambda = 10.24$

Figure 3.12: *Forces distribution for the various operating conditions.*

to the AD model. Those discrepancies have a small influence on the angle of attack, as this tangential induction is almost negligible compared to the the large angular velocity. However, the case $\lambda = 5.7$ and $\lambda = 10.24$ were run with the uneven interpolation kernel derived in section 3.1.1, and the recovered induction is superposed on figure 3.13. Interestingly, the

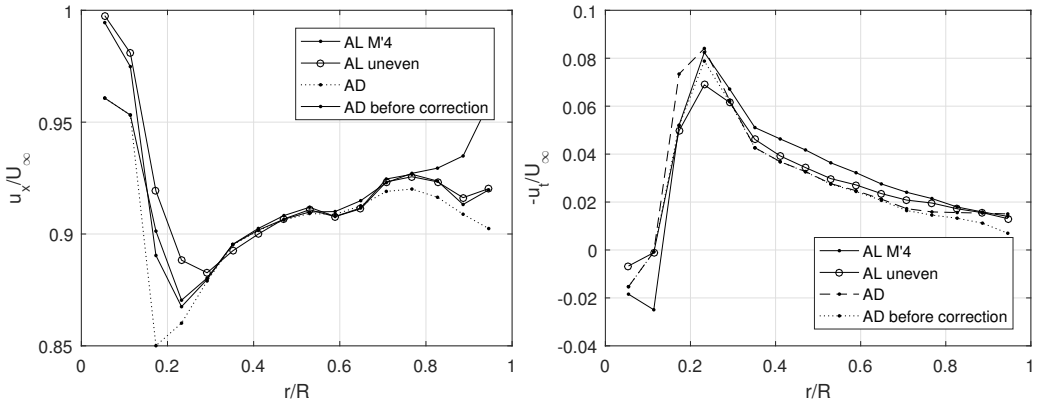

(a) $\lambda = 5.7$

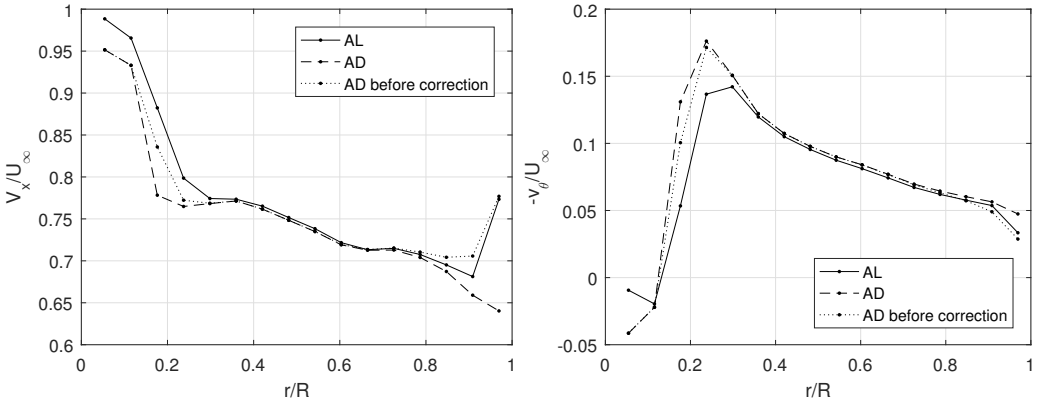

(b) $\lambda = 7.55$

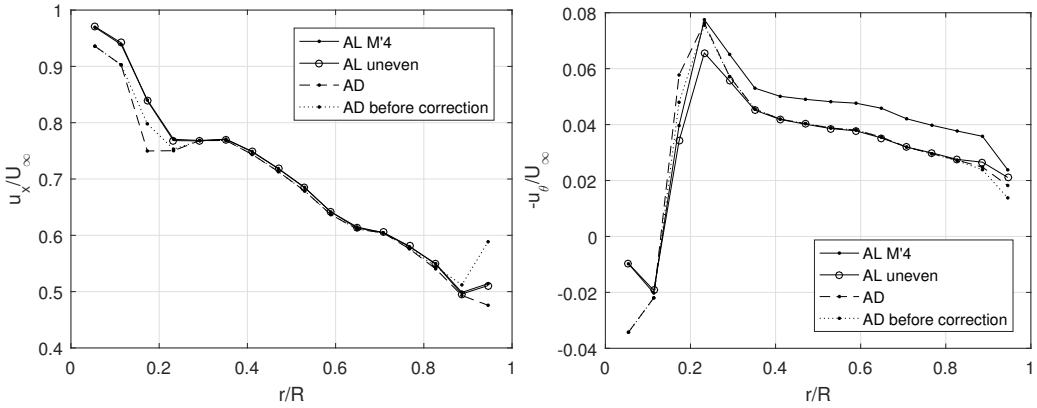

(c) $\lambda = 10.24$

Figure 3.13: *Blades local velocities for the various operating conditions*

predicted induction is clearly enhanced compared to the M_4' interpolation. This emphasizes the need of a proper interpolation mimicking the distribution behaviour if the local velocities have to be captured correctly. It also verifies the good results obtained with the modified interpolating function.

Power and thrust The time-averaged power and thrust generated by both methods are summarized in Table 3.6. Similarly to what was observed with the forces, the case $\lambda = 7.55$ overpredicts the power by 4.5%, whereas the power predicted by the other method is closer to the reference. The methods also predict a similar value for the thrust, due to a general good agreement of the normal forces. In general, the differences are reasonable for both quantities, and the AL method provides a correct estimation of the extracted power and thrust.

	Actuator Disk		Actuator Lines			
u_∞	Power [kW]	Thrust [kN]	Power [kW]	Variation	Thrust [kN]	Variation
14 m/s	5468.3	467.9	5546.0	+1.4%	473.4	+1.2%
9m/s	3031.4	512.3	3167.8	+4.5%	522.1	+1.9%
5 m/s	498.2	188.5	511.5	+2.7%	190.9	+1.3%

Table 3.6: *Power and thrust*

3.4 Actuator lines in an atmospheric boundary layer

In the previous section, the AL method was verified in uniform flow against the advanced AD method. In this section, the method is verified in the case of a turbulent inflow consisting in a turbulent atmospheric boundary layer (ABL). The nature of this inflow will affect the behaviour of all the aspects previously studied in uniform flow. The wake is destabilized earlier due to the interaction with the surrounding eddies. The forces acting on the blades become unsteady due to the velocity fluctuations and the sheared inflow. The power and thrust also become time dependant.

The objectives are to understand the influence of the turbulent inflow on the wind turbine and to verify how the model will handle the new characteristics of the flow compared to an AD with tip-loss corrections. Also, we aim at confirming that a relatively coarse resolution produces sufficiently accurate results, so that larger farm simulations can be performed with an adequate reliability. The numerical set up is first presented. Then, the loads, power, thrust and the wake behaviour are compared for the different cases.

3.4.1 Numerical setup

The presented simulations are performed in a domain of size 10Dx8Dx4D depicted on figure 3.14. The boundary conditions are periodic in the x- and z-directions. At the ground, the velocity is imposed by a logarithmic wall model based on the law of the wall for rough ground, as detailed in section 2.1. The upper boundary condition enforces no-through flow.

The methods are assessed at two resolutions. The high resolution has 64 points per diameter at the height of the rotor, whereas the coarser one has 32 points per diameter. The total grid consists in 512x256x256 or 256x128x128 grid points for the fine and coarse cases, respectively. In the vertical y-direction, the grid is uniform and has 64 or 32 points per diameter for the 200 first meters, and thus $\Delta z = \Delta y$. It is then stretched until the upper boundary, as the upper part of the flow can be solved coarsely. The grid spacing is uniform in the horizontal $x-$ and spanwise $z-$directions, but the spacings are different and set to

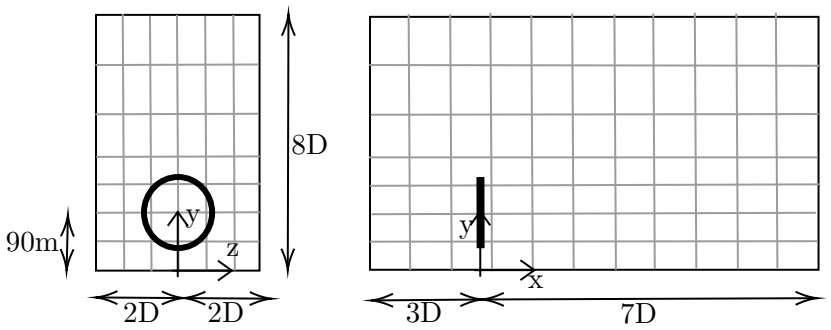

Figure 3.14: *schematic of the computational domain*

Δx=1.25Δz. Those grid characteristics are sketched on figure 3.14, with a reduced number of points for the sake of clarity.

To generate an atmospheric boundary layer whose characteristics are not affected by the presence of a wind turbine, concurrent simulations are considered. The main one actually involves the wind turbines, while the auxiliary one is used for generating the inflow conditions. For the ABL simulation, the value of the imposed pressure gradient is chosen so that the mean (*i.e.*, time-averaged) speed at hub height (*i.e.*, at 90 m) is 9m/s. This velocity is also chosen as the reference upstream velocity denoted U_∞ The ground roughness is set to impose a turbulence intensity that reaches about 6% at hub height. The statistics of the recovered ABLs are found in appendix A. It was verified that the ABLs obtained from both resolution were sufficiently close so that a fair comparison can be carried.

The wind turbine simulation is performed on a similar domain, with the rotor located as depicted on figure 3.14. In the x-direction, the boundary conditions are set to inflow/outflow conditions. The inflow is extracted from a vertical slice in the middle of the ABL domain. The model used for the turbine is the AD or the AL method described in previous sections. For the AL method, the forces computed from the flow are distributed with a non-isotropic 2D Gaussian kernel with $\sigma_c/\Delta z = 3$ and $\sigma_t/\Delta z = 1$. The flow velocity on the blades is obtained from the surrounding grid using the modified interpolation kernel presented in section 3.1.1. No controller is added, and the rotation speed is kept constant at 10.3 rpm. To ensure stability, the time step is set to $\Delta t = 0.04s$ in the coarse case and $\Delta t = 0.02s$ in the fine case, so that the local tip-CFL for the AL cases is 0.65. The total simulation time is 560 seconds which corresponds to 4 convective times. The first two are necessary to obtain a statistically converged flow. The last two are then analyzed to extract relevant data for the power, thrust, unsteady loads and wake characteristics.

3.4.2 Results and discussion

3.4.2.1 Time-averaged loads

Figure 3.15 depicts the time-averaged forces acting on the blades. Within the same resolution, the total forces obtained with the AD or AL model show good concordance, except from a small offset. The AL method tends to predict a slightly higher value, especially for the tangential force. Surprisingly, this offset is uniform on the entire blade, whereas it was mostly

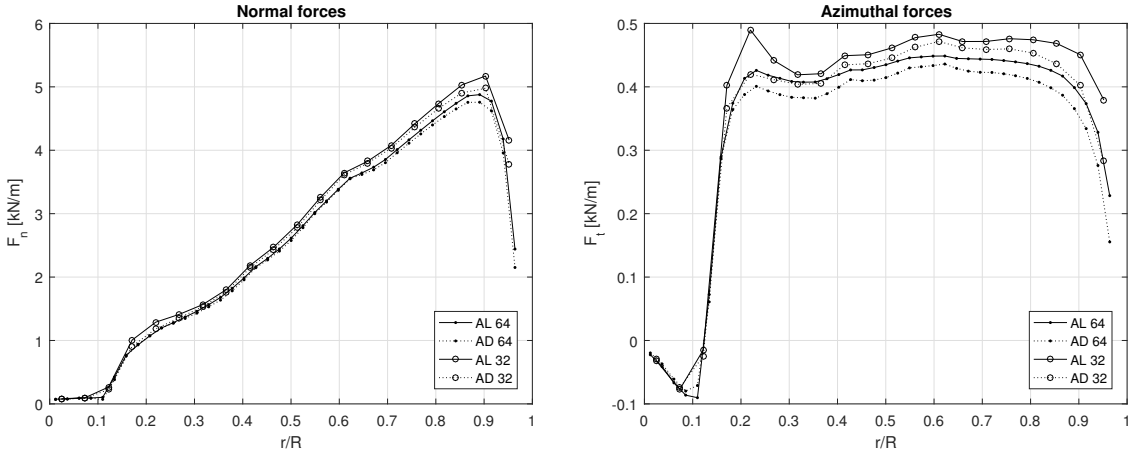

(a) Normal forces *(b) Tangential forces*

Figure 3.15: *Comparison of time-averaged forces on the blades for AL (solid) and AD (dots) for fine (points) and coarse (circles) resolution.*

located in the tip region in uniform flow. Apart from this offset, the curves aspects are very similar. The forces in the tip region captured with the AL method at fine resolution present a slightly more sudden decrease that was also observed with the VPM method [10]. This effect confirms the advantages of the 2D mollification, that allows to recover a correct behaviour without adding any further correction. In coarse resolution, the AL struggles to obtain such a collapse in the tip region, and the force decreases slower than with the AD, as it was already observed in uniform flow. Though, the sudden reduction of the AD also appears slightly too steep compared to the results at higher resolution.

Additional investigations have been performed to understand the origin of the offset. The interpolation of the velocities on the blade was tested with the uniform kernel, the instantaneous velocity field was inspected and the tip-loss correction was verified to only have a impact in the tip region. None of those investigations have highlighted any major cause for the presence of this offset.

3.4.2.2 Unsteady loads

The deformation of the blades (not yet accounted in the present model) and the inherent fatigue loads are driven by the bending moments exerted by the flow. The moments are computed in the two polar directions of the rotor. The moment acting in the axial direction is called the flapwise moment M_f and the one acting in the tangential direction is called the edgewise moment M_e. Their respective definitions are

$$M_f = \int_{R_{hub}}^{R_{tip}} (r - R_{hub}) \mathbf{F} \cdot \hat{\mathbf{e}}_x dr \quad \text{and} \quad M_e = \int_{R_{hub}}^{R_{tip}} r \mathbf{F} \cdot \hat{\mathbf{e}}_\theta dr, \tag{3.4}$$

where $\mathbf{F}(r,t)$ is the time-varying force distribution per blade element length. An advantage of the AL against the AD is that obtaining the moments on one blade is straightforward, as the forces are directly computed on the rotating blades. For the AD, the distribution of the

forces on the disk surface requires to proceed to an additional step to recover the moments. Provided the forces were stored during the entire computation, one can run a virtual line within the disk and interpolate the forces at its position. The moments are then obtained by using the trapezoidal quadrature for the integral. Their time evolution as well as their probability density function (PDF) are plotted on figures 3.16 (for the coarse case) and 3.17 (for the fine case).

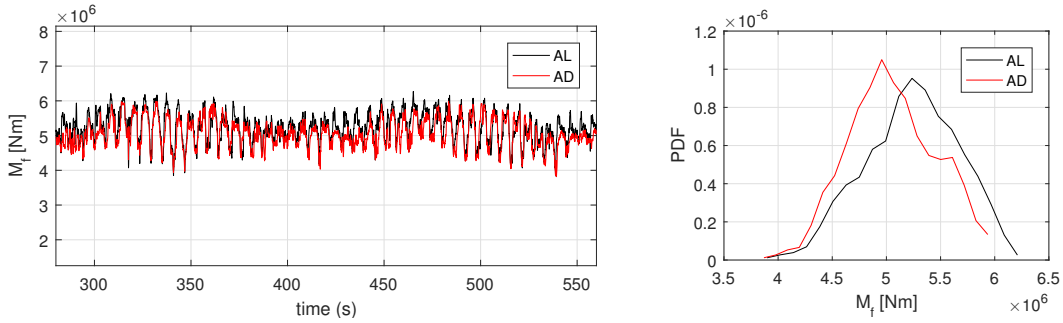

(a) Flapwise moment, 32 pts/D

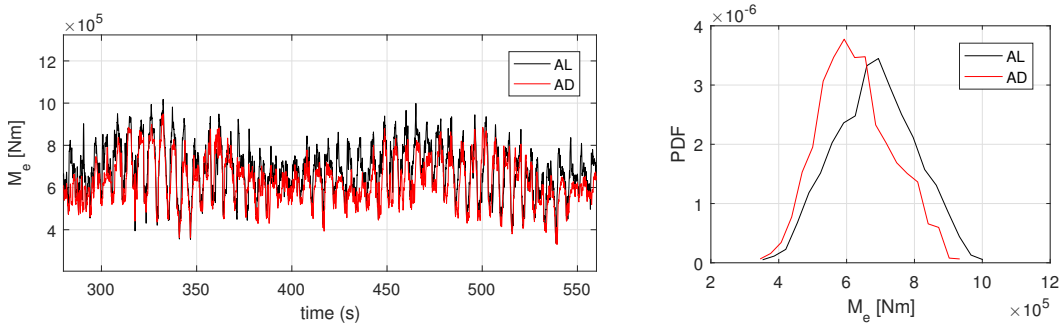

(b) Edgewise moment, 32 pts/D

Figure 3.16: *Comparison of the moments extracted with the AL (black) and AD (red) at low resolution. The left plot shows the time evolution, the right one shows the probability density function for both cases.*

The time evolution of both the edgewise and the flapwise moments is very similar for the two methods. Three scales of time variations are distinguishable. Some small oscillations with high frequencies are representative of the small eddies impacting the blades. The more regular but intense variations of the moment correspond to the blade rotation, whose effect is captured with consistency by the AL method without requiring any additional post-processing step. Finally, large-scale variations are also observed and correspond to larger gusts in the ABL.

The probability density function of both moments presents a small offset in the coarse case. It probably results from the differences that were previously observed for the normal and tangential force. This offset is decreased at finer resolution and this enhancement can be related to three positive aspects. First, as observed previously, the AL method captures the tip behaviour better. Secondly, the precision of the integral of the forces along the blade is quadrupled as the number of blade element was doubled and that the used quadrature is second order. Also, post-processing the AD requires to interpolate the forces between two

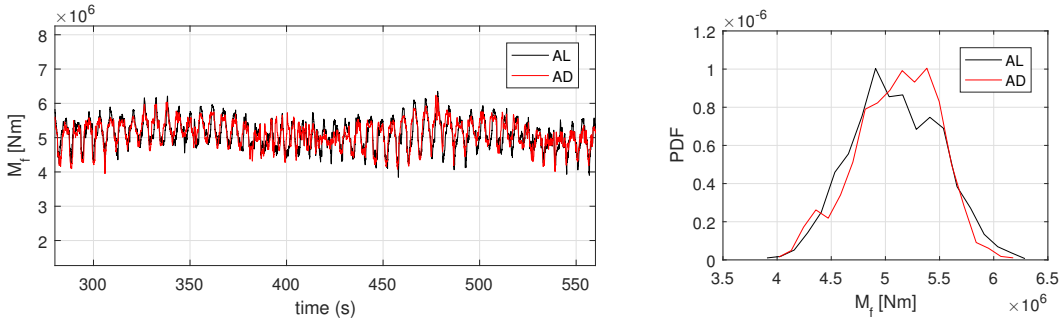

(a) Flapwise moment, 64 pts/D

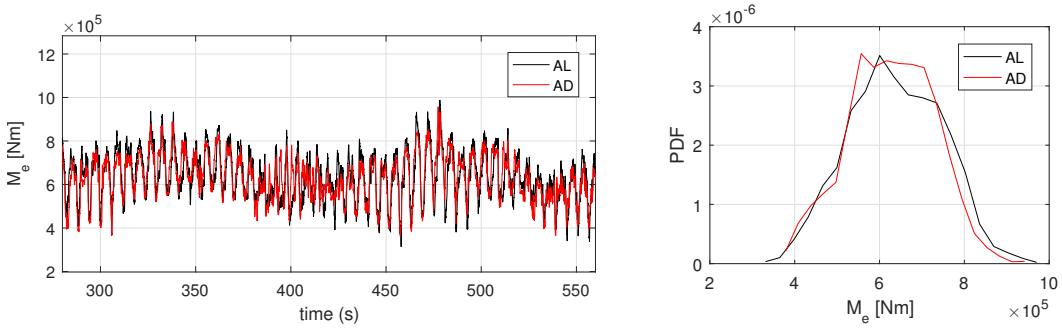

(b) Edgewise moment, 64 pts/D

Figure 3.17: *Comparison of the moments extracted with the AL (black) and AD (red) at high resolution. The left plot shows the time evolution, the right one shows the probability density function for both cases.*

sectors of the disk, which is performed better at high resolution due to the increased number of azimuthal elements. Finally, it is observed that, regardless of the small offset, the standard deviation is also 7% larger when computed with the AL method. This variation is due to the moment peaks that have a larger amplitude when computed with the AL method.

3.4.2.3 Power and thrust

The time-averaged power and thrust are summarized in Table 3.7. It quantifies the offset that was observed previously at around 6.5% for the power and 2.8% for the thrust.

	AL, 32pts/D	AD, 32 pts/D	AL, 64pts/D	AD, 64 pts/D
Power [kW]	2821 (+6.6%)	2636	2559 (+6.4%)	2396
Thrust [kN]	492 (+2.8%)	478	461.9 (+1.9%)	453

Table 3.7: *Time-averaged power and thrust*

The observed offset in power has two important aspects. Firstly, its origin is quite different than what was observed in the case of uniform flow. In this case, the dissimilarity of the power was mostly linked to the inability of the non-corrected AL method to capture the tip-losses sufficiently. Here, the power is increased due to the higher forces on the entire blade. Secondly, the variation of the power is almost not attenuated when the resolution is raised, and the grid

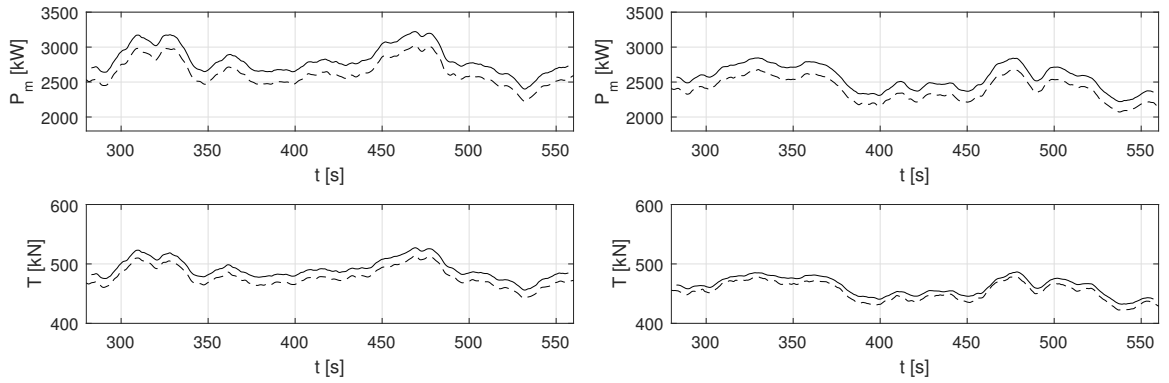

(a) Coarse resolution *(b) Fine resolution*

Figure 3.18: *Temporal evolution of the power and the thrust for AL (solid) and AD (dashed).*

resolution is thus not the cause of this offset.

The power and thrust extracted from the different simulations is displayed on figure 3.18. The AL power signal was filtered using a gaussian smoother of width equivalent to two seconds, in order to remove the oscillations resulting from the rotation of the blades. As observed for the moments and the time-averaged loads, a small offset is visible and the AL method predicts an increased power, regardless of the resolution. The offset is also constant in time. However, the recovered patterns are quite similar, and both methods capture the unsteady variations in a similar way.

The discrepancies between the AL and AD thrust histories are quite smaller than those observed in terms of power, but still slightly differ. This difference is due to the smaller variations observed in the normal force, that were mostly located in the outer part of the blade. The thrust also varies more with the resolution than the power. This is attributed to the better agreement of the normal forces, that makes the tip behaviour more determining. This variation could impact the predicted deviation of the wake when the turbines are tilted, as the misalignment between the thrust and the inflow is at the origin of this wake deflection process.

3.4.2.4 Wake behaviour

The instantaneous vorticity and streamwise velocity behind a wind turbine are displayed on figures 3.19, 3.22 and 3.20. Concerning the vorticity field, it appears that all four simulations give similar results in the far wake. The transition of the wake to its turbulent state is also predicted similarly by all cases, with the destabilization happening around one diameter behind the rotor and the shear layers presenting a similar pattern. At a coarse resolution, the near wake is very similar for the two methods. Both AD and AL capture the streamtube expansion, and a continuous vortex sheet is shed from the blade tips. At a higher resolution, the near wake differs more importantly as the AL shed distinct vortex tubes whereas the AD still produces a continuous shear layer. However, this difference does not have an impact on the destabilization of the wake. The interaction with the surrounding turbulence therefore appears to be the dominant factor for the transition of the wake to a turbulent state

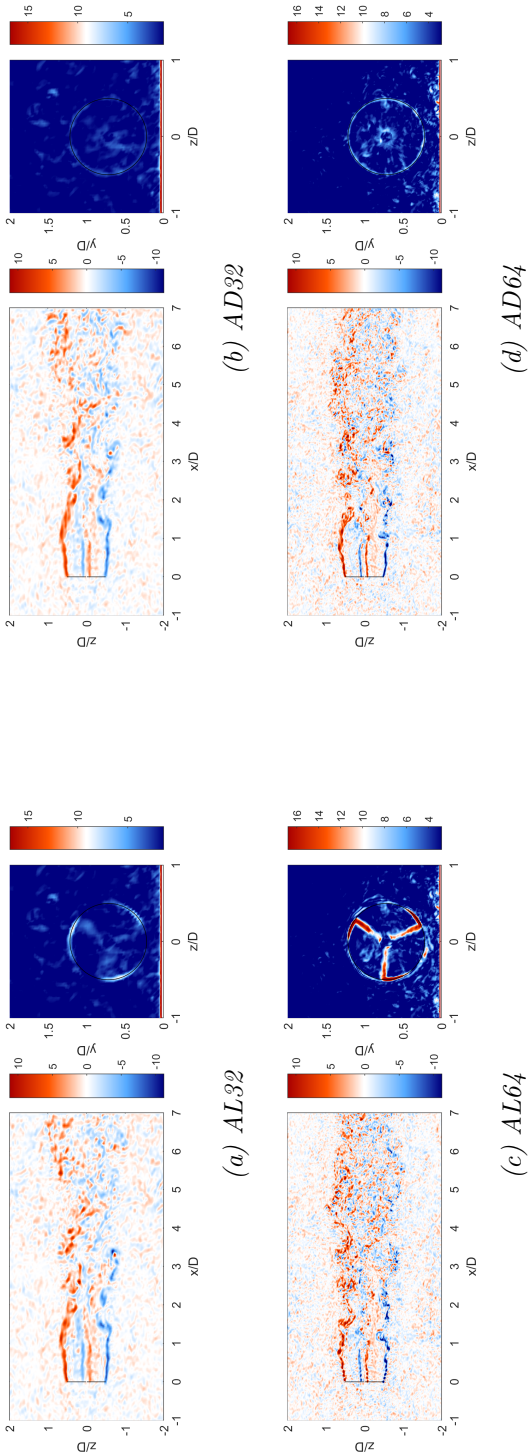

(a) AL32 (b) AD32 (c) AL64 (d) AD64

Figure 3.19: *Instantaneous normalized vorticity in the horizontal and the rotor plane*

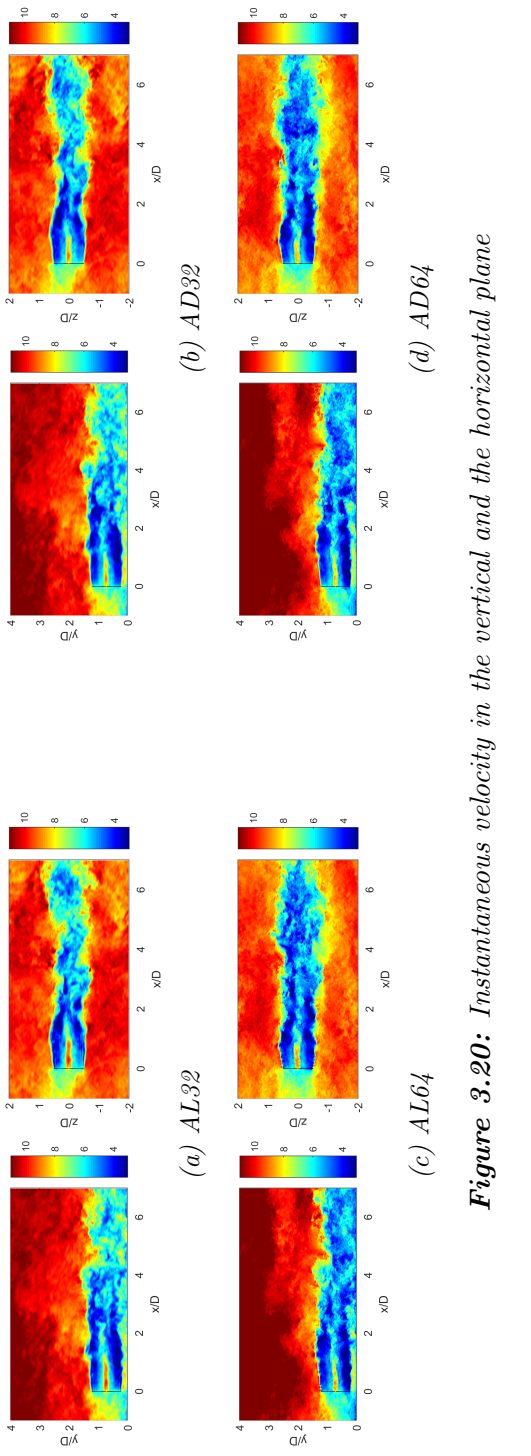

(a) AL32 (b) AD32 (c) AL64 (d) AD64

Figure 3.20: *Instantaneous velocity in the vertical and the horizontal plane*

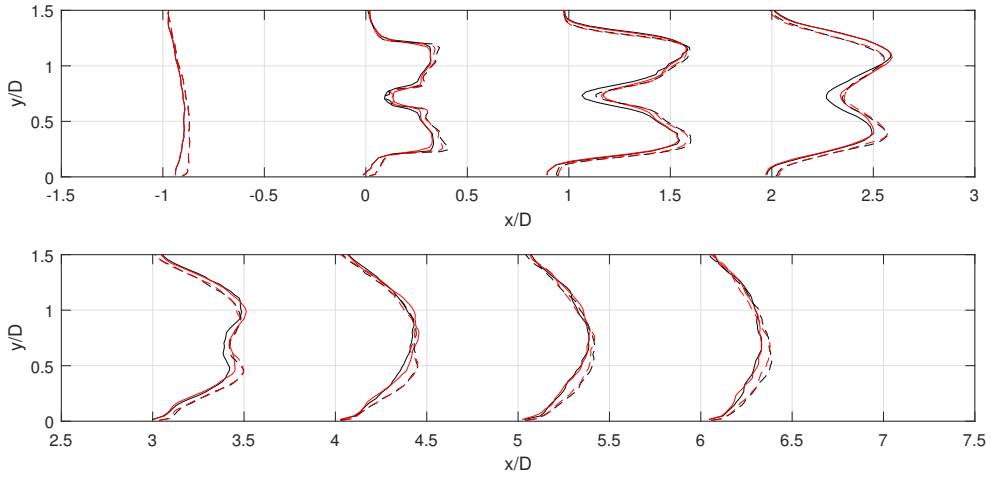

Figure 3.21: *Mean velocity deficit* $\frac{\bar{u}_{ABL} - \bar{u}}{u_\infty}$ *in the vertical plane containing the rotor axis. AL (black) and AD (red), for coarse (solid) and fine (dashed) resolution.*

The velocity field behaviour is comparable to the vorticity. The highly resolved AL is the only method that renders oscillations at small distance downstream of the rotor. All methods show very good agreement in the far wake. Large wake oscillations are not observed, what is probably due to the small level of ambiant turbulence intensity. This is also probably reinforced by the small size of the domain in the spanwise direction that constrains the horizontal wake movement.

The time-averaged velocity deficit at several downstream locations is depicted on figure 3.21. It is normalized regarding the time-averaged velocity at the hub $u_\infty = 9m/s$. In the near wake, the deficit generated by the coarse AL is larger at the hub, probably due to the absence of force mollification in this region. In the far wake, the highly resolved methods tend to predict an higher deficit, but it is unclear if this is due to the grid resolution or to the variation in the turbulent inflow generated separately for the two simulations. In spite of those observations, both methods predict quite similar results for the mean velocity deficit, especially when they are used at the same resolution. Finally, one observes that the time-averaged deficit one diameter before the turbine is larger at fine resolution, which could explain by the lower time-averaged forces.

3.5 Conclusion

In this chapter, the AL method was improved by modifying the distribution of the forces on the surrounding mesh. This distribution allows to smooth the forces in a way that mimics the pressure field around the blades, and hence increases the fidelity of the method. Modifying the mollification of the forces also required to modify the interpolation of the velocities from the surrounding mesh, so that the interpolation kernel has a similar topology to the smoothing one. This was performed by defining a new interpolation function with a wide support based on B-Splines.

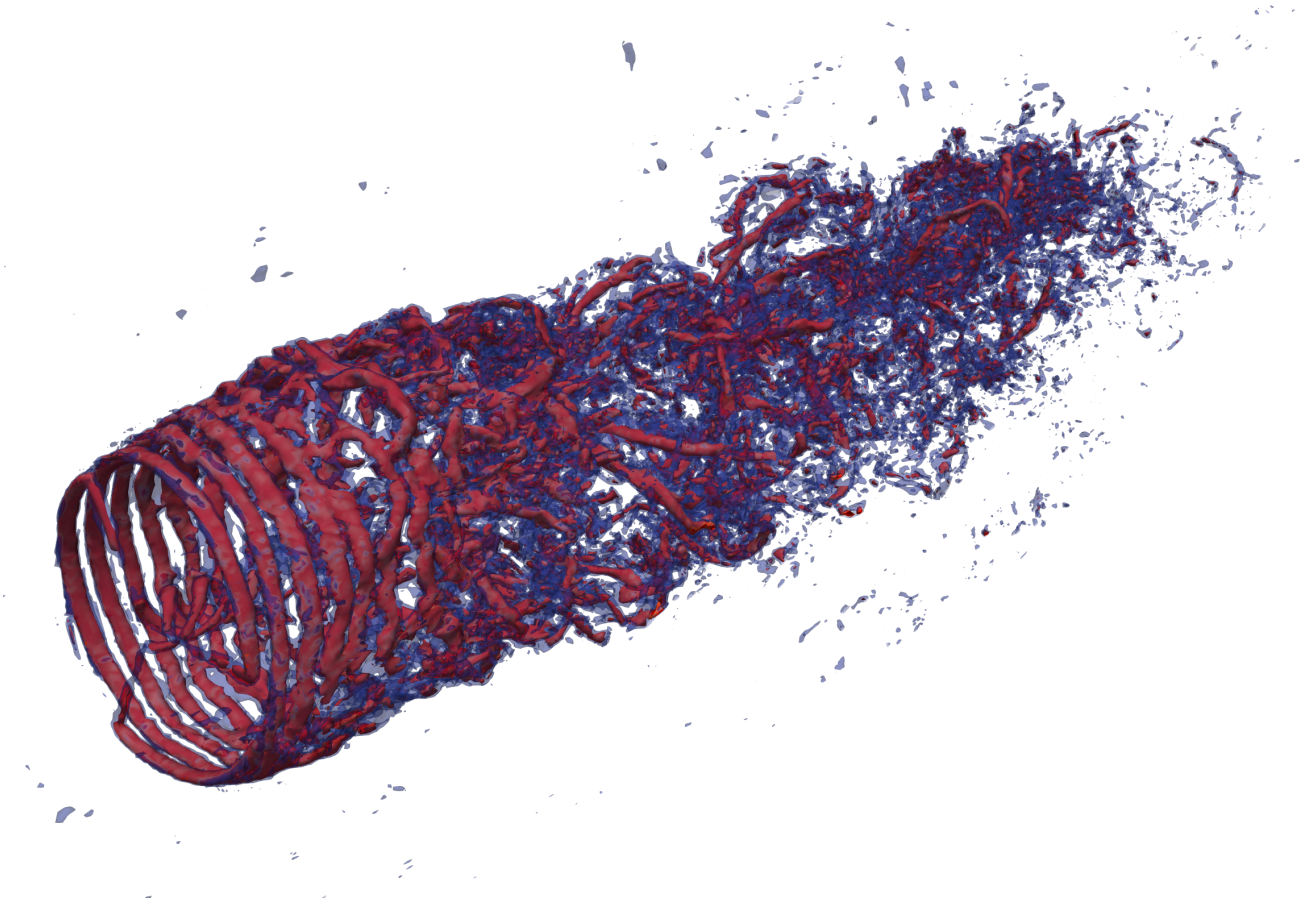

Figure 3.22: *Isocontour of vorticity behind a wind turbine in an atmosperic boundary layer, computed with 64 points per diameters.*

The improved AL method was compared to the advanced AD method in uniform flows. At first, various topologies of the smoothing kernel were assessed and the spanwise mollification was pointed out as the source of the load overestimation often noticed on the blade tips. It was hence concluded that the 2D mollification gives the best results in terms of loads and power. Further investigations on this kernel were then carried. The optimal values of its geometry were found at coarse resolution to be $\sigma_c/\Delta z = 3$ and $\sigma_t/\Delta z = 1$. This helped recovering a force distribution on the blade that is consistent with the AD. The sensitivity to the grid was also studied and it appeared that coarsening the resolution reduces the ability of the AL to predict the tip behaviour.

The AL method was then verified by comparing the rotor characteristics at various operating points of the wind turbine. Interestingly, the behaviour of the AL method is enhanced when the upstream velocity differs from 9m/s. The interpolation also showed a determining role in capturing the proper induction at the blade in those cases.

Finally, the AL and AD methods were compared in an ABL at high and low resolution. Both methods exhibited good agreement at each resolution, and their ability to model the wake correctly was highlighted, even for the coarse case. A small offset in the time-averaged thrust, power and load was observed, but it stayed quite limited. Also, this offset was found

to be consistent with the time and the resolution. Thus, as all simulations performed with the AL method would present this offset, their relative comparison remains valid.

Through the rest of this work, the AL method mollified with a 2D interpolation kernel will be used for the simulation of tilted wind turbines as it allows to remove the assumptions on the upstream velocity underlying the tip-loss correction. If this sampling showed good agreement in straight cases, yawing or tilting rotors creates an ambiguity about how it should be performed. This is especially the case in an ABL presenting an asymmetric inflow in the vertical direction. The correction having an effect on the thrust, itself playing an important role in the wake deviation, dropping the assumptions on the tip-losses increases the robustness of our future analysis of tilted machines.

The AL method however presents the disadvantage of being more constrained numerically than the AD. The resolution plays an important role in capturing the correct forces and power, and cannot be reduced further than 32 points per diameter. The time-step is also limited by the value of the allowable tip-CFL.

In particular, the simulation of a wind turbine in an ABL computed with 32 points per diameters confirmed the reliability of the model. The forces, power and thrust were recovered appropriately. Also, the wake structures were also correctly recovered, so that the interaction between two wind turbines can be effectively modeled using the AL method. This resolution will thus be used for the further investigations, as it constitutes a good trade off between the computational cost and the accuracy of the results.

Chapter 4

Tilted wind turbine in an atmospheric boundary layer

This chapter aims at assessing the effect of tilting wind turbines by studying a single machine in realistic conditions of operation. The numerical set up of the simulations is first described. Then, we study various tilt angles and their effects on the turbine and the flow. In particular, the variation of power and thrust as well as the potential increase of fatigue damage are quantified for the rotor. The impact on the flow is evaluated by measuring the wake statistics, such as the average velocity deficit and the turbulent kinetic energy production and the wake recovery. This chapter will also introduce the techniques used to quantify the wake recovery and deflection, that will be used in the later analysis of wind farms.

4.1 Numerical set up

The presented simulations have a configuration similar to the coarse one presented in appendix A. The wind turbine is impacted by an atmospheric boundary layer (ABL) computed with a precursor and the hub average velocity is 9m/s. The rotation speed of 10.3 rpm is kept constant as the controller is disabled to avoid any variation of the parameters between the assessed cases. The wind turbine itself is modeled with the actuator lines (AL) method described in the previous chapter. The velocities are interpolated using a uniform kernel and the forces are distributed with the non-isotropic 2D Gaussian kernel. The timestep is chosen as $\Delta t = 0.04s$ so that the tip-CFL is sufficiently small. The total simulation time is 560 seconds which corresponds to four convective times, but only the two last ones are used to compute the statistics.

Three tilt angles γ are assessed: 25^o, 0^o and -25^o. Those values are chosen as they are sufficiently large for the effects of tilting to be clearly distinguishable. A positive tilt angle is achieved in practice by using a downwind configuration for which 25^o is a realistic angle of inclination [35]. In this work, the influence of the tower was neglected. The 25^o case is referred to as the positive-tilt case, in opposition to the negative-tilt case and the no-tilt case.

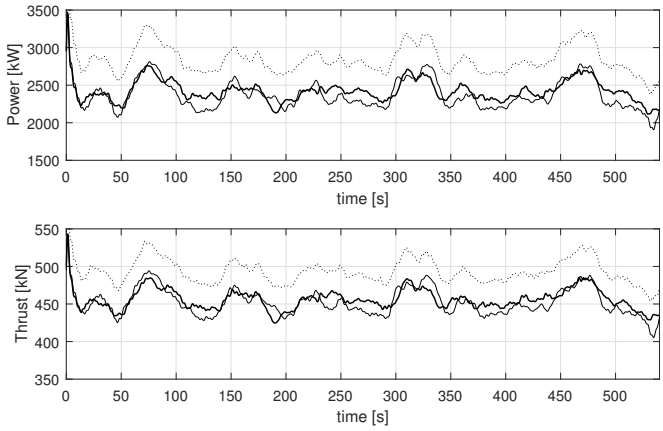

Figure 4.1: *Time evolution of the filtered power and thrust for a single wind turbine in ABL at three different tilt angle: 0^o (dotted), 25^o (thick solid) and -25^o (thin solid).*

4.2 Power and thrust

The power and thrust extracted by the blades at different tilt angles is summarized in Table 4.1. Tilting a single wind turbine leads to an important power loss due to the reduction of the surface normal to the wind and the misalignment of the blades with the inflow. Interestingly, the power of a positive-tilt case is 2% higher than that of a negative one. This is related to the fact that the upwind part of the rotor is the upper part in the 25^o case. This upwind part is less impacted by the wake and undergoes a lower axial induction. This more effective part of the rotor catches a faster velocity in the positive-tilt case, leading to an increased power and thrust. Furthermore, the standard deviation of the signal is decreased in connection with the increase of the tilt angle. On the sampled data, the positive-tilt case is thus less sensible to the variations of the turbulent flow behaviour.

Angle	Power [kW]	Variation	STD	Thrust [kN]	Variation	STD
0^o	2821.4	-	8.2%	491.9	-	19.1 %
25^o	2414.3	-14.4%	7.1%	455.8	-7.3%	15.5 %
-25^o	2359.3	-16.4%	9.8%	450.6	-8.4%	20.7 %

Table 4.1: *Power and thrust statistics*

Figure 4.1 shows the time evolution of the power and thrust filtered with a cut-off frequency of 0.3 Hz to remove the contributions smaller than the rotation frequency. We observe that the three samples present similarities in their variations. The correlation coefficient of the positive- and negative-tilt signals compared to the no-tilt case are 0.90 and 0.88, respectively, while it drops to 0.75 between the -25^o and the 25^o cases. The turbulent variations of the inflow thus affects the power output differently between the various tilt angles. In general, the positive-tilt case produces more power than the negative one. However, this tendency is not verified at each time step. The time evolution of the thrust presents a similar behaviour to the power signal.

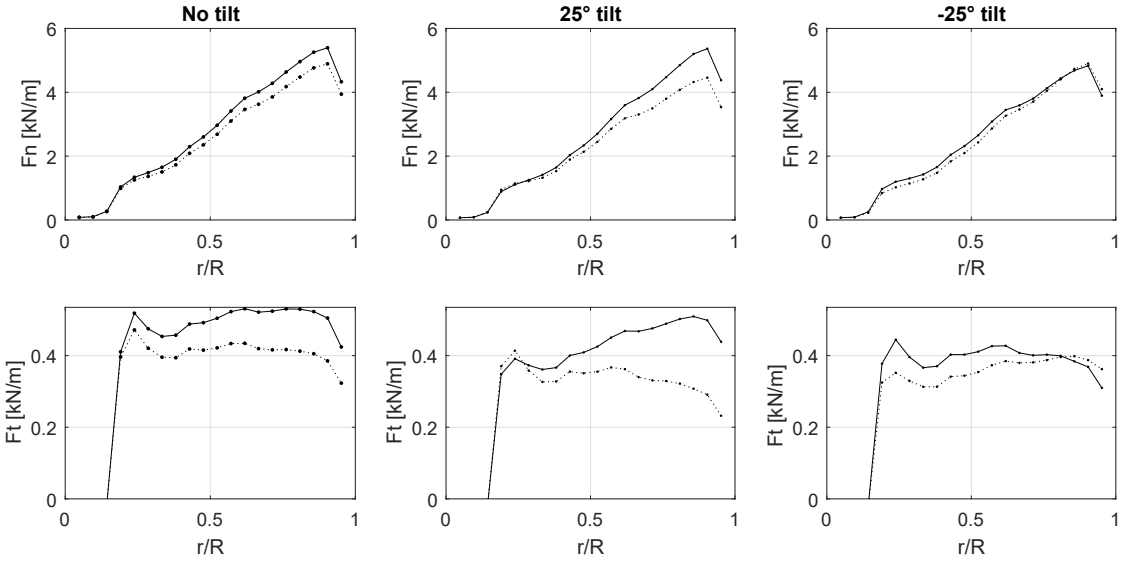

Figure 4.2: *Mean normal and tangential forces acting on the upper (solid) and lower (dotted) half of the rotor.*

4.3 Loads and fatigue analysis

In section 3.4, it was observed that the nature of the ABL inflow created an azimuthal dependency on the forces and thus modified the different moments. When tilting is added, this asymmetry is further modified, leading to the alleviation or intensification of the alternating loads. Those effects must be quantified to compare the differential impact of tilting on the structure and blades loads.

Figure 4.2 displays the time-averaged forces acting on the upper and lower regions of the rotor. In the no-tilt case, the upper part is impacted by larger velocities due to the sheared inflow, and thus experiences an increased loading. This imbalance is especially visible on the second half of the blade. When tilted positively, the upper part is shifted upwind and the loads are further increased. The difference between the mean forces on the blades is multiplied by a factor 1.30 compared to the no-tilt case. Conversely, the difference is alleviated if the turbine is negatively tilted, as the upper part is placed downwind. The mean force imbalance is reduced by a factor 0.37.

The noticeable force variation is especially located at the tip and this imbalance impacts the tilting moment M_t acting on the nacelle and defined by

$$M_t(t) = \sum_{\text{blades}} \hat{\mathbf{e}}_z \cdot \int_0^R \mathbf{y} \times \mathbf{F}(r,t) dr,$$

where F is the force per blade element length and $\mathbf{y}$ the distance to the tilting axis. The value of the tilting moment for each considered case is found in Table 4.2. The increase is very important for the positive case and the design of the nacelle will have to take this moment into account. On the contrary, tilting the rotor negatively leads to a drastic decrease of the

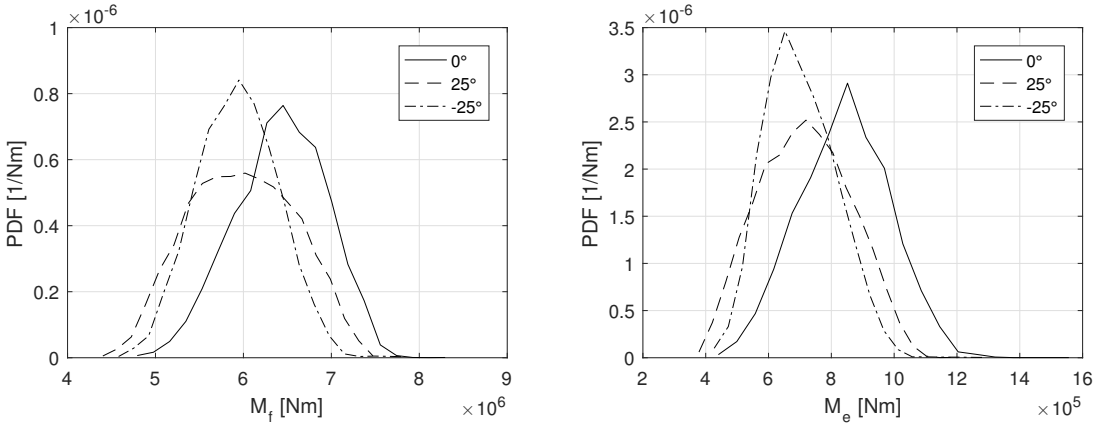

(a) Flapwise moment *(b) Edgewise moment*

Figure 4.3: *Probability density function over time of the bending moments.*

tilting moment.

	0	25	-25
Tilting moment [kNm]	-727.2	-1044.1	-166.7
Variation [%]	-	+43.6 %	-77.1 %
Standard deviation [%]	0.8 %	0.5 %	3.2 %

Table 4.2: *tilting moment and its variation compared to the reference case*

Figure 4.3 depicts the probability density function of the two bending moments acting on the blades, defined by equation (3.4). Both tilted rotors experience a lower mean bending moment than the no-tilt case. This originates from the reduction of the aerodynamic forces caused by the misalignment with the free-flow. Also, a small offset is observed between the means of the edgewise moment of the positively and negatively tilted rotor. This variation can be linked to the offset observed for the power and thrust. The standard deviation of the positive-tilt is larger than that of the negative case. This variation is related to the imbalance between the two halves of the rotor that was observed for both the normal and the tangential forces. The variation is larger for the positive-tilt case and is linked to an increased alternation of the bending moment during one rotation. This case thus suffers from larger alternating loads and thus have an increased risk of failure caused by fatigue.

To confirm this trend, a more accurate fatigue analysis is performed. The loads are sampled on the two lasts convective times and the number of cycles of each amplitude is extracted using the rainflow counting algorithm introduced in Matsuishi [36]. The results are depicted on figure 4.4 where the binning was performed for the large amplitude cycles. A clear shift towards higher alternating loads is observed when the tilt angle is increased, especially for the flapwise moment. Also, the total number of high alternating load cycles is of the order of the number of rotation in the sampled time. The vertical shear along the rotor is thus the main source of high fatigue loads and the shift finds its origin in the force variation observed on figure 4.2.

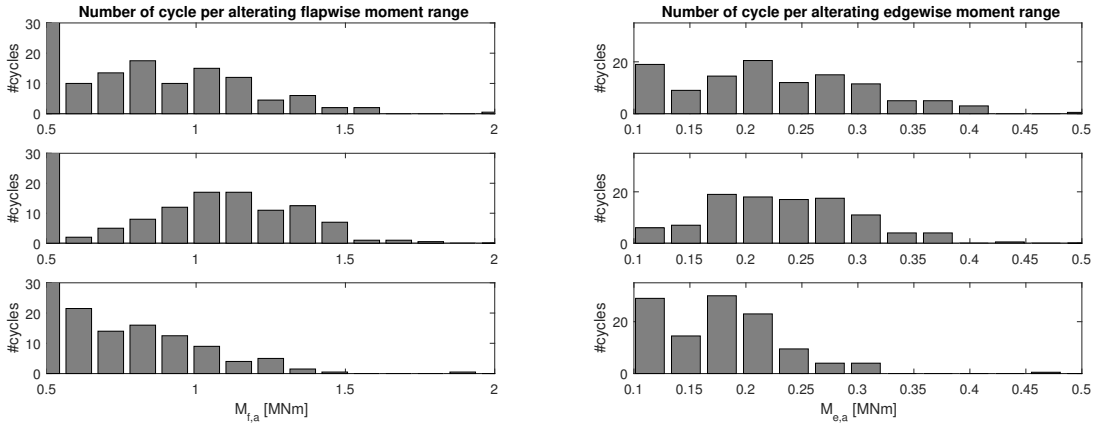

Figure 4.4: *Bar plot of the number of cycle per bending moment range. Tilt angle from up to down:* 0^o*,* 25^o *and* -25^o

The total effect of the alternating loads in the sampled time is quantified by computing the equivalent alternating moment $M_{a,eq}$. It is defined as the purely alternating moment that would generate the same damage as the unsteady signal observed in reality and takes into account the entire spectrum of alternating loads. It can be calculated from the data recovered with rainflow counting and the equation

$$M_{a,eq} = \left(\sum_{i=0}^{n_c} \frac{n_i M_i^{-m}}{N_{eq}} \right)^{1/m},$$

where n_i is the number of cycles with an alternating moment M_i, n_c is the number of cycles and N_{eq} is a predefined number of cycles [37]. The parameter m is the slope of the M-N curve. It is set to 10 for the glass-fiber composing the rotor blades [38, 32]. The number of equivalent cycles N_{eq} is chosen so that the frequency of the equivalent alternating moment is one Hertz. The total process to retrieve the equivalent moment required some additional assumptions that are summarized in annex B.

	No tilt	25^o tilt	-25^o tilt
Equivalent flapwise moment [kNm]	1080	1160 (+7.4%)	901 (-16.8%)
Equivalent edgewise moment [kNm]	2970	2720 (-8.6%)	2210 (-25.5%)

Table 4.3: *Equivalent alternating moment for the tilted cases compared to the straight case.*

Table 4.3 contains the equivalent alternating moments generated solely by the aerodynamic forces for the considered cases. The equivalent flapwise bending moment is increased for the 25^o case and decreased for the -25^o case, as expected from the observation of the high amplitude varying cycles on figure 4.4. However, the amplification in the positive-tilt stays reasonable due to the decrease of the amplitude of the high frequency cycles due to the misalignment. For the edgewise moment, a reduction is observed in both cases with a different amplitude, the -25^o case benefiting from a larger mitigation.

In conclusion, a negative tilt angle succeeds to alleviate the aerodynamic loads acting on the turbine. The reduction of the vertical shear impacting the rotor has a positive impact

on the mean tilting moment and on the fatigue loads. On the contrary, a positive tilt leads to an increase of those two stresses. However, this amplification stays quite limited for the fatigue loading which is the most restrictive one. Hence, the feasibility of the positive-tilt configuration is not compromised.

4.4 Wake behaviour

4.4.1 Instantaneous streamwise velocity

Figure 4.5 depicts the instantaneous velocity field at the end of the simulation (t=560s). On the y-plane, it is observed that both tilted turbines have high velocity regions in their far wake, contrary to the no-tilt case. The wake of the positive-tilt case also appears to be more spread in the spanwise direction. This is linked to the ground effect that will increase the dispersion of the velocity deficit (see later on figure 4.9). On the z-plane, one can observe the deviation of the low velocities, but this behaviour will be clearer on the time-averaged velocities. The negative-tilt case presents more mixing and some high velocities regions are found at low altitude. Their origin comes from the acceleration of the flow at the bottom of the rotor. The 25^o case does not present such an increase at the bottom, and the far wake is more sheared than for the other cases.

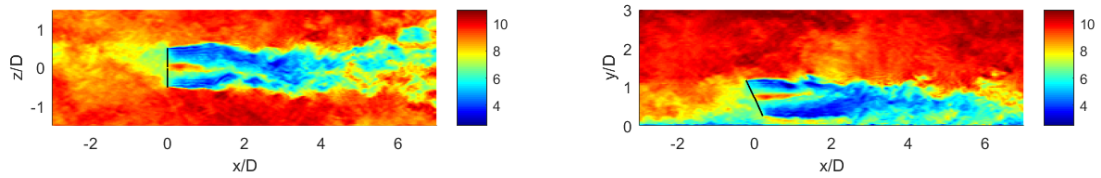

(a) 25^o *tilt*

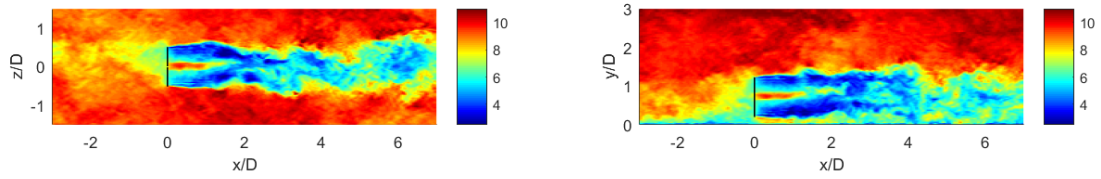

(b) no tilt

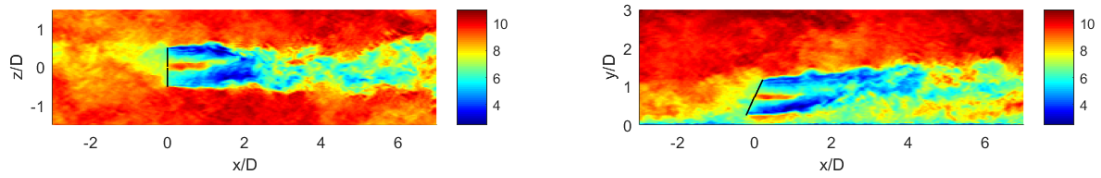

(c) -25^o *tilt*

Figure 4.5: *Instantaneous streamwise velocity in the y- and z-plane intersecting the rotor hub. Tilt angle from up to down:* 25^o, 0^o *and* -25^o.

4.4.2 Flow statistics

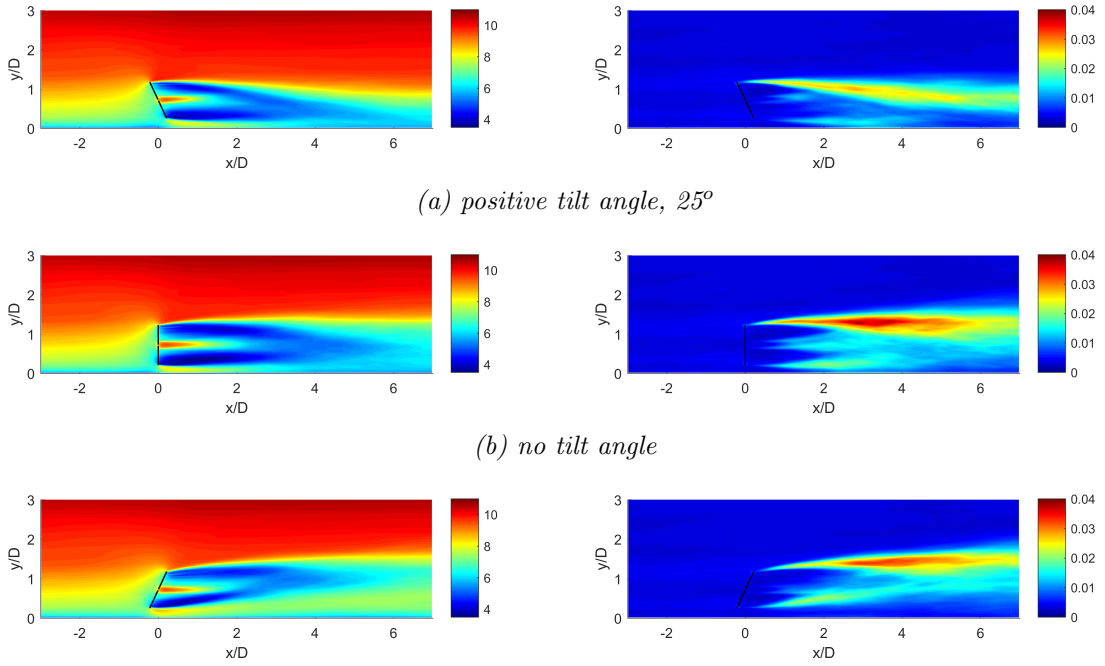

(a) positive tilt angle, 25º

(b) no tilt angle

(c) negative tilt angle, -25º

Figure 4.6: *Isocontours of mean velocity and mean normalized turbulent kinetic energy (with the factor U_∞^2).*

Figure 4.6 represents the time-averaged streamwise velocity and the turbulent kinetic energy production in the wake. Both depicted quantities are deflected downwards for the positive-tilt case and upwards for the negative-tilt case. Also, there is less production of turbulent kinetic energy for the tilted wind turbines, especially for the positive case. This is attributed to the reduction of the shear between the wake and the upper part of the ABL. The reduction of the turbulent fluctuations decreases the mixing with the free-flow and the low velocities region can be observed further in the wake of the positive-tilt case. The analysis of the time-averaged streamwise velocity also indicates that the 25^o case has more potential in improving the wind farm efficiency. In fact, the downwards wake deflection attracts higher velocities from the upper part of the free-stream. This could reduce the deep-array effect and increase the production of the downstream turbines. On the contrary, when the wake is deviated upwards, the region behind the rotor is filled with low velocities from the bottom of the shear layer. Although the streamwise velocity is higher behind the turbine of the negative-tilt case compared to the no-tilt case, the repetition of this effect in a wind farm is likely to hinder the energy capture and have a negative impact on the total efficiency.

The recovery of the wake can be characterized by two indicators [39]. The power P contained in the flow past the rotor is given by

$$P(x) = \left\langle \frac{\bar{u}^3(x)}{U_\infty^3} \right\rangle.$$

The wake recovery rate RR is defined as the variation of the time-averaged streamwise velocity along the x-direction,

$$RR(x) = \Big\langle \frac{\partial \bar{u}(x)}{\partial x} \frac{D}{U_\infty} \Big\rangle.$$

The operator $\langle \cdot \rangle$ denotes the spatial average. This averaging is performed on a disk with the same dimension as the rotor and centered at the hub position. The disk is swept along the x-axis direction so that the evolution is evaluated behind the rotor. Here, the equivalent upstream velocity U_∞ is chosen so that the normalized power of the inflow is unity. This leads to a value of 9.33 m/s for all three simulations.

Figure 4.7 depicts the evolution of the power and the wake recovery rate. The power starts its decrease upstream from the wind turbine and reaches a minimum slightly downstream. The tilted turbines attain their smallest value earlier, which means that the recovery starts beforehand. Moreover, the minimal value is linked to the thrust, which explains why it lies lower for the straight turbine and (to a smaller extend) for the positive-tilt case. After $x/D = 1$, the power in the flow starts increasing again. This increase is quicker for the positive case that overtakes the negative one at around $x/D = 3$. At the end of the computational domain, the wake of the tilted rotors contains 70% (for the positive-tilt case) and 66% (for the negative-tilt case) of the initial power, against 51% for the no-tilt case. The wake recovery rate also indicates that the recovery starts earlier when the turbines are tilted, as a positive value is recovered more upstream. The recovery rate is higher for the 25^o case than the -25^o. Also, the decrease is steadier for the 25^o case than for the two others. Those differences are attributed to the ground effect, that is beneficial to the positive-tilt case, whereas the recovery of the two other cases is mostly driven by the turbulent mixing with the surrounding flow.

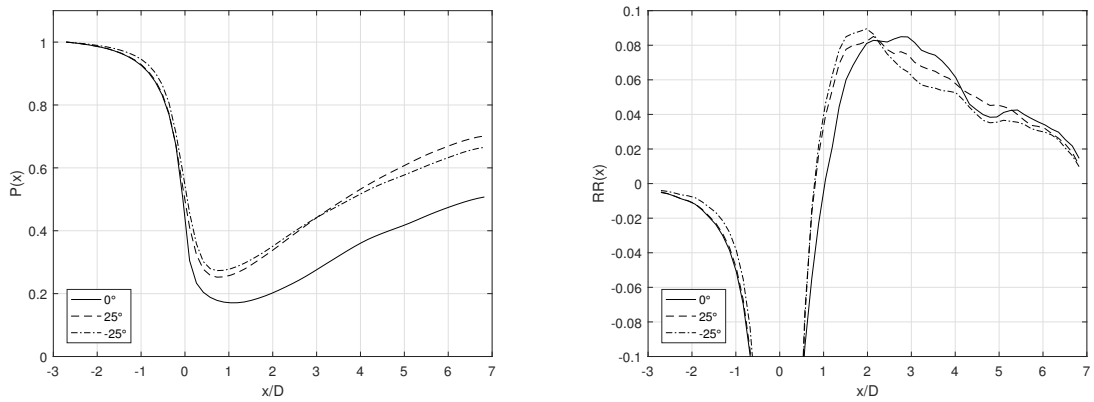

(a) Power available in the flow *(b) Wake recovery rate*

Figure 4.7: *Evolution of the power contained in the flow and of the wake recovery rate evaluated on a disk with the same dimension as the rotor swept along the x-axis.*

Figure 4.8 shows the wake center deviation in the vertical direction and the wake width in both vertical and spanwise directions. Those results were obtained by fitting (in the mean square sense) the average velocity deficit in the x-plane with a Gaussian-like function defined

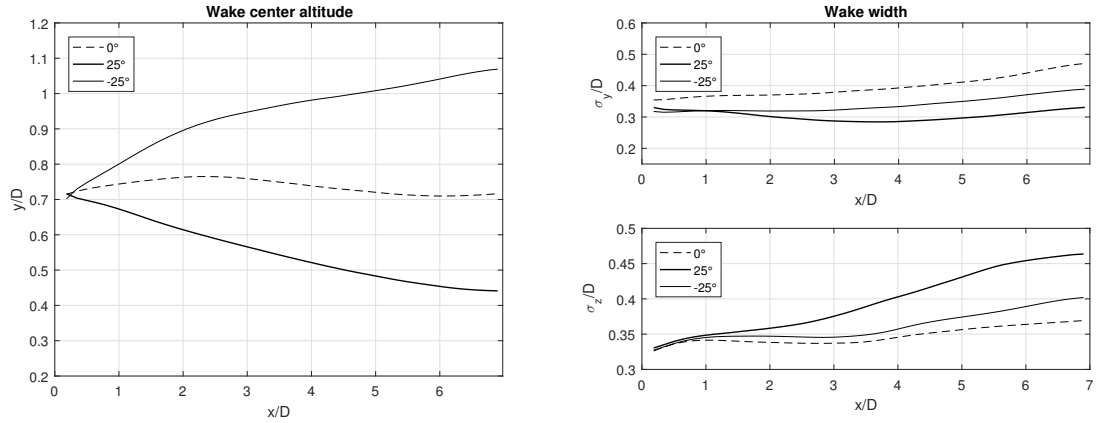

Figure 4.8: *Wake center altitude and standard deviation from this center, as a function of the distance to the rotor.*

by

$$u(y,z) \simeq A \exp\left[-\frac{1}{2(1-\rho^2)}\left(\frac{(y-\mu_y)^2}{\sigma_y^2} - \frac{2\rho(y-\mu_y)(z-\mu_z)}{\sigma_y\sigma_z} + \frac{(z-\mu_z)^2}{\sigma_z^2}\right)\right],$$

where A is the amplitude and ρ is the correlation coefficient [40]. The means μ_y and μ_z give the position of the center in their respective directions. The standard deviations σ_y and σ_z are an image of the wake width, considering that more than 95% of the deficit integral lies in the region contained between 2 standard deviations. This gaussian shape showed good agreement with velocity deficit, especially in the far wake [41].

The wake of the tilted turbines are deviated importantly with an initial slope of -0.05 and 0.1 for the 25^o and the -25^o case, respectively. Interestingly, the two angles are significantly different. This appears to be related to the ground effect that plays a larger role when the wake is deviated downwards. Also, the width of the wake in the vertical direction is smaller for the tilted turbines. At first, the ratio between the vertical width of the tilted turbines and the non-tilted one corresponds to the cosine of the tilt angle. Later, the downwards directed wake is shrunk due to the interaction with the ground. This effect is compensated by an increase of the width in the spanwise direction. The latter effect could increase the interactions between turbines placed in adjacent rows, but stays quite limited.

Figure 4.9 presents the mean streamwise velocity deficit and the mean vorticity superposed with streamlines of the mean transverse (cross) flow at several downstream locations. The vortex structure in the wake is substantially modified when the turbines are tilted. For the no-tilt case, only one vortex core is distinguishable behind the center of the rotor. It corresponds to the rotation of the flow induced by the turbine. The streamlines are then structured in a spiral centered on the vortex core. This rotation loses intensity as we move through the wake, due to its recovery. This structure of the transverse velocities does not impact the deficit position that stays at the same location behind the rotor, and simply diffuses as we propagate away.

When the turbine is tilted, two additional vortex cores appear. They consist in two opposite vortices centered around $z/D = \pm 0.5$. The presence of those two additional cores

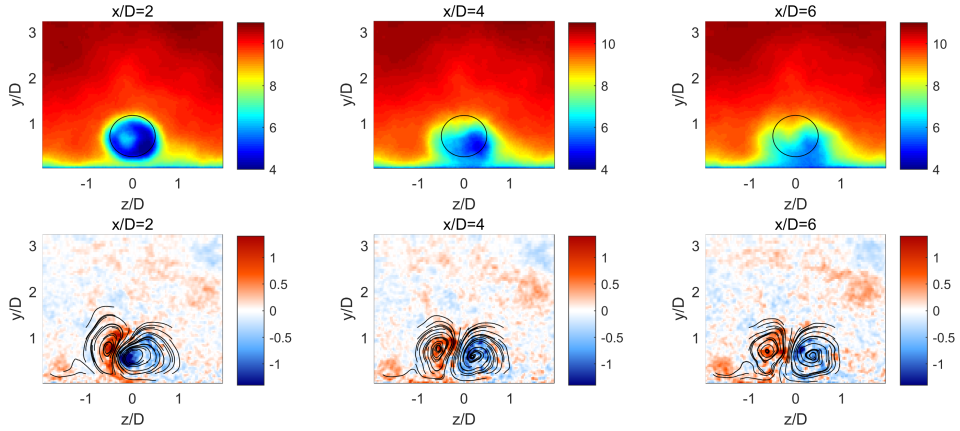

(a) 25^o tilt

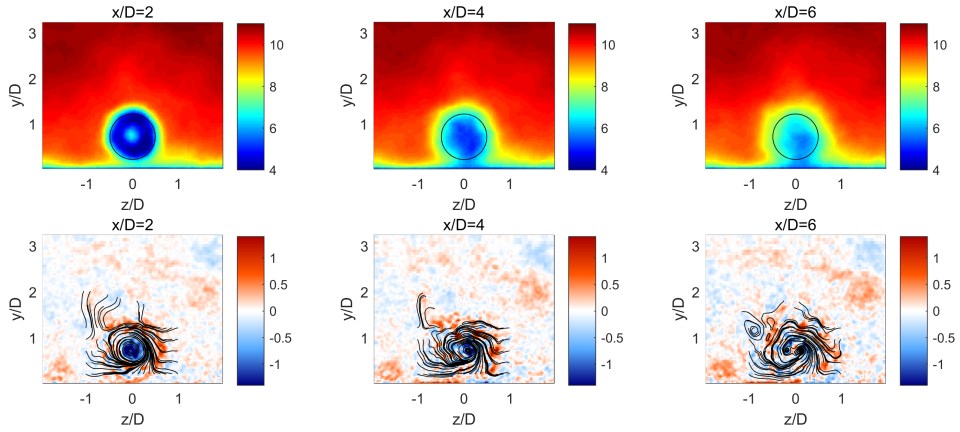

(b) no tilt

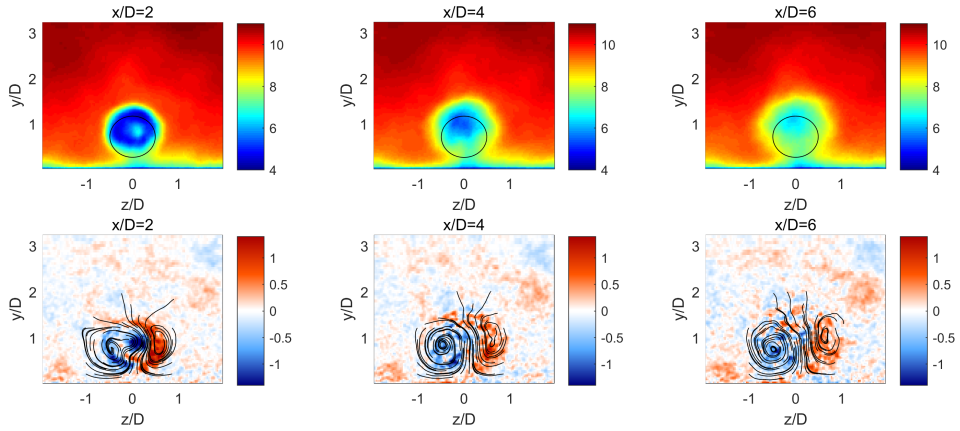

(c) −25^o tilt

Figure 4.9: *Time-averaged streamwise velocity and time-averaged normalized streamwise vorticity ($\bar{\omega}_x D/U_\infty$), superposed with streamlines of the transverse velocities. The positive vortices (in red) correspond to clockwise rotation.*

dramatically modifies the streamlines. Instead of a spiral, two contra-rotating structures are observed. This combination creates a downwards (25^o case) or upwards (-25^o case) velocity component behind the rotor. This is responsible for the observed deficit deviation. The deviation of the streamlines near the ground are also responsible of the variation of the wake shape observed in the positive-tilt case. However, those transverse velocities are not confined behind the rotor and also impact the sides of the turbine. For the positive-tilt case, some low velocity from the bottom of the shear layer could be lifted on the sides. This could have a harmful effect on the parallel rows or if the turbines are insufficiently aligned with the inflow direction.

The apparition of this pair of contra-rotating vortices is linked to the thrust T that has a component perpendicular to the streamwise velocity given by $T \sin \gamma$. This can be seen as a lift force that thus implies circulation in the flow. The rotor can be approximated as a horizontal lifting line with a distribution of the circulation Γ given by

$$\Gamma(z) = \frac{T \sin(\gamma)}{\rho U_\infty \pi R^2} c(z)$$

with $c(z)$ the chord distribution of the disk, as developed in Sophira *et al* [42]. Similarly to the lifting line approach, a vortex sheet is shed downstream and quickly roll-up around the stronger vortices originated from the sides of the rotor [43]. The thrust and the tilt angle are thus two important parameters in the wake deflection.

4.5 Conclusion

This chapter provided insight into the tilted wind turbines behaviour in a neutral atmospheric boundary layer. Three tilt angles were assessed to evaluate the effects of positive and negative tilting on some important aspects. The power and thrust were first assessed and it appeared that a single wind turbine loses around 15% of power when tilted by $\pm 25^o$. However, the positive-tilt case produced 2% more power. Then, the loads and fatigue study revealed that the mean bending moment was reduced for both tilted cases, but that the fluctuations were higher for the positive-tilt case. This resulted in an increased equivalent fatigue loading. Finally, an analysis of the wake showed that adding a tilt angle results in a wake deflection and an increase of the recovery rate of the velocity deficit. The wake recovery rate and the mean energy in the flow were also higher in the tilted cases. Finally, the transverse velocities were found to be structured into two contra-rotating vortices that are a the origin of the wake deflection.

The presented analysis led to exciting results concerning tilting of wind turbines. The negative-tilt case achieved to reduce the load, and the upward wake deflection increases the speed of the wake recovery. However, it is unlikely to have a beneficial influence on the power of the downstream turbines in a wind farm configuration. In fact, the deflection goes together with the ascension of low velocities from the bottom of the shear layer. On the contrary, for the positive-tilt case, the wake deflection tends to pull in some high velocities. The entrainment phenomenon was also observed in that case, what presents a real potential for reducing the deep-array effect. The reverse of the medal is the increase of the fatigue loads, but the amplification stays reasonable.

Having defined the effect of tilting on single wind turbines and described the main analysis tools, we will now move on to the discussion of the interactions in wind farms. Tilting a

turbine generates power losses that make the application to an isolated machine irrelevant. However, in large wind farms, those losses could be outweighed by the production increase of the downstream turbines. The next Chapter will present tilted wind turbines in an array configuration in order to quantify those interactions and further assess the use of tilting in wind farms.

Chapter 5

Tilted turbines in a wind farm

In this chapter, the analysis of a wind farm containing tilted wind turbines is performed. The efficiency of such a farm can be drastically reduced due to the interactions between the turbines, especially if they are aligned with the wind direction. The velocity deficit behind the upstream machines moves towards the downstream ones, leading to a dramatic reduction of the power output. This chapter analyses such an aligned configuration for a small wind farm and shows how tilting can be used to overcome this issue. In particular, a special focus is put on how the turbines interact with each other, and how the modifications observed for a single wind turbine in the previous chapter are diluted or amplified in an array configuration.

5.1 Numerical set-up

The domain consists in a computational box of size 40Dx8Dx8D depicted on figure 5.1, with a grid spacing similar to the coarse resolution presented in 3.4. There are thus 32 grid points per diameters in the y- and z-direction, with a grid stretching in the vertical direction starting above the rotors. The horizontal spacing are different and set to $\Delta x = 1.25\Delta y$. The total mesh hence consists in 1024x128x256 grid points. The boundary conditions are inflow/outflow in the x-direction and periodic in the z-direction. As to the vertical one, the velocity is imposed at the bottom using a wall model, and a no-through condition is set at the upper part. The wall model is set so that the recovered velocity at the hub altitude is 9m/s, and the turbulence intensity is close to 6%, similarly to the simulations performed at smaller scales previously.

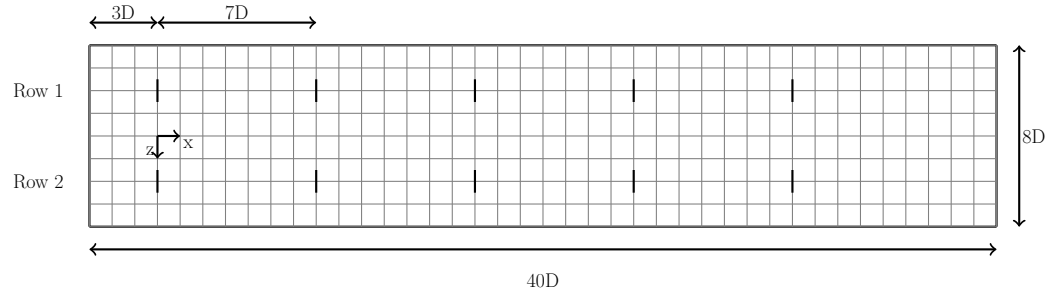

Figure 5.1: *Schematic of the computational domain and the location of the wind turbines*

The statistics of the recovered ABL are found in appendix A.

In this domain, ten turbines are placed with a spacing of 7D in the stream direction and 4D in the spanwise direction. The worst case for the wind turbine alignment is considered. The machines are thus perfectly aligned with the wind direction. As the boundary conditions are set to periodic in the spanwise direction, the simulation accounts virtually for an infinite number of rows. The turbines are modeled using the AL model. The force distribution is performed using a 2D gaussian kernel with $\sigma_c/\Delta z = 3$ and $\sigma_t/\Delta z = 1$ and the interpolation function is uniform. The wind turbines rotation speed is not constant through the simulation as they are controlled using a torque-based controller described in [30]. This allows a realistic response to the impacting flow. This controller is based on the second control-zone of the power curve, where the pitch angle of the blades is not modified.

The wind farm is simulated for a little bit more than 37 minutes with a time step of 0.04s, to ensure a sufficiently low tip-CFL. This represents 4 convective times based on the hub velocity. The statistics and time-averaged quantities described in the next sections are performed on the two last convective times.

In the following sections, the flow and the wind turbines behaviour in the wind farm will be discussed. Three cases are considered. The first wind farm is only composed of turbines with no tilt angle. For the two others, all the turbines were tilted with an angle of 15^o or 25^o. Those two angles were chosen as they are representative of two approaches. For the 15^o case, the power losses of a single wind turbines are sufficiently limited so that the tilt angle does not need to be modified if the turbines are not aligned. The 25^o angle is more representative of the maximal achievable angle if dynamic tilt control could be performed. The case with negative tilting is not considered as our previous investigations clearly showed that the resulting wake deflection was not favorable for the downstream machines. The three cases are denoted as the *baseline*, *intermediate* and *strong* cases for the angles of 0^o, 15^o and 25^o, respectively.

5.2 Power and thrust

The mean power and thrust of each wind turbine are depicted on figure 5.2. They are normalized regarding the power and thrust extracted from the first non-tilted machine of each row. As expected, the first tilted machines efficiency is reduced compared to the straight ones. This mean reduction is 16% in the strong case and 5% for the intermediate case. However, starting from the second turbine, the tilted cases produces more power than the baseline. The power extraction is reduced between the first and the second machine by 51% on average for the baseline case, but only 30% and 43% for the strong and intermediate tilted cases, respectively. Also, for the tilted cases, the power starts increasing from the third machine, as a consequence of the increase of the wake deflection. For the baseline case, the improvement is visible only from the fourth machine, likely due to the increase of the flow turbulence that helps accelerating the recovery. In the row 1, which benefits the most from the tilting effect, the power extracted from the last strongly tilted wind turbine is 73,4% of the first turbine of the baseline case. The intermediate case only recovers 59% of this power. As reference, the last turbine of the first row only produces 50,8% of the power of the first turbine in the baseline case. This increased efficiency is even more noticeable when the tilted nature of the turbines are taken into account. In that case, the power output difference of the last tilted

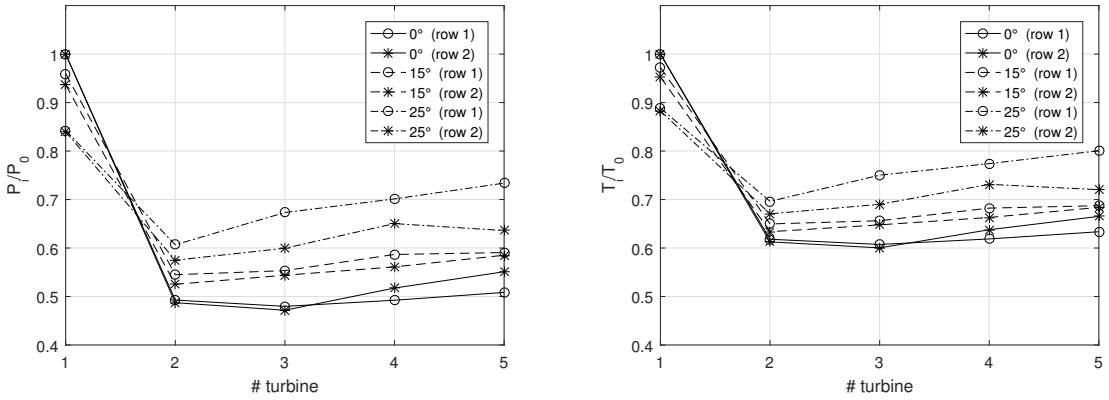

(a) Mean power *(b) Mean Thrust*

Figure 5.2: *Time-averaged power and thrust per turbine in the plant, normalized using the first straight turbine of each row*

turbine compared to the first one is 87.1% and 62.6% for the strong and intermediate tilted cases, respectively. The behaviour of the thrust is very similar to the power.

The time-averaged power output of the farm and of each row is presented in Table 5.1. The total output of the 25^o-tilted windfarm is 25.3 MW, which represents 14,5% more than the non-tilted wind farm. This constitutes a very significant increase of the total power. Similarly, the intermediate case presents an interesting increase of 6.5%. However, an important dissimilarity is observed between the two rows. Not only does the baseline case present variations, but the relative gain obtained with tilt is also modified importantly depending on the row. This is related to a lower upstream velocity, than affects both the power and the positive effect of the tilt.

	Wind farm		Row 1		Row 2	
Tilt-angle	Power [MW]	Variation	Power [MW]	Variation	Power [MW]	Variation
0^o	22.1	-	11.4	-	10.7	-
15^o	23.5	+6.5%	12.4	+8.8%	11.1	+4.1%
25^o	25.3	+14.5%	13.6	+19.7%	11.7	+9.0%

Table 5.1: *Mean power output of the farm*

5.3 Loads

In the previous Chapter, the variation of the forces across the rotor was shown to be increased when the rotor was inclined onward. This led to an increase of the tilting moment and of the fatigue loads. In this section, we aim at verifying to what extent this phenomenon is increased in a wind farm. The loads are thus sampled on the two last convective times, and an analysis of the tilting and bending moments is conducted.

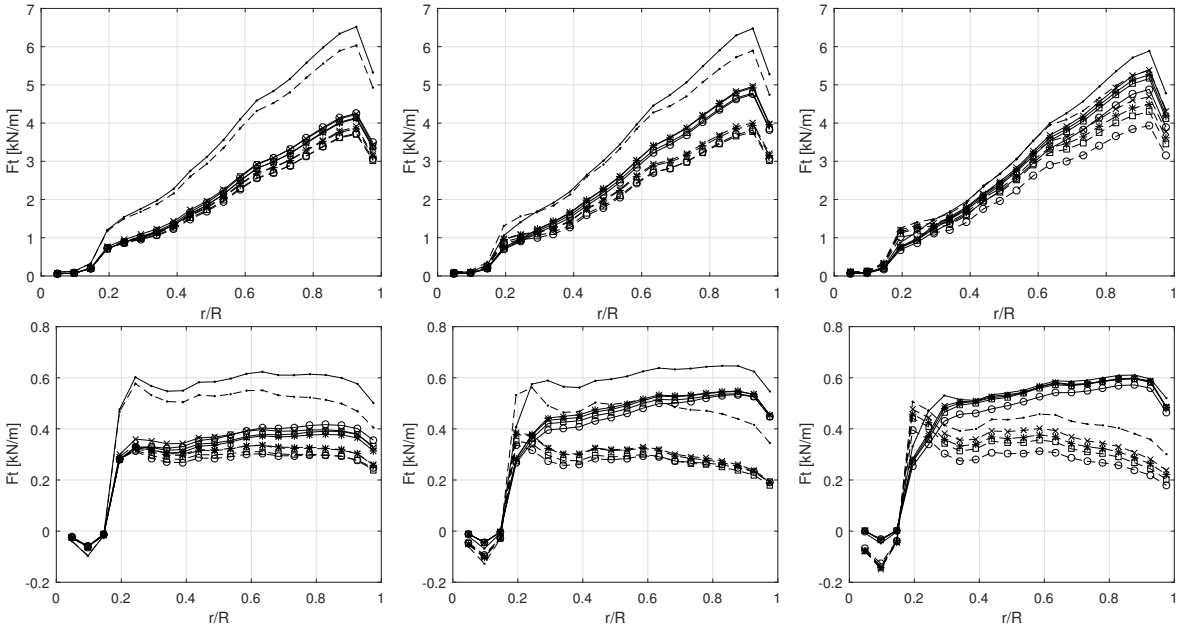

(a) 0 ° *(b) 15 °* *(c) 25 °*

Figure 5.3: *Differential of forces between the upper (solid) and lower (dashed) part of the rotor for the first row. Markers represents the position of the turbine in the row. From first to last: dots, circle, square, start and cross.*

5.3.1 Time-averaged loads

Figure 5.3 shows the evolution of the asymmetry of the time-averaged forces acting on the lower and the upper half of the rotor for the first row. The first turbine of the tilted cases present a larger asymmetry than the baseline case. When we switch from the first to the second turbine, the forces are reduced with a lower diminution for the tilted cases. The imbalance between the two regions of the rotor also evolves. It is conserved for the baseline case but grows for the tilted turbines. Then, from one turbine to another, the loads are lightly increased on both parts of the rotor. Only the lower part of the strongly tilted rotors undergoes a more noticeable increase. This suggests that the impacting flow contains larger velocities in it lower part. As this increase is not as pronounced for the upper part, the imbalance is decreased through the farm for that case. This can cause a reduction of the tilting moment for the last turbines.

5.3.2 Tilting moment

The loads asymmetry creates a tilting moment on the nacelle of the turbine, whose time-averaged evolution in the wind plant is depicted on figure 5.4a. The first tilted turbines suffer from a larger tilting moment due to the increased shear trough the rotor. Interestingly, this moment is very similar between the intermediate and the strong case. An increment of this tilting moment is observed from the first to the second turbine. This variation is mostly sensitive for the tilted cases and is linked to the lower velocities near the ground, and the faster recovery of the upper flow. Then, the tilting moment is decreased from turbine to

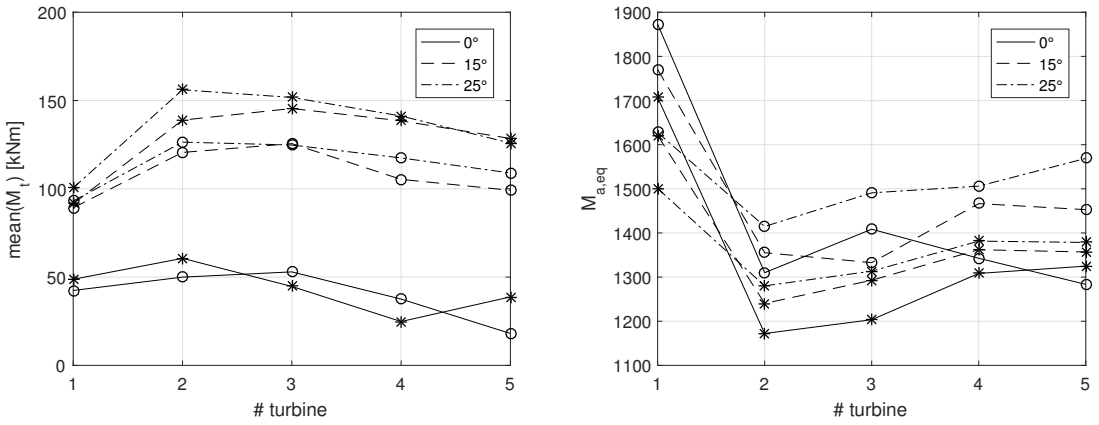

(a) Mean moment *(b) Equivalent alternating moment*

Figure 5.4: *Mean and alternating component of the tilting moment for the first (lines with stars) and second (lines with circles) row.*

turbine. For the baseline case, the reduction is mostly linked to the homogenization of the velocity profile behind the turbines. A similar effect is observed for the intermediate case. For the strong case, the reduction rate appears stronger and benefits from the increase of the forces on the lower part of the rotor.

The fatigue on the nacelle is assessed by computing the equivalent alternating load of the tilting moment as described in appendix B. The results are displayed on figure 5.4b. The first turbines benefit from the tilt angle, likely due to the general decrease of the loads due to the misalignment. However, this trend is inverted from the second turbine, were the tilted ones exhibit a higher equivalent alternating moment. The effect of the fatigue on the nacelle is globally increased as we go trough the wind farm, contrary to what was observed for the mean tilting moment.

5.3.3 Bending moments

The bending moments in the flapwise and edgewise directions also vary within the wind farm. Their mean value for each turbine is depicted on figure 5.5. The evolution through the farm is in agreement with the evolution of the power and thrust. Also, both moments evolve similarly. The bending moments are first dramatically decreased from the first to the second turbine due to the degradation of the free-flow. Then, their value increases from one turbine to the next one, with an increased rate for the tilted cases.

The alternating part of the bending moments is more likely to cause the failure of the blades. The previous chapter raised concerns about the rise of the alternating flapwise moment that was increased when the tilted configuration was used. Figure 5.6 shows the number of cycles per alternating moment range for the three considered cases. Interestingly, the behaviour of the flapwise moment is modified from the aforementioned observations. The alternating flapwise moment of the first wind turbines does not show major variations of is distribution between the tilted and no-tilted cases. On the contrary, the edgewise alternating moments present a modified number of cycles when the turbines are tilted, whereas this

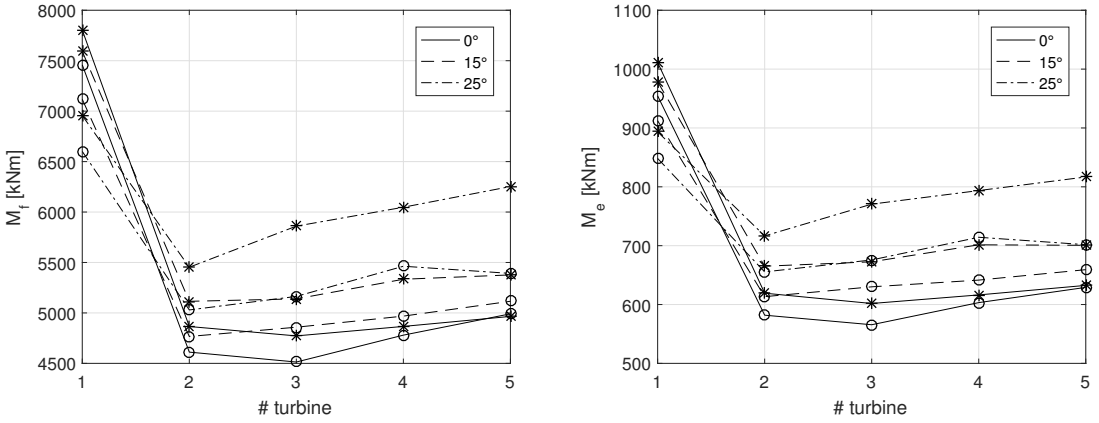

(a) Flapwise moment *(b) Edgewise moment*

Figure 5.5: *Mean bending moments for the first (lines with stars) and second (lines with circles) row.*

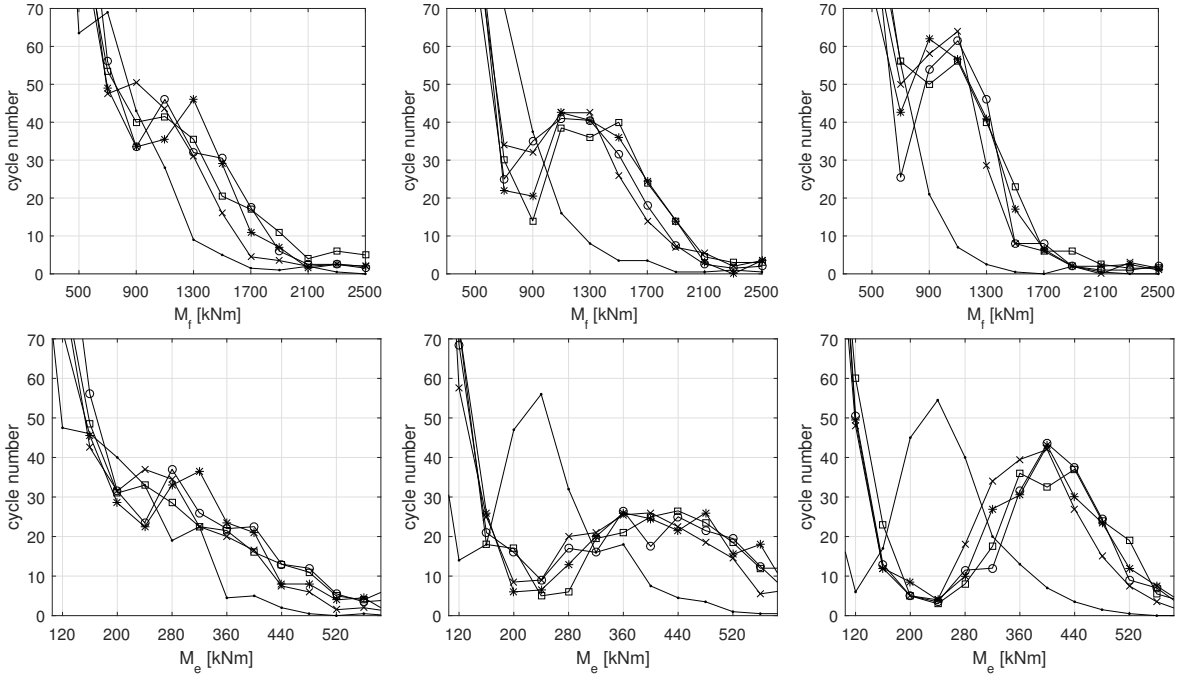

(a) 0 ° *(b) 15 °* *(c) 25 °*

Figure 5.6: *Number of cycles per alternating moment range. The curves are given for the five wind turbines of the first row. From first to last: dots, circle, square, start and cross.*

shift was less visible in the previous chapter. This variation of behaviour may be due to the controller that was added for the wind farm.

The moment acting on the downstream turbines is importantly modified when the rotors are tilted. For the baseline case, those turbines exhibit a slightly higher number of alternating

cycles than the first machine. This increase is likely due to the increased level of turbulence in the wake. However, the general tendency of the first curve is conserved. In the tilted cases, we observe a more important variation. For the flapwise moment, a new peak of cycles is observed at higher intensity. The edgewise moment also presents a shift of the peak that was observed for the first turbine. The rise of the number of cycles with a high alternating moment is due to the increase of the shear across the rotor that leads to higher forces on the upper part of the rotor, as observed earlier. Interestingly, the peaks are centered around higher intensities for the intermediate case than for the strong case. This is likely due to the reduction of the asymmetry of the forces observed for this strong case. In particular, it can be observed that the alternating moments of the last turbine are slightly lower than for the previous ones.

5.4 Wake statistics

This section will study the wake statistics to provide insight into the wake deflection. The instantaneous velocity and vorticity fields will not be discussed, but can be found in appendix C.

5.4.1 Time-averaged streamwise velocity

The mean velocity in vertical planes intersecting the hub of all the turbines on a row is displayed on figure 5.7. For the baseline case, the velocity deficit behind the first rotors is not deviated and impacts directly the downstream turbine. The wake of this second wind turbine consists in a more uniform velocity deficit with a slower hub jet. Furthermore, the wake grows slightly along the row, and the low velocity region increases in altitude as we move forward in the wake.

On the contrary, the low velocity region is deflected downwards when the turbines are tilted. The downstream located machines are impacted by a more shared flow, with lower velocities at the ground and higher ones at the top of the rotor. For the intermediate case, apart from the deflection, the deficit behind the first wind turbine is not very distinctive from the baseline. A major change is observed from the second wind turbine, where a clear asymmetry of the deficit is visible. The wake steering is also more perceptible from this second turbine. For the strong case, a clear decrease of the velocity deficit is observed for all the turbines. The intensity of the wake deflection is also more obvious, and the flow impacting the downstream turbines has a higher vertical gradient. The deviation angle tends to increase with the streamwise distance in both tilted cases. The entrainment is also visible, as the high velocity region tends to be lowered at each wind turbine.

It must also be pointed that the rows exhibit some differences in their behaviour. This difference is especially noticeable for the strong case where the deviation angle of the velocity deficit differs importantly from one row to another. This difference is linked to the inflow whose velocity is statistically lower for the second row. This variation of the inflow is due to large turbulent structures that do not collapse when a periodic computational domain of small lateral size is used. It would disappear if the size was much increased (which is not the scope of this study). Interestingly, the distinction between the two rows is less sensitive for the intermediate and baseline cases. Larger tilt angles might thus be more subject to variation of the inflow.

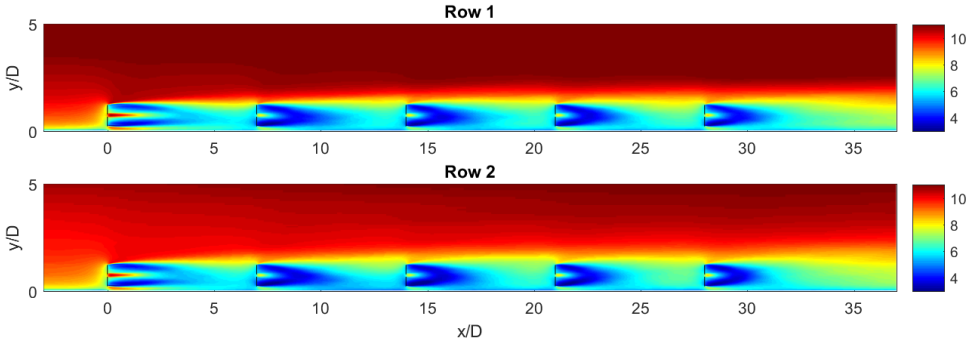

(a) No tilt angle

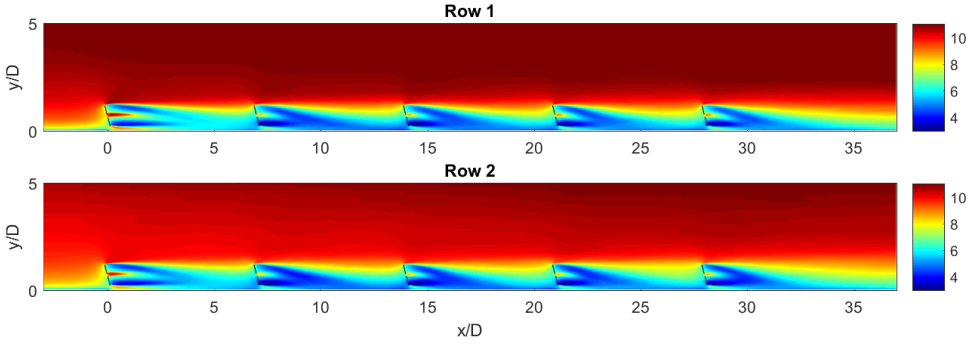

(b) 15° tilt angle

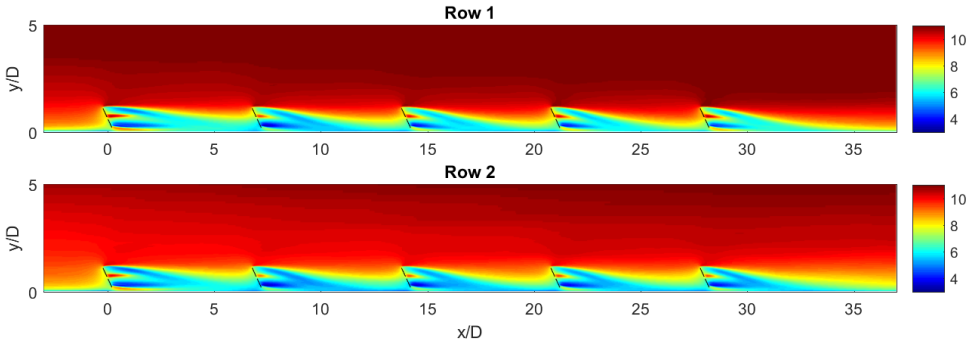

(c) 25° tilt angle

Figure 5.7: *Time averaged streamwise velocity in a vertical plane slicing the wind turbines.*

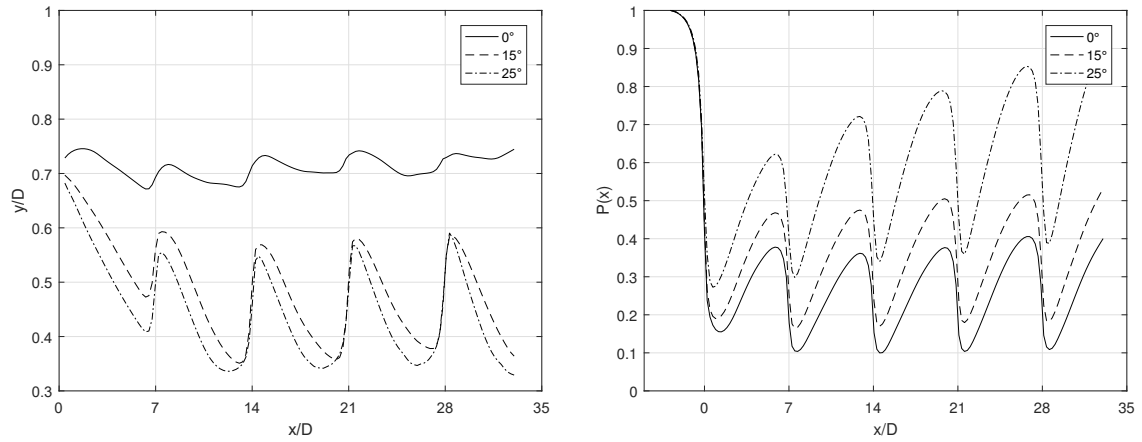

(a) Wake center height *(b) Power in the flow*

Figure 5.8: *Indicators of the wake recovery*

The wake deflection and recovery can be quantified using the approaches developed in section 4.4. In particular, the wake center height is measured by fitting a gaussian-like function to the velocity deficit. The latter is reduced to a square with a length of D with its center aligned with the hub, so that the fit is limited to the local wake behaviour. The power in the flow is also measured on a disk with the dimensions of the rotor, and swept along the x-axis.

Figure 5.8 presents the evolution of those two indicators for the first row. The two tilted cases are deviated downwards and a similar pattern is observed for each wind turbine. Lightly downstream, the wake starts being deflected almost linearly up to a minimum reached around 2 diameters before the next machine. There, a sudden increase is observed as the flow goes through a new rotor. After the second turbine, the altitude seems to achieve a steady state variation. Interestingly, the difference in the rate of descent observed between the strong and intermediate cases is not as large as it would have been expected from the difference of angle. This is attributed to the ground effects that prevents the deficit from being deflected importantly.

The power in the flow shows an alternation of increase and decrease similar to the wake center altitude, but its evolution in the array presents some major differences. First, it is observed that the variation is quite similar for the baseline and intermediate case. The patterns follow each other closely, with a moderate offset. Before the last turbine, the available power is 51% of the free-flow energy, against 41% in the baseline case. This represents a considerable increase, but it must be put in perspective with the 85% recovered in the strong case. This dissimilarity is somewhat surprising as it is not clearly marked in the wake deviation. Its origin is linked to two contributions. First, the dispersion of the wake is increased due to the larger redirection towards the ground, leading to strong interactions. Second, the entrainment of the high velocities is an important source of power increase. The efficiency of tilting is thus related not only to the deflection, but also to the ability to pull in the upper high energy of the flow.

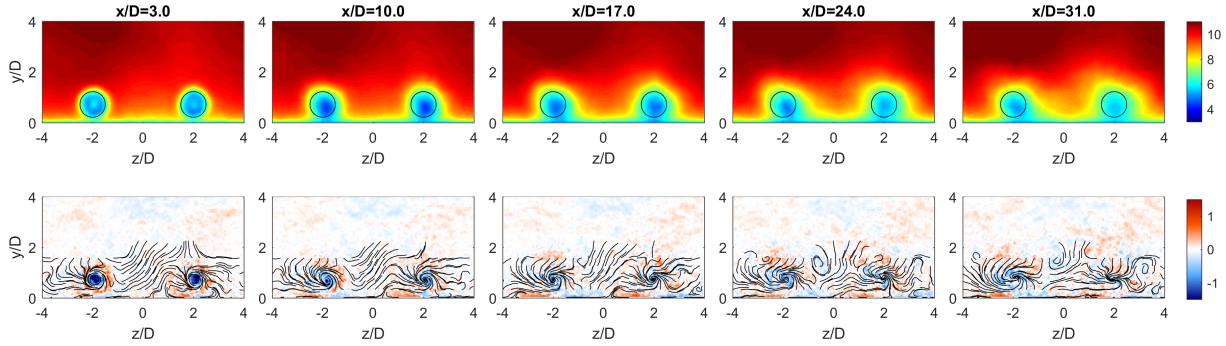

(a) No-tilt

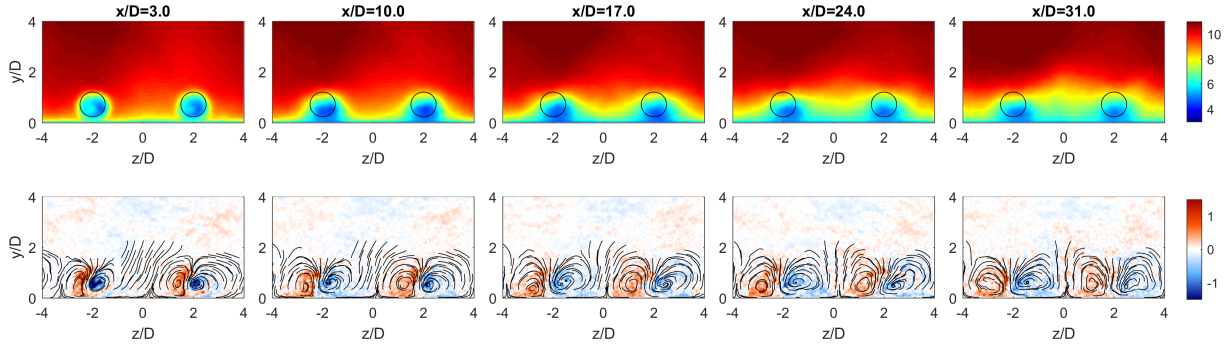

(b) Intermediate tilt

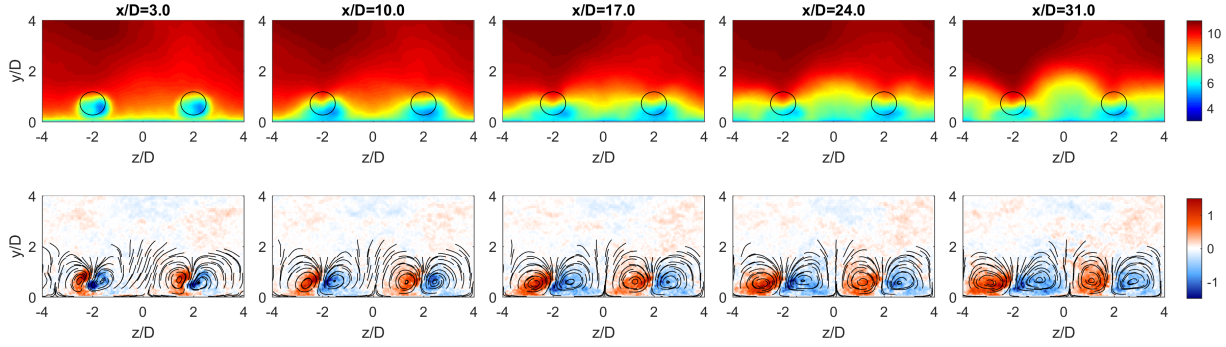

(c) Strong tilt

Figure 5.9: *Time-averaged streamwise velocity and vorticity with streamlines of transverse velocities.*

5.4.2 Time-averaged transverse velocities and vorticity

Figure 5.9 displays the time-averaged streamwise velocity and vorticity supplemented by the streamlines of the time-averaged transverse velocities, represented at several downstream locations. The sampled planes are parallel to the rotor plane and located three diameters behind each wind turbine. For the no-tilt case, the velocity deficit diffuses radially and the effect of the ground seems quite small. The deficit maintains a circular shape, and its center stays aligned with the center of the turbine. The influence on the lateral parts is thus limited. The transverse velocities have the spiral shape that was observed in section 4.4. At the first sampled location, the vortex core centered behind the wind turbine is clearly marked. However, as we propagate away from the turbine, it is more diffuse, and the spiral shape is more subtle. The transverse flow thus tends to become more complex through the row.

The effect is quite different in the case of tilted wind turbines. The wake generated by the two first machines is reshaped as an ellipse. As we go further downstream, this shape is spread over the ground. This generates a thick layer of low velocity deficit on the ground that affects the lateral parts of the farm. This effect is increased by the interaction between the turbines, and the wake has a lower altitude on each presented slice. Far downstream, the velocity deficit profile exhibited by the strongly tilted wind farm is opposite to the one observed for the non-tilted case. The central part of the farm experiences a high deficit whereas the rows are impacted by a higher velocity, due to the induced entrainment resulting from the wake deflection. The wake appears to be deflected similarly for the intermediate case, but to a smaller extent. The entrainment is not visible and the low velocity region presents a smoother thickness.

This behaviour is linked to the vortex system behind the tilted turbines. One observes two contra-rotating vortices. In the intermediate and strongly tilted cases, the vortices and the streamlines are similar behind the first turbine. However, as we descent in the flow, the intensity of the rotation is increased with a larger rate for the strong case. This justifies why the entrainment is more substantial. The last slices presents four distinct regions of rotation with opposed directions. Furthermore, the rotation of the strong case seems confined within the domain, with the streamlines presenting large angles near the boundary. This effect is likely to be mitigated in a real configuration, as the flow behind the lateral rows is not blocked sideways, and the separation between two rows is usually slightly wider.

The region of the flow on which the tilt has a positive impact must also be assessed. In fact, the deviation of the low velocity region to the center of the farm raises concerns about the maximal misalignment of the turbines for which the tilt angle stays beneficial. In fact, figure 5.9 clearly suggests that a turbine centered in the farm would have a higher power output in the baseline case than in the tilted cases. Using the mean streamwise velocity, we now aim at estimating the maximal offset between the turbine that would make tilting inefficient. The power in the flow at the location of a sixth wind turbine in the array is evaluated. This power is computed on a disk swept along the z-axis, 7D behind the last rotor. The resulting curves normalized with the power at the inflow are depicted on figure 5.10. In the tilted cases, the maximal power is observed right behind the two rows, whereas this location is the least favorable one for the the baseline case. The tilted rotors thus benefit from their aligned position, especially the strongly tilted ones. The latter case also presents a wider favorable region than the intermediate one. The allowable offset is almost 1D in that case, against 0.6D

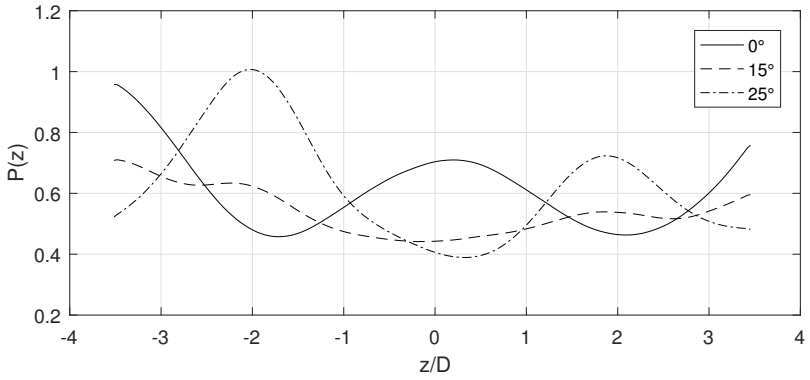

Figure 5.10: *Power available in the flow at the location of an hypothetical 6th wind turbine, as a function of its spanwise offset*

for the intermediate one. This is linked to a smoother power through the transverse direction, and the center of the wind farm is moderately affected, whereas the benefit behind the row is smaller.

5.5 Conclusion

The present Chapter was designed to determine the interactions between the wind turbines and how their behaviour was modified with the tilt angle. Those interactions were assessed regarding three important parameters: the power and thrust, the variation of the loads on the turbines and the wake behaviour. The retrieved values for the total power output were very exciting as an important increase of 14.5% or 6.5% was observed in the strongly or intermediate cases. The losses occurring on one single turbine are thus clearly compensated by the increase of the production of the downstream machines. The investigation of the wake showed that this increase is not only due to the wake deflection, but also to the interaction with the ground and to the entrainment of higher velocities. Those two phenomenons were shown to be increased through the wind plant.

However, those results are counterbalanced by two side-effects. First, the downwards deviation behind the rotor is balanced by an upward velocity between the rows. This raises some low velocities from the bottom of the shear layer and reduces the power in the flow alongside the rows. This reduces the benefits of tilting wind turbines when the rows are not well aligned with the mean wind direction. In our case, it was determined that a sixth wind turbine placed 7D behind the last rotor would not benefit from an offset larger than 1D in the strong case. This maximal offset was even reduced to 0.6D in the intermediate case. Second, the alternating loads acting on the downstream located turbines where shown to be increased. This is due to the higher imbalance between the upper and the lower part of the rotor. However, an interesting observation is that this imbalance is reduced in the strongly tilted case, due to the larger forces on the lower part of the rotor. The mean moment was thus increased, but the alternating part was reduced.

Chapter 6

Conclusion and perspectives

This thesis was undertaken to provide a deeper knowledge of an original wake steering strategy. It based on the variation of the tilt angle of the wind turbines, that is able to deflect the wake downwards or upwards. For this purpose, the actuator lines model was improved and verified in various configurations. Then, it was used to simulate tilted wind turbines in single or wind farm configurations to characterize the effect of this adaptation.

The first part of this dissertation focused on the improvement of the actuator lines model. A new way of distributing the forces computed around the lines was implemented. This new approach distributes the forces around the blades using a non-isotropic 2D mollification kernel to increase the accuracy of the overall method. This method was characterized and verified against the advanced actuator disk method and showed positive results. Its ability to predict the main aspects of the flow and the effect on the rotor was observed at both coarse and fine resolution.

This new model stands as an interesting complement to the actuator disk method. Whereas the latter performs very well in large wind farm simulations, the presented actuator lines model can be used at higher resolution to provide more insight into the blade dynamics or the near wake behaviour. In fact, the actuator lines method was shown to be more sensitive to the grid coarsening; yet, it is able to retrieve complex vortex structures and to account for the finite number of blades. In future works, the actuator lines model could be enriched by a structural dynamics solver so that the fluid-structure interaction problem could be handled. The presented approach could also be transposed to the vertical axis wind turbines to enable the simulation of their complex aerodynamics at a decent computational cost.

The second part of this thesis assessed how tilting the wind turbines affects the wake and the behaviour of the rotor. Very interesting results were found regarding the efficiency of the total wind farm, as the power production was drastically increased when a large tilt was applied. However, this improvement induced a moderate increase of the fatigue loads, and the velocity deficit deformation decreased the energy of the flow sideways. Further investigations could be conducted with different operating conditions varying the wind speed and direction, to verify that those encouraging conclusions still hold. The presented analogy between a tilted rotor and a horizontal lifting line could also be used to develop a very simplified model of the wake deviation, that could be used to predict an optimal tilt angle for the wind farm.

Tilting would be particularly interesting if it could be used dynamically, as it showed a real potential when the turbines are aligned with the mean wind direction and with a large tilt angle. In this case, the overall output of the farm could be drastically increased. However, the conception of a mechanism that would allow such a movement might be complicated. Before this feature becomes available, a constant tilt angle applied to all the rotors is very likely to increase the efficiency of the wind plant in the well aligned cases. However, further investigations should then verify that the minor power decrease in the non-aligned cases is counterbalanced by the increase of the "essentially aligned" case.

Appendix A

Statistics of the atmospheric boundary layers

This additional note concerns the behaviour of the ABLs that have been created for the simulations of the wind turbines in turbulent flows. Three cases were considered. Two small ABLs were generated in a small domain of size 10Dx8Dx4D[1] with a lower and a higher resolution. A third one was computed using a larger domain of size 40Dx8Dx8D with a relatively coarse resolution of 32 points per diameter at hub height.

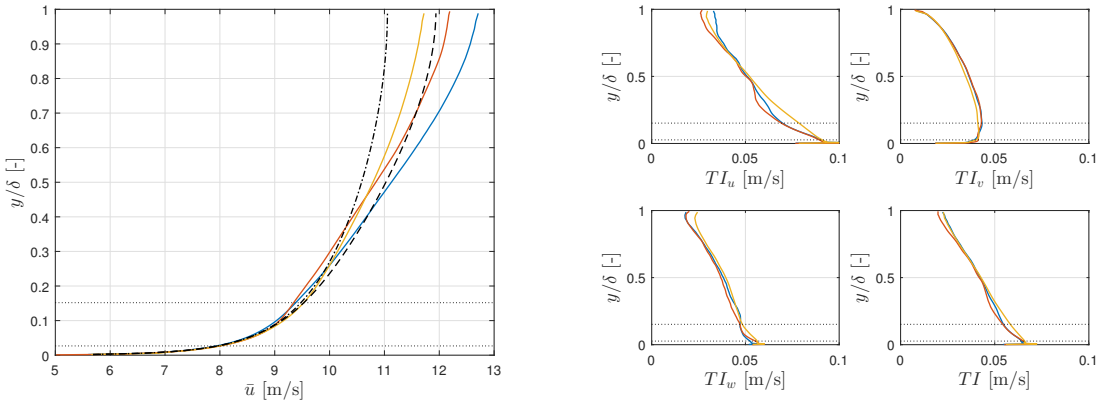

(a) Mean velocity profile *(b) Turbulence intensity*

Figure A.1: *Statistics of the ABLs. Theoretical expectations (black) for a boundary layer (dashed) and a channel (dash-dotted) and the profiles recovered in the small ABLs of Chapter 3 & 4 (coarse in blue, fine in red) and the larger ABL of Chapter 5 (yellow). The dotted lines enclose the rotor altitude (90± 63m).*

The statistics of the recovered boundary layers are shown for all cases on figure A.1. The theoretical value is obtained using the Coles composite profile that reads

$$\frac{\bar{u}}{\bar{u}_\tau} = \frac{1}{\kappa}\log\left(\frac{y}{y_0}\right) + G(\eta)$$

[1]D is the diameter of the considered turbine, here the NREL-5MW of dimension $D = 126m$

where $\eta = y/\delta$, $\kappa = 0.38$, y_0 is set to 2.8mm and u_τ to 0.33m/s in order to recover the speed of 9m/s and the turbulence intensity of 6% at the hub. the Coles complementary function $G(\eta)$ is defined as

$$G(\eta) = D(3(\alpha\eta)^2 - 2(\alpha\eta)^3)$$

where D=2.70 for a turbulent boundary layer, and α is set so that the slope of the profile is zero when $\eta = 1$. It could be argued that the no-through condition imposed at the upper boundary differs from the boundary layers theory, and that a half channel case should be considered. In that case, D=0.3 and the complementary function has a much smaller amplitude.

The numerically obtained velocity profiles differ in some ways from the theoretical expectations, especially for the small domain cases considered in Chapters 3 and 4. This is partially linked to the small size of the computational domain and the resolution, as the statistics are closer to the reference for a larger domain or a higher resolution. The largest discrepancies are observed at high altitude, where the grid is coarser due to the important stretching in the vertical direction. Interestingly, the large domain case presents a profile that is in between the boundary layer and the half channel expectations. An even larger domain, with a finer resolution, would produce a profile that resembles even more to the half channel case.

An insight into the statistics recovered at the rotor's height is also provided on figure A.2. In this region, the agreement is better with the theoretical expectations. The best concordance is found for the large domain. The latter also has a slightly larger turbulence intensity, except for the vertical one. At the hub, the mean velocity is very close from the targeted 9m/s. The turbulence intensity globally decreases with the altitude and its value at the hub height is close to 5.8% for the small cases. For the larger domain, it reaches 6.3 %.

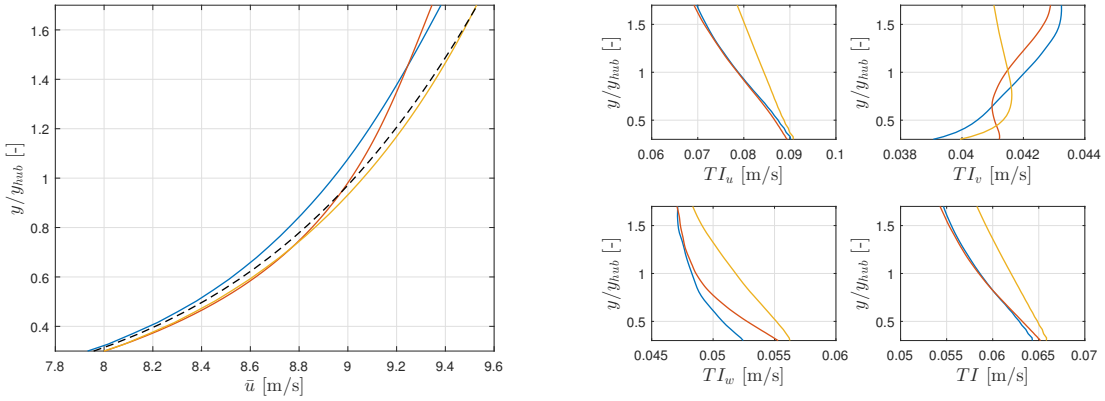

(a) Mean velocity profile *(b) Turbulence intensity*

Figure A.2: *Statistics of the ABLs. Theoretical expectations (black) and the profiles recovered in the small ABLs of Chapter 3 & 4 (coarse in blue, fine in red) and the larger ABL of Chapter 5 (yellow)*

Appendix B

Computation of the equivalent bending moment

The variations of the bending moment acting on the blades is a dominant cause of breakage due to fatigue. This variations come from the unstationary nature of the turbulent free-flow but also from the sheared mean velocity profile obtained in an ABL. The spectrum of this variation is very large, and summarizing all those effects into one measurement is preferable. An approach for the analysis of the varying loads is detailed here. It is based on the estimation of the equivalent bending moment M_{eq}.

First, the time-dependant moment $M(t)$ must be converted into a number of cycles. This is done using the rainflow algorithm. This leads to the knowledge of the number of cycles n_i having an alternative load $M_{a,i}$ and a mean moment $M_{m,i}$. However, the turbulent inflow tends to pollute the signal with small oscillations, that will be considered at cycles by the rainflow counting. This issue is solved either by smoothing the very low frequencies of the initial signal, or by neglecting the cycles associated with a moment lower than 10% of the variation due to the blade rotation. This second approach was applied here, even if it did not modified the obtained results substantially.

From there, the cumulative damage on the blade for the sampled time is given by the Palmgren-Miner's rule as

$$D = \sum_{i=0}^{n_c} \frac{n_i}{N_{F,i}}.$$

where n_b is the number of cycle bins and $N_{F,i}$ is the number of cycles to failure. The latter is linked to the alternating moment by the M-N curve

$$N_F = kM_a^{-m}$$

with k and m two parameters depending on the blade material. The M-N curve is derived from the more common S-N curve, assuming that the bending moment are proportional to the stresses. However, this equation is only valid for a pure alternating moment with no mean component. This value can be obtained from the Goodman diagram, the Walker rule or the Haigh slope. However, as pointed out in [32], the mean moment is often very small compared to the tensile one, and the correction only has a little impact when applied to the aerodynamic moments of the blades. In fact, the Goodman's approach to retrieve the purely alternating moment M_{pa} was implemented by adding the effect of the mean moment with

$$M_{pa} = \frac{M_a M_u}{M_u - M_m}$$

where M_u is the ultimate moment based on the value of the ultimate stress of the material and transformed into a stress based on the geometry of the blade. The ultimate moment was by far larger than the mean moment and the correction factor was very close to one. This led to a negligible variation of the results.

The equivalent moment M_{eq} is a purely alternating moment that generates the same damage than the measured unsteady moment. Is is thus linked to the damage by the relation

$$\sum_{i=0}^{n_c} \frac{n_i}{k M_i^{-m}} = D = \frac{N_{eq}}{k M_{a,eq}^{-m}},$$

which can be rewritten as (also found in [37]),

$$M_{a,eq} = \left(\sum_{i=0}^{n_c} \frac{n_i M_i^{-m}}{N_{eq}} \right)^{1/m}.$$

The value of the M-N curve slope slope m is set to 10 for the glass-fiber composing the rotor blades [38, 32]. The number of equivalent cycles N_{eq} is chosen so that the frequency of the equivalent alternating moment is 1 [Hz].

Appendix C

Instantaneous velocity in the wind farms

This appendix shows the instantaneous velocities in the wind farms, as a complement to the statistics presented in Chapter 5.

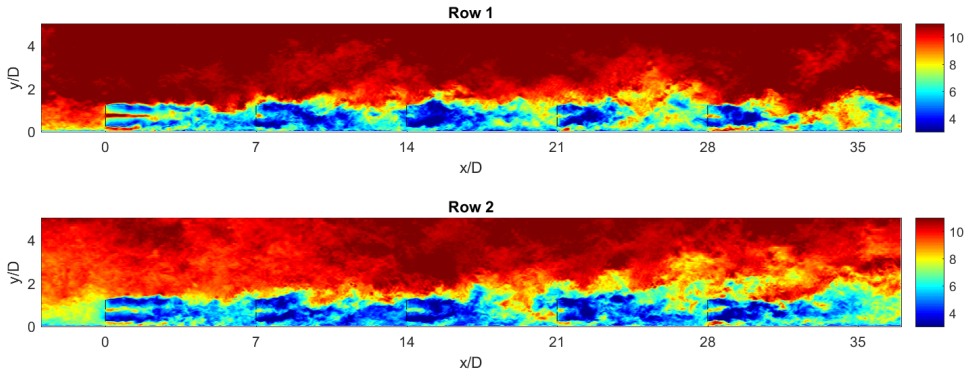

Figure C.1: *Instantaneous streamwise velocity in z-planes. The turbines are not tilted*

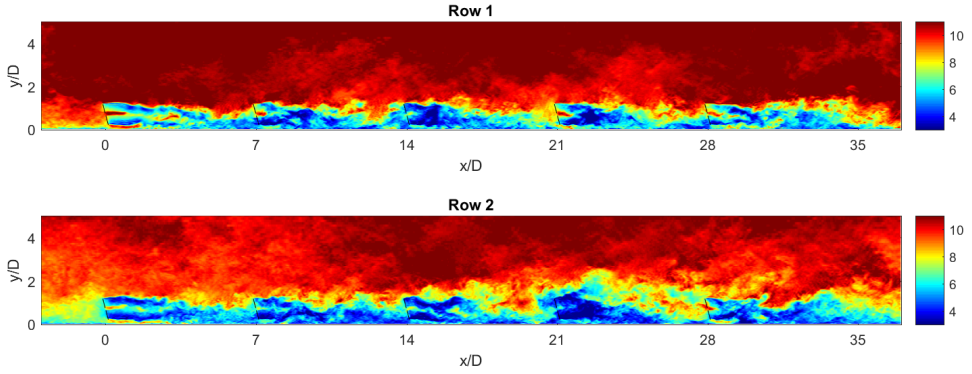

Figure C.2: *Instantaneous streamwise velocity in z-planes. The turbines are tilted with an angle of 15^o*

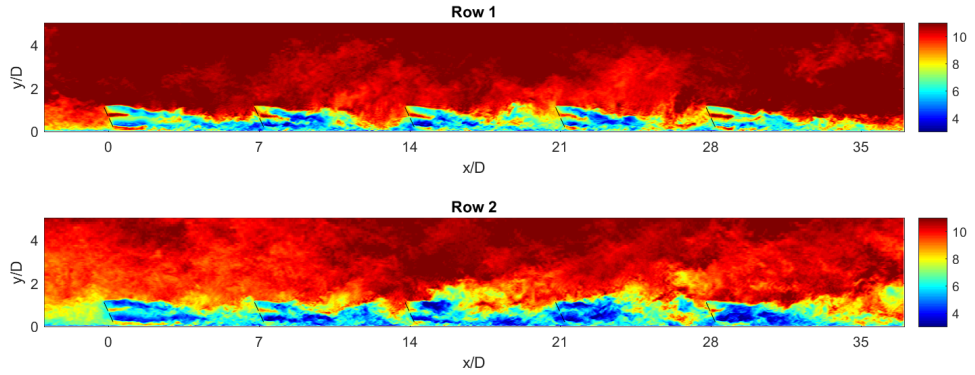

Figure C.3: *Instantaneous streamwise velocity in z-planes. The turbines are tilted with an angle of 25°*

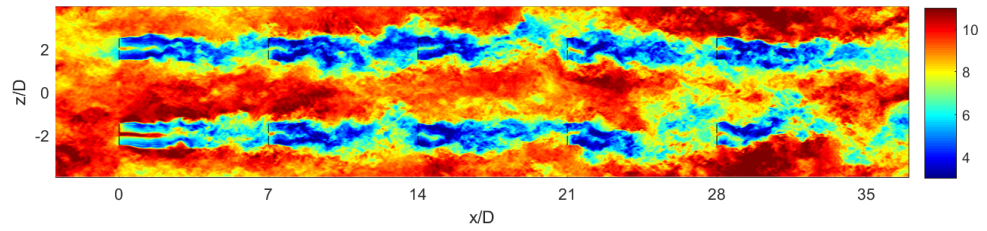

Figure C.4: *Instantaneous streamwise velocity in the y-plane. The turbines are not tilted*

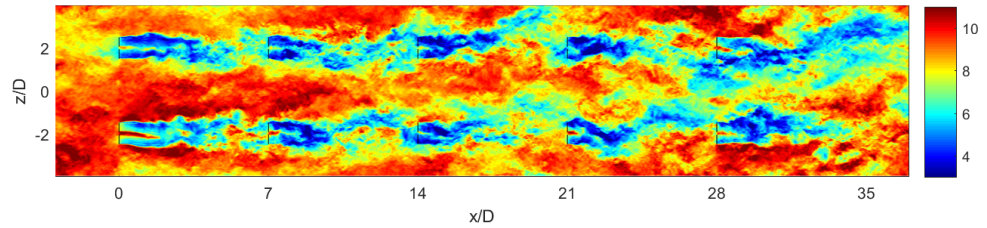

Figure C.5: *Instantaneous streamwise velocity in the y-plane. The turbines are tilted with an angle of 15°*

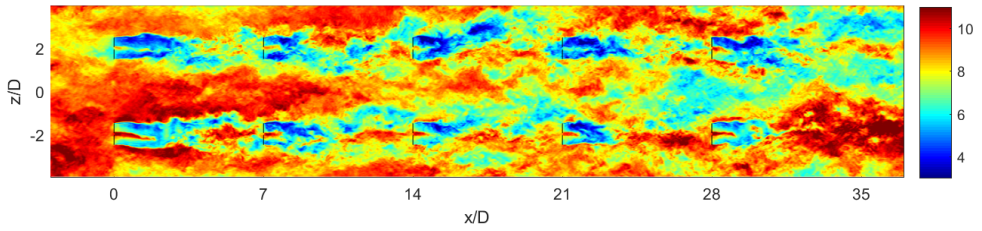

Figure C.6: *Instantaneous streamwise velocity in the y-plane. The turbines are tilted with an angle of 25º*

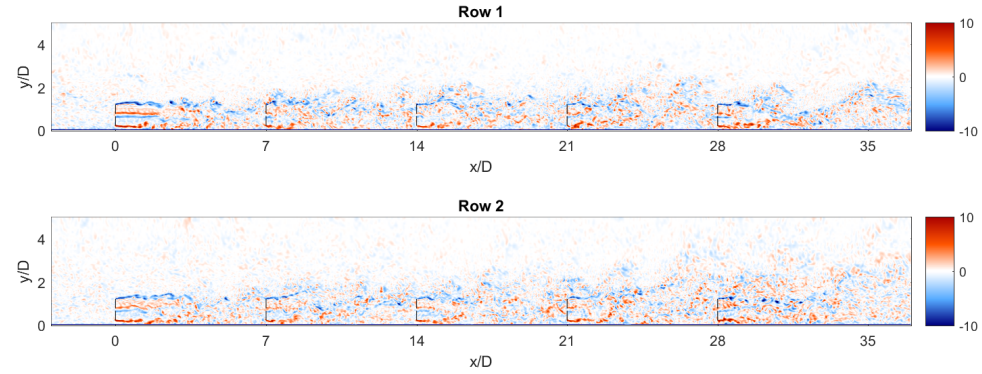

Figure C.7: *Instantaneous (normalized) vorticity in the perpendicular direction to the z-planes. The turbines are not tilted*

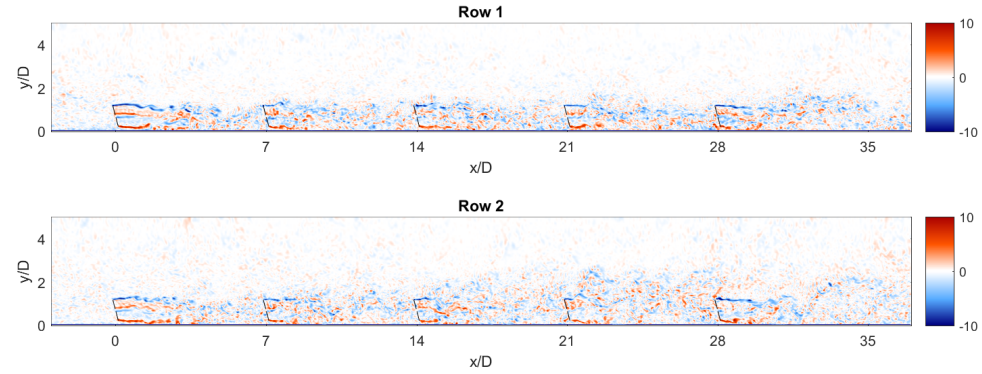

Figure C.8: *Instantaneous (normalized) vorticity in the perpendicular direction to the z-planes. The turbines are tilted with an angle of 15º*

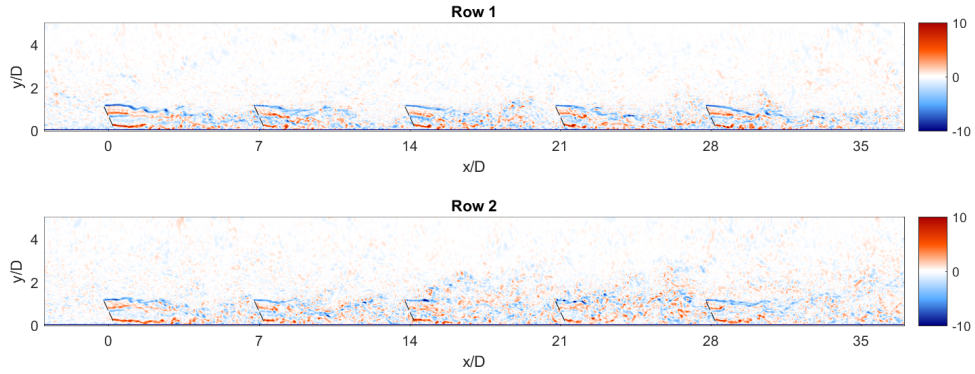

Figure C.9: *Instantaneous (normalized) vorticity in the perpendicular direction to the z-planes. The turbines are tilted with an angle of 25º*

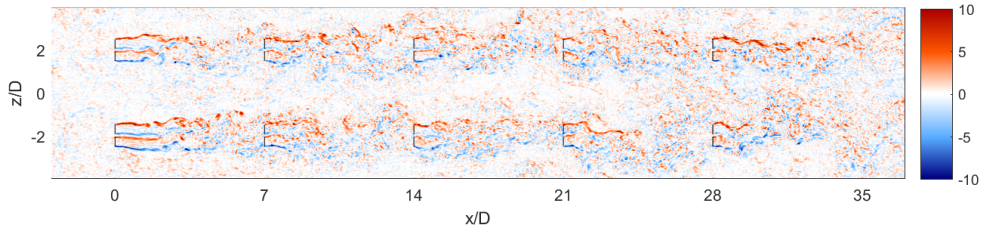

Figure C.10: *Instantaneous (normalized) vorticity in the perpendicular direction to the y-plane. The turbines are not tilted*

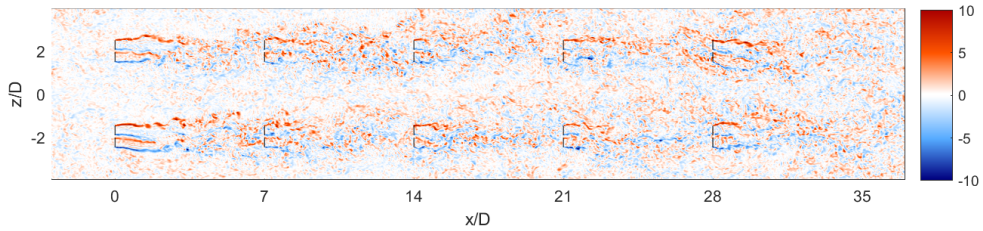

Figure C.11: *Instantaneous (normalized) vorticity in the perpendicular direction to the y-plane. The turbines are tilted with an angle of 15º*

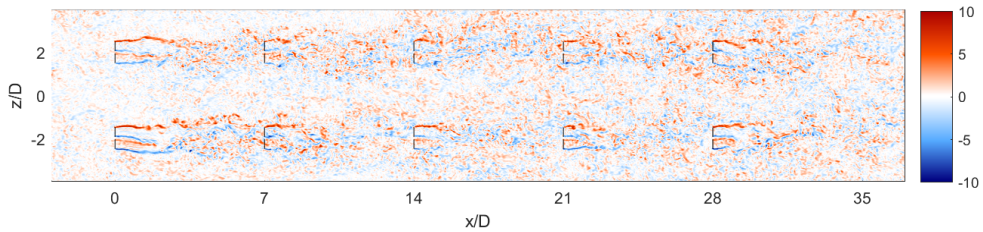

Figure C.12: *Instantaneous (normalized) vorticity in the perpendicular direction to the y-plane. The turbines are tilted with an angle of 25º*

Bibliography

[1] V. Smil, *Energy Transitions: Global and National Perspectives*. ABC-Clio, 2017.

[2] O. Edenhofer, R. P. Madruga, and Y. Sokona, "Renewable energy sources and climate change mitigation," 2012.

[3] WindEurope asbl, "Wind energy is competitive," 2016.

[4] Energy observatorium Federal public service of economy, "Iea wind annual report of 2015," 2016.

[5] R. Stevens, D. F. Gayme, and C. Meneveau, "Effect of turbine alignment on the average power output of wind-farms," 2013.

[6] P. Gebraad, J. J. Thomas, A. Ning, P. Fleming, and K. Dykes, "Maximization of the annual energy production of wind power plants by optimization of layout and yaw-based wake control," *Wind Energy*, vol. 20, no. 1, pp. 97–107, 2017.

[7] A. M. Abdelsalam and V. Ramalingam, "Effect of the tilt angle on the wind turbine performance and wakes," *Conference paper*, 2013.

[8] P. A. Fleming, P. M. Gebraad, S. Lee, J.-W. van Wingerden, K. Johnson, M. Churchfield, J. Michalakes, P. Spalart, and P. Moriarty, "Evaluating techniques for redirecting turbine wakes using sowfa," *Renewable Energy*, vol. 70, pp. 211–218, 2014.

[9] J. Annoni, A. Scholbrock, M. Churchfield, and P. Fleming, "Evaluating tilt for wind plants," pp. 717–722, 2017.

[10] M. Moens, M. Duponcheel, G. Winckelmans, and P. Chatelain, "An actuator disk method with tip-loss correction based on local effective upstream velocities," *Wind Energy*, vol. 21, no. 9, pp. 766–782, 2018.

[11] M. Duponcheel, "Direct and large-eddy simulation of turbulent wall-bounded flows : further development of a parallel solver, improvement of multiscale subgrid models and investigation of vortex pairs in ground effect," 2009.

[12] J. Smagorinsky, "General circulation experiments with the primitive equations. i. the basic experiment," *Mon. Weather Rev. 91*, pp. 99–164, 11 1963.

[13] O. Thiry, "Investigation of wall shear stress models for large eddy simulation," 2017. PhD thesis at Université Catholique de Louvain.

[14] M. Lee, B. Oh, and Y. Kim, "Canonical fractional-step methods and consistent boundary conditions for the incompressible navier-stokes equations," *Journal of computational physics*, 2001.

[15] L. Georges, "Development and validation of a les methodology for complex wall-bounded flows : application to high-order structured and industrial unstructured solvers," 2007.

[16] H. Glauert, *Airplane Propellers*, pp. 169–360. Berlin, Heidelberg: Springer Berlin Heidelberg, 1935.

[17] J. N. Sorensen, W. Z. Shen, and R. Mikkelsen, "Tip loss correction for actuator/navier–stokes computations," *Journal of Solar Energy Engineering-transactions of The Asme - J SOL ENERGY ENG*, vol. 127, 05 2005.

[18] S. Guntur, N. Troldborg, and M. Gaunaa, "Application of engineering models to predict wake deflection due to a tilted wind turbine.," *EWEA 2012-European Wind Energy Conference & Exhibition. European Wind Energy Association (EWEA)*, 2012.

[19] J. Sorensen and W. Shen, "Numerical modeling of wind turbine wakes," *ASME. J. Fluids Eng.*, 2002.

[20] N. Troldborg, "Actuator line modelling of wind turbine wakes," 2008. PhD thesis at Technical University of Denmark.

[21] W. Z. Shen, R. Mikkelsen, J. N. Sørensen, and C. Bak, "Tip loss corrections for wind turbine computations," *Wind Energy*, vol. 8, no. 4, pp. 457–475, 2005.

[22] P. Jha, M. Churchfield, P. Moriarty, and S. Schmitz, "Guidelines for volume force distributions within actuator line modeling of wind turbines on large-eddy simulation-type grids," *ASME. J. Sol. Energy Eng.*, 2014.

[23] L. Martínez Tossas and C. Meneveau, "Optimal smoothing length scale for actuator line models of lifting surfaces," 11 2015.

[24] M. J. Churchfield, S. J. Schreck, L. A. Martinez, C. Meneveau, and P. R. Spalart, "An advanced actuator line method for wind energy applications and beyond," p. 1998, 2017.

[25] R. F. Mikkelsen and J. N. Sorensen, "Actuator disk methods applied to wind turbines," 2004.

[26] M. Shives and C. Crawford, "Mesh and load distribution requirements for actuator line cfd simulations," *Wind Energy, 16(8)*, pp. 1183–1196, 2013.

[27] P. K. Jha and S. Schmitz, "Actuator curve embedding–an advanced actuator line model," *Journal of Fluid Mechanics*, 2018.

[28] G.-H. Cottet, P. D. Koumoutsakos, P. D. Koumoutsakos, *et al.*, *Vortex methods: theory and practice*. Cambridge university press, 2000.

[29] J. J. Monaghan, "Extrapolating b splines for interpolation," *Journal of Computational Physics*, vol. 60.2, pp. 253–262, 1985.

[30] M. Moens, "Large eddy simulation of wind farm flows: improved actuator disk model and investigation of wake phenomena," 2018. PhD thesis at Université Catholique de Louvain.

[31] J. Jonkman, S. Butterfield, and W. Musial, "Definition of a 5-mw reference wind turbine for offshore system development," *National Renewable Energy Lab.(NREL)*, 2009.

[32] M. Hansen, *Aerodynamics of Wind Turbines*. Earthscan, 2nd ed., 2008.

[33] E. Branlard, *Wind Turbine Aerodynamics and Vorticity-Based Methods: Fundamentals and Recent Applications*, vol. 7. Springer, 2017.

[34] T. L. Martinez, S. Leonardi, M. Churchfield, and P. Moriarty, "A comparison of actuator disk and actuator line wind turbine models and best practices for their use," 2012.

[35] I. Janajreh, R. Qudaih, I. Talab, and C. Ghenai, "Aerodynamic flow simulation of wind turbine: Downwind versus upwind configuration," *Energy Conversion and Management*, vol. 51, no. 8, pp. 1656 – 1663, 2010.

[36] M. Matsuishi and T. Endo, "Fatigue of metals subjected to varying stress," *Japan SMech. Engineerig.*, 1968.

[37] J. P. A. A. Blasques and A. Natarajan, "Mean load effects on the fatigue life of offshore wind turbine monopile foundations," 2013.

[38] D. T. Griffith and T. D. Ashwill, "The sandia 100-meter all-glass baseline wind turbine blade: Snl100-00," *Report from Sandia, Mexico*, 2011. Annex A.

[39] M. Boudreau and G. Dumas, "Comparison of the wake recovery of the axial-flow and cross-flow turbine concepts," *Journal of Wind Engineering and Industrial Aerodynamics*, vol. 165, pp. 137–152, 06 2017.

[40] J.-J. Trujillo, F. Bingöl, G. C. Larsen, J. Mann, and M. Kühn, "Light detection and ranging measurements of wake dynamics. part ii: two-dimensional scanning," *Wind Energy*, no. 1, pp. 61–75, 2011.

[41] M. Bastankhah and F. Porté-Agel, "A new analytical model for wind-turbine wakes," *Renewable Energy*, vol. 70, pp. 116 – 123, 2014.

[42] C. R. Shapiro, D. F. Gayme, and C. Meneveau, "Modelling yawed wind turbine wakes: a lifting line approach," *Journal of Fluid Mechanics*, vol. 841, 2018.

[43] L. A. Martínez-Tossas, J. Annoni, P. A. Fleming, and M. J. Churchfield, "The aerodynamics of the curled wake: a simplified model in view of flow control," *Wind Energy Science (Online)*, vol. 4, no. NREL/JA-5000-73451, 2019.

UNIVERSITÉ CATHOLIQUE DE LOUVAIN
École polytechnique de Louvain
Rue Archimède, 1 bte L6.11.01, 1348 Louvain-la-Neuve, Belgique | **www.uclouvain.be/epl**